THE CHARACTERIZATION OF SECONDARY LITHIUM-ION BATTERY DEGRADATION WHEN OPERATING COMPLEX, ULTRA-HIGH POWER PULSED LOADS

by

DEREK N. WONG

Presented to the Faculty of the Graduate School of

The University of Texas at Arlington in Partial Fulfillment

of the Requirements

for the Degree of

DOCTOR OF PHILOSOPHY

THE UNIVERSITY OF TEXAS AT ARLINGTON

September 2016

Acknowledgements

I would like to thank my advisor Dr. David Alan Wetz for guiding me through my doctorate studies. Also, none of the work presented in this paper would be possible without the support of the US Navy specifically from Dr. John M. Heinzel and Dr. Azzam N. Mansour. The resources they have provided have been key to the completion of my doctorate studies.

Furthermore, I would like to extend my gratitude to my parents Kendall and Marinda, my sister Melanie, my brother Ryan, and my wife Winnie for their moral support. Through the rough times fighting to get this degree, you have been there by my side to hear the good and the bad.

Lastly, I would like to thank my lab mates Isaac, Clint, Matt, Donald, Chris and Caroline who have provided me with critical advice and shared with me all the knowledge you have regardless of how difficult or time consuming it was. I would also like to thank Dr. Anthony Matasso who trained and mentored me all throughout my graduate career. Without the support of all of you I would not have the knowledge to start let alone complete my experiments. Thank you again.

September 8, 2016

Abstract

THE CHARACTERIZATION OF SECONDARY LITHIUM-ION BATTERY DEGRADATION UNDER COMPLEX, ULTRA-HIGH POWER PULSED LOADS

Derek N. Wong, PhD

The University of Texas at Arlington, 2016

Supervising Professor: David A. Wetz, PhD

The US Navy is actively developing all electric fleets, raising serious questions about what is required of onboard power supplies in order to properly power the ship's electrical systems. This is especially relevant when choosing a viable power source to drive high power propulsion and electric weapon systems in addition to the conventional loads deployed aboard these types of vessels. Especially when high pulsed power loads are supplied, the issue of maintaining power quality becomes important and increasingly complex. Conventionally, a vessel's electrical power is generated using gas turbine or diesel driven motor-generator sets that are very inefficient when they are used outside of their most efficient load condition. What this means is that if the generator is not being utilized continuously at its most efficient load capacity, the quality of the output power may also be effected and fall outside of the acceptable power quality limits imposed through military standards. As a solution to this potential problem, the Navy has proposed using electrochemical storage devices since they are able to buffer conventional generators when the load is operating below the generator's most

efficient power level or able to efficiently augment a generator when the load is operating in excess of the generator's most efficient power rating. Specifically, the US Navy is interested in using commercial off-the-shelf (COTS) lithium-ion batteries within an intelligently controlled energy storage module that could act as either a prime power supply for on-board pulsed power systems or as a backup generator to other shipboard power systems.

Due to the unique load profile of high-rate pulsed power systems, the implementation of lithium-ion batteries within these complex systems requires them to be operated at very high rates and the effects these things have on cell degradation has been an area of focus. There is very little published research into the effects that high power transient or pulsed loading has on the degradation mechanisms of secondary lithium-ion cells. Prior to performing this work, it was unclear if the implementation of lithium-ion batteries in highly transient load conditions at high rate would accelerate cell degradation mechanisms that have been previously considered as minor issues. This work has focused on answering these previously unanswered questions.

In early experiments performed here, COTS lithium-iron-phosphate (LFP) cells were studied under high-rate, transient load conditions and it was found that their capacity fade deviated from the traditional linear behavior and exponentially declined until no charge could be accepted when recharge was attempted at high rate. These findings indicated that subjecting LFP chemistries to transient, high rate charge/discharge profiles induced rapid changes in the electrode/electrolyte interface that rendered the cells useless when high rate recharge was required. These findings suggested there was more phenomena to learn about how these cells degraded under

high rate pulsed conditions before they are fielded in Naval applications. Therefore, the research presented here has been focused on understanding the degradation mechanisms that are unique to LFP cells when they are cycled under pulsed load profiles at high charge and discharge rates. In particular, the work has been focused on identifying major degradation reactions that occur by studying the surface chemistry of cycled electrode materials. Efforts have been performed to map the impedance evolution of both cathode and anode half cells, respectively, using a novel three electrode technique that was developed for this research. Using this technique, the progression of degradation has been mapped using analysis of differential capacitance spectrums. In both the three electrode EIS mapping and differential capacitance analysis that has been performed, electrical component models have been developed. The results presented will show that there are unique degradation mechanisms induced through high rate pulsed loading conditions that are not normally seen in low rate continuous cycling of LFP cells.

Table of Contents

List of Figures

List of Tables

Chapter 1: Background and Hypothesis

To date, the US Navy has relied on fossil fuel based propulsion and fuel generated electricity in order to drive their ships and supply power to onboard electrical loads. Weapon systems deployed on navy ships have historically been operated by traditional chemical and explosive based propulsion and ordinance. Recently, the Navy has constructed a new class of destroyers which are propelled by electrically driven motors [1]. In these ships, there is a plan to integrate new weapon systems such as electromagnetic launchers and solid state laser, among others, that will be electrically driven. Many of these new directed energy systems will operate using pulsed power supplies in a transient, repetitive mode of operation. This means that they will demand power from their prime power system in very unique ways varying from very high power to near zero power in an on and off manner. This creates challenges for shipboard power engineers who are trying to designing a power source to supply for these complex systems [2, 3, 4]

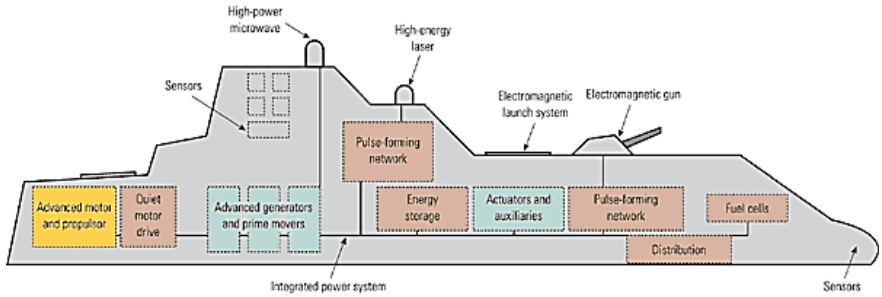

Figure 1: Systems on future all electric driven Navy warships [5]

Pulsed power loads are characterized by their high peak to average, non-continuous load profile which makes them unique compared to continuous loads. Essentially, these types of loads appear as transients, fluctuating heavily. Therefore, the prime power

supply used for these type of loads must be able to source large amounts of power in a short amount of time on demand. Conventional fossil fuel based electrical motor-generator sets can supply high power for these types of systems but the transient manner of operation causes the power quality to fluctuate during the consistent on and off switching. Therefore, it is required that a conventional generation sources be buffered so that they can maintain a power quality while these unique profiles are operated. One concept involves utilizing a hybrid energy storage module (HESM), that is constructed of both secondary lithium-ion cells and electric double layer supercapacitors [6, 7] to augment the conventional generation. A diagram of one proposed architecture, that is very simple and far from optimized, in which a HESM could be used is shown in Figure 2.

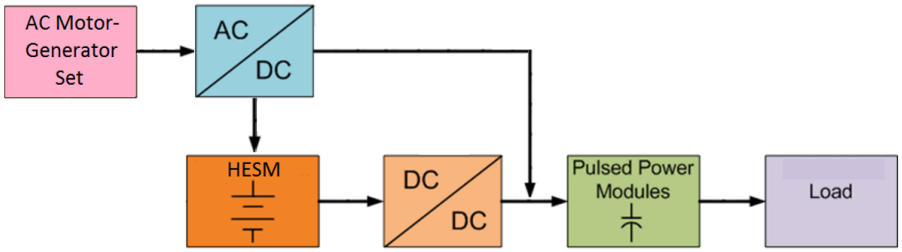

Figure 2: A flow chart modeling the proposed architecture in which lithium-ion batteries could be implemented. The HESM output will is regulated by a DC-DC power converter and the AC generation can be loaded by either the HESM or the load so that a base load is always maintained. During periods of high load, both the HESM and the generator can supply the load demand.

By combining the high energy density offered by lithium-ion batteries and the high power density offered by supercapacitors, a prime power supply that offers the best of both worlds is achieved. When combined with a generator, the HESM can act as either a buffer or a source enabling high generator efficiency to be achieved. Using active control during operation, the supercapacitors are able to source the leading edge of any fast transients of the load. During steady the operation, the capacitor can supply any

excess power that is above the desired operational rate of the batteries. Once steady state is achieved, the battery is able to output a constant power that is regulated using its own dedicated power electronics. The capacitors are able to maintain the DC bus voltage and keep the supercapacitors charged. During load inactivity, the generator continues to output its base power but into the HESM rather than the load. During recharge, the capacitors accept any transient currents from the generator, enabling the batteries to be steadily recharged at the desired rate. In this mode of operation, the batteries must be able to be discharged and recharged at high symmetric rates. Operation under these high rates in a transient mode has not been previously studied and therefore the work performed here attempts to answer how this mode of operation affects battery lifetime and degradation.

In other work performed at the University of Texas at Arlington's (UTA's) Pulsed Power and Energy Laboratory (PPEL), a 10 kW actively controlled HESM has been designed, constructed and validated as a testbed on which to study new topologies and control strategies. That HESM is shown photographically in Figure 3.

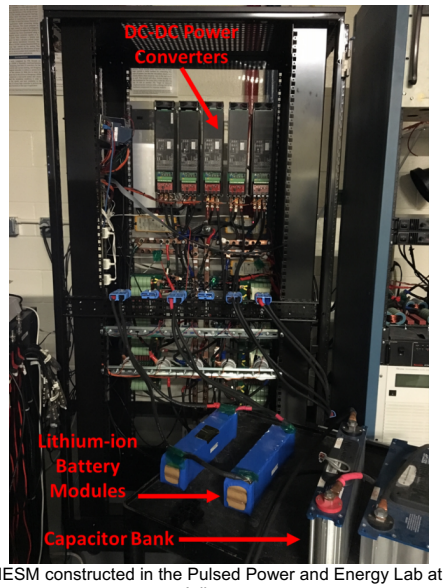

Figure 3: A picture of the HESM constructed in the Pulsed Power and Energy Lab at the University of Texas at Arlington.

How the lifetime of lithium-ion batteries is affected within a HESM has not been previously studied and it is necessary to understand these phenomena when designing HESMs for high rate applications. Aside from military applications, these types of topologies have relevance for use in electric vehicles (EVs). In the Navy's applications, safety remains most critical but size and weight of the battery are often considered more important than cycle life. This is not the case in EVs where cycle life is nearly equally important as safety due to the need to keep consumer costs low. However, if high rate pulsed operation brings a reduction in cycle life; it is valuable to understand what capacity fade characteristics are unique to it prompting the work performed here.

Selection of a suitable lithium-ion chemistry

When sizing a LIB for use within a HESM architecture, several different chemistries can be initially considered however, the unique power profile and safety concerns can quickly start to eliminate many of the available options. Historically, applications utilizing batteries as their prime power source have cycled them under continuous charge and discharge profiles at relatively low to modest rates well below the cells' maximum ratings. These metrics are vastly different from the rapidly transitioning load requirements of interest to the Navy.

Nickel Metal Hydrides and Lithium Cobalt Oxides

The energy dense chemistries typically used in consumer electronics, such as nickel metal hydride (NMH) and lithium cobalt oxide ($LiCoO_2$), are less than ideal for safe and reliable operation within prime power supplies for high-pulsed power loads because of their instability at the required high recharge rates. These chemistries become unstable at high temperatures that can be detrimental when deploying them at high rates onboard a mobile platform such as a Navy vessel. Though cooling can help significantly, the cooling requirements may become large themselves and become more of a requirement than an added feature. $LiCoO_2$ and NMH chemistries have 140 mAh/g and 200 mAh/g energy densities respectively making them some of the most energy dense battery chemistries on the market. However, the safety characteristics must be carefully considered since both are capable of violent and dangerous reactions if cycled under extreme conditions. NMH cells have been used previously to power plug-in electric vehicles due to their cheaper cost when compared to lithium-ion batteries [8, 9, 10]. However, this chemistry releases hydrogen gas when overcharged and typically

needs to be charged at very low rates to prevent capacity fade. The $LiCoO_2$ chemistry has high energy density stemming from its efficient placement of Li^+ and Co^{3+} ions in alternating (111) crystal planes of a rock salt-like lattice (Figure 4). However, due to oxygen reactivity below $Li_{0.5}CoO_2$, only half of the theoretical capacity can be practically utilized [11]. Additionally, like the NMH chemistry, $LiCoO_2$ cells cannot be overcharged since they are susceptible to overheating and eventually thermal runaway [12, 13]. Charging at currents above the nominal rating, often referred to as 1C, results in rapid capacity fade. Thus, the implementation of $LiCoO_2$ or NMH cells in high power pulsed sources is undesirable due to the inherent safety issues and the incapability of overcharging.

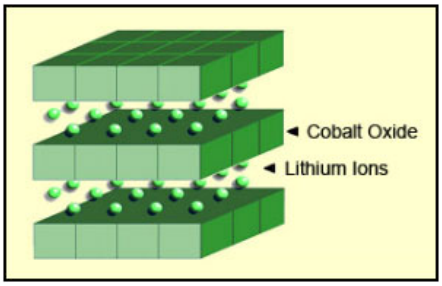

Figure 4: Diagram of the layered oxide crystal structure in lithium cobalt oxide cathodes [14]

Lithium Nickel Cobalt Aluminum Oxides

Previously, the Navy has researched the feasibility of using lithium nickel cobalt aluminum (NCA) oxide chemistries. This is the current chemistry utilized by Tesla Motors to power their electric drivetrains [15]. The NCA chemistry offers greater energy density than $LiCoO_2$ and has shown to be durable even under extreme conditions due to the extra stability obtained by the addition of aluminum [16, 17, 18]. Academic research into this chemistry has also yielded promising results when testing it for high

rate applications. However, this chemistry is not widely available and is normally used for very niche applications making the cost inherently high. Additionally, NCA chemistries are still cobalt based and therefore have similar safety concerns when it comes to thermal runaway. This chemistry is not necessarily off the table for high rate applications but it is also not the most desirable candidate.

Lithium Iron Phosphates

The most promising candidate comes with the olivine structured lithium-iron phosphate ($LiFePO_4$) chemistry (Figure 5). This type of cell has a reputation as a high power chemistry with great stability, even when pushed beyond its nominal limits [19, 20, 21]. It is also an inherently safe cell that has a far less violent reaction when abused unlike the thermal runaway events seen in the chemistries discussed above. This is made possible through the fabrication of nano-phosphate particles that are blended with carbon black to produce a low resistance cell with excellent cyclability and capacity retention. Because of these unique properties, it is often used in high power applications, many of which replace lead-acid batteries used in cold cranking amp roles [22]. This makes it an attractive candidate for use in a prime power supply for high pulsed power systems. There always must be something that is given up and in this case, the $LiFePO_4$ or LFP cells give up energy density, approximately 170 mAh/g, meaning that they are not as energy dense as the cobalt based chemistries [11]. In some regards, LFPs tend to behave more like supercapacitors. They have a nominal operating voltage that ranges between 2.50 V and 3.65 V that is very flat throughout its usable capacity. Since the size and weight of the overall HESM package is critical when being considered aboard mobile applications, the energy density trade off must be

taken into consideration as more cells are required to achieve higher voltages and capacities. Because of its promising features, the LFP chemistry was chosen as the focus for the research presented here.

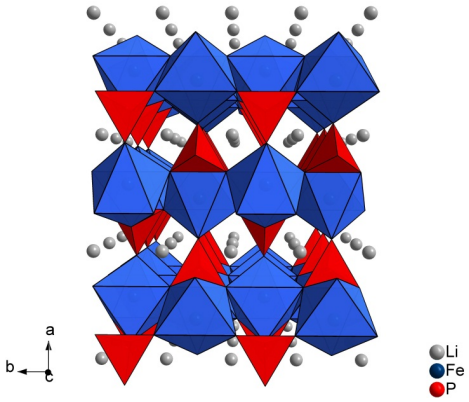

Figure 5: Diagram of the olivine crystal structure in Lithium Iron Phosphate cathodes [23]

Previous research of lithium-ion battery degradation

As mentioned previously, there is not a significant knowledge base discussing lithium-ion battery degradation characteristics when applied as power sources for high rate pulsed power loads. Research into the effects of cycling at rates well above the nominal rating (10C or greater) is also scarce [24]. Within the bodies of work found in the literature, there is no significant discussion of the aging mechanisms that high rate, pulsed operation induces within LFP cells. Instead, most authors present data that shows how capacity fade is accelerated under certain conditions with only speculations as to why aging occurs. These speculations are mostly derived from research data collected on laboratory-fabricated cells cycled at rates no higher than five times the nominal rate (5C).

A few researchers have published interesting findings, describing the degradation behavior of a cell as being highly dependent on the cycling profile used [25]. For example, Monem et. al. evaluated the effect of different charging profiles on the capacity fade and internal impedance of LFP cell [26]. Using electrochemical impedance spectroscopy (EIS) measurements and modeling, the individual impedance elements were identified and resistance values were obtained. As a conclusion, Monem et. al. reported that an LFP cell charged using a 7 A pulsed profile had a higher capacity fade after 500 cycles of operation than a continuously charged cell at the same rate. The ohmic resistance obtained from EIS modeling was found to be lower in the 7 A pulsed cell than the resulting ohmic resistance in the continuous. Thought they had this conclusion, there was no definitive form of reasoning provided as to why this was the case. Most importantly, they concluded that overall the best charging procedure was a pulsed profile with a low amplitude and the least number of pulses. In this case, the cell charge-discharge performance was enhanced and a decrease was noticed in the diffusional time constant. The delicate balance outlined in this paper clearly supports the need to study the effects of pulsed discharge on cell performance and impedance evolution. Moreover, based on previous research of the effects of high rate cycling and cycling profiles, it can be inferred that the pulsed conditions introduced in pulsed power systems will induce unique degradation behavior in lithium-ion cells.

Introducing common degradation mechanisms

When laying out a plan to investigate and identify the degradation characteristics in pulsed discharged lithium-ion batteries, it is necessary to first understand common degradation mechanisms that have been studied and previously identified by the

academic community. The reversible capacity of a lithium-ion cell is vital in determining its cyclability especially under heavy loading. Since lithium-ion batteries were introduced into the consumer market in 1991 by Sony, many studies have been conducted on the side reactions that contribute to capacity fade and internal resistance rise. Widely published degradation mechanisms for lithium-ion batteries includes solid electrolyte interphase development and growth, cathode metal dissolution, electrode cracking, gas generation, binder dissolution, and electrolyte decomposition [27, 28, 29, 30].

The solid electrolyte interphase layer

During the normal charge and discharge reactions of a lithium ion battery, there are many well-published side reactions that occur. These side reactions occur between electrolyte components, active lithium-ions, and electrode materials to form byproducts that do not contribute to usable energy storage. A typical lithium ion charging reaction involves the removal of lithium from the matrix of the positive electrode, normally referred to as the cathode, when an electrical bias above the activation threshold is applied. These freed lithium-ions move through the electrolyte solution, which is ionically conductive and electronically insulating, to the negative electrode or anode. There they recombine with electrons at the anode surface via exchange of charged particles through the double layer and intercalate into the anode matrix. The charge/discharge chemical reactions for a typical graphite anode and lithium metal oxide cathode system is shown below [11].

Cathode: $$LiM_yO_z \rightleftarrows xLi^+ + xe^- + Li_{1-x}M_yO_z \quad (1)$$

Anode: $$xLi^+ + xe^- + xC_6 \rightleftarrows xLiC_6 \quad (2)$$

During this exchange, reactions can occur at the interface between the electrolyte and electrode that decomposes the electrolyte solution and deposits solid byproducts on the electrode surfaces. These deposits form protective layers over the particles of the cathode and anode that protects them from further reactions with the electrolyte but also consumes active material. These layers of ‘protective material’ are commonly referred to as the solid electrolyte interphase layer or SEI (Figure 6). There has been extensive research conducted on the reactions and conditions under which SEI films form and the dependence of their composition on cycling conditions and the battery materials chosen [31, 32, 33]. The rate of growth of the SEI layer can also be influenced by the rate at which batteries are charged and discharged. Pulsed power applications introduce a new aspect that has never before been studied. Namely, what effect does a rapidly alternating pulsed load have on the composition of the SEI film and how fast it develops? Because the side reactions that form the SEI layer occur at the interface between an electrode and the electrolyte, it is reasonable to hypothesize that the rapid switching in polarity in the double layer from pulsing the cell will have an effect on the rate of formation of SEI compounds.

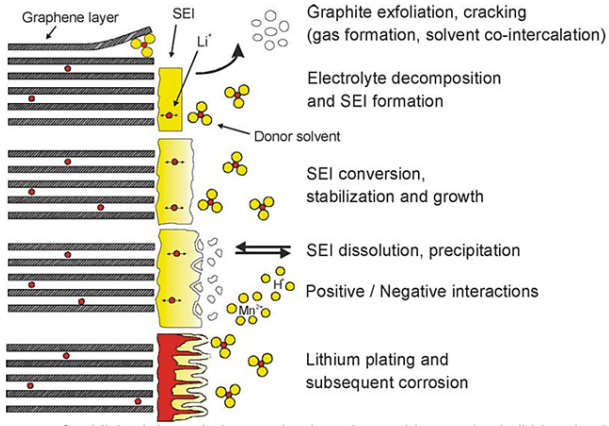

Figure 6:Diagram of published degradation mechanisms in graphite anodes in lithium-ion batteries [28]

SEI film compounds don't all share the same properties as far as ionic and electrical conductivity. Some researchers have divided the category of SEI surface films into two categories: SEI acting films and non-SEI films [34]. The difference between these two designations is that unlike normal SEI films formed, designated non-SEI films have low ionic conductivity and thus do not continue to allow the exchange of active lithium ions. While both types of films have been characterized as acting as a protective layer for the electrode material from further side reactions, non-SEI films have the added inert like behavior which can correspond to increases in internal cell resistance and power loss. Additionally, thermal stress can also influence the chemistry of the surface films. It has been reported by previous researchers that the storage of lithium-ion cells at elevated temperatures can adversely affect the stability of the initially formed SEI causing it to break down and possibly dissolve back into the electrolyte. This leaves the electrode material unprotected and new byproducts are allowed to form of the surface [35]. Some researchers have shown that the newly formed compounds are more stable than the previously dissolved meta-stable lithium alkyl carbonates [36]. While the new films may

be more stable under the high thermal stress, they also have higher ionic resistance that translates into power fade. It is unknown whether the added aspect of pulse cycling will cause new compounds to be formed that can adversely affect a cell's power capability. Furthermore, on the surface of the cathode particles, it has been observed that the oxygen from the metal oxide host structure can aid in the oxidation of the electrolyte [37]. Depending on the quality of the cell, the cathode particles can react with degraded electrolyte salts to form compounds such as LiF on the surface [38]. The surface of the cathode particles can also undergo polymerization and/or transesterification to form polymeric films on the positive electrode surface. The reactions that form these compounds also creates gases like carbon dioxide that bubbles to the surface of the solution. Some researchers have discovered a linear correlation between the amount of gas produced in the cell to the capacity fade observed. All in all, there are a plethora of side reactions which can create byproducts forming a surface film on either electrode. This film can be an absorber of active material and/or impede the movement of lithium-ions corresponding to an increase in cell internal resistance.

While research into the formation of SEI films has been mainly focused on the anode side, it is not unheard of that one would form on the cathode side as well. Thus, the surface chemistry of both the anode and cathode should be studied initially to determine the effects of pulsed discharge on each. Specifically, three things should be determined when studying the surface films formed in pulsed discharged cells. These include identifying the concentration of compounds, measuring their thickness, and identifying the underlying side reactions. Overall, this information is vital not only towards the

proper selection of a cell for pulsed power supply but also for the advancement of future high power battery technologies.

Crystallographic changes in electrodes

While the growth of SEI layers are the degradation mechanism most widely researched, structural and crystallographic defects that can form during cycling are also important to discuss in high power applications. During normal operation of a lithium-ion battery, there can be volume changes in both electrodes associated with the insertion and removal of lithium ions. In addition, if decomposition products, such as oxidized electrolyte products form between layers of the anode, they can cause the cell to exfoliate or form high levels of porosity. In both the anode and cathode, micro-cracking can form in cells that are mechanically stressed by cycling outside their normal voltage ranges. These mechanical defects will lead to a decreased number of available active lithium sites therefore increasing capacity fade (Figure 7).

Along with the mechanical defects that occur during cycling, changes in atomic order can also occur that distort the lattice of both electrodes. In some cases, when lithium leaves an electrode, there are large shifts in the electrode's crystal structure. These phase shifts occur because lithium metal is no longer a part of the crystal structure and therefore the matrix shifts to a more stable form.

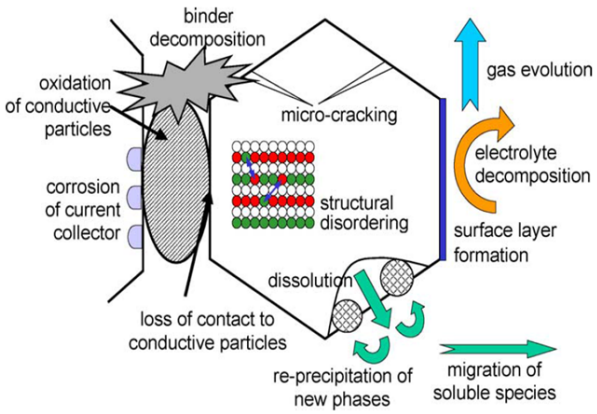

Figure 7: Diagram of published degradation mechanisms of metal oxide cathodes in lithium-ion batteries [28]

For example, in lithium nickel oxides, the monoclinic crystal phase shifts to a hexagonal structure when lithium is released causing large volume shifts that adversely affects the capacity if the phase shift becomes permanent [11]. In cases where a high rate or high order of delithiation occurs (high charge state), some areas of cathode particles may undergo permanent phase shift. These sites can no longer reintegrate lithium ions into their matrix and that phase ceases to be an appropriate host. Secondly, another commonly discussed degradation mechanism is metal dissolution from the cathode host structure [37]. Metal dissolution occurs when transition metals that makeup the cathode host structure, dissolve into the electrolyte solution and are carried across the separator to the anode where they are deposited. This can cause capacity fade in two ways. The first is that it damages the cathode host structure causing permanent phase changes leading to the precipitation of new phases that can have a higher resistance. The second involves dissolved metals that can be deposited in the anode structure and become favorable sites for electrolyte decomposition. At the very least, these sites remove places where active lithium could have been stored. The deposited metal and

any degradation product attached to it can also be a source of mechanical strain on the electrode material similar to the effect described above. Therefore, any high stress cycling profile may exasperate these phenomenon creating more favorable conditions for them to occur.

Overall, it is important to note the effects of mechanical and chemical impurities which derive from both a physical expansion via intercalation of lithium and from the permanent precipitation of new phases via structural reordering or metal dissolution. All of these factors can lead to capacity fade and increased cell resistance. Many of these mechanisms can be accelerated by high rates and high temperatures but it is unclear whether they are affected by pulsed profiles. It stands to reason that the constant reversal of ion flow within a cell through repeated pulsed charge and discharge may create fatigue-like stress fractures on the electrodes. The reordering of atoms in the cathode lattice may increase if the direction of lithium ions is constantly reversing back and forth. Answering these questions is an aim of this work.

Comment [DW1]: Homey say what???

Degradation of non-active cell components

Cell components, which do not contribute to the energy storage reaction, are also susceptible to degradation as the cell is cycled. Components such as the electrode binders, current collectors, and conductive additives can react with active cell materials when the cell is stressed beyond its rated limits. While these types of degradation may not affect the usable capacity of the cell, they can affect the amount of contact that the conductors have with the electrode materials. This leads to an increase in the cell's electrical resistance and therefore may affect the power output of a cell. These mechanisms are discussed in more detail below.

When stretching the charge capability of a cell, the binder that holds the electrode particles together may begin to decompose. Binder material in lithium ion batteries serves mainly to keep all cell components connected and ensures good electrical contact between them. Typically, in commercial cells, the anodic binder is a mixture of carboxymethyl cellulose and styrene-butadiene rubber while the cathode binder is polyvinylidene fluoride (PVDF). In normal operation, these binders are stable and do not react with any cell components or diffuse within the electrode. However, it has been reported that at temperatures above 80°C, surface films contain more inorganic compounds and the binder materials begin to break down affecting the contact resistance between particles and the conductive material [28]. On the cathode side, PVDF binder has been known to decompose and be a major cause of aging in tested $LiFePO_4$ electrodes [39]. PVDF binder can also diffuse to the surface of the positive electrode and hider the movement of lithium ions. It is not entirely clear what specifically causes the binder dissolution as some researchers have tested $LiFePO_4$ cathode at temperatures above 90°C, demonstrating that the cell was still able to be cycled [40]. In the case of cells that couldn't be cycled due to binder dissolution, the binder material was found in high concentrations at the surface of the positive electrode and even on the negative electrode surface [28]. Because the Navy's application requires not only high rate operation but also utilization of the maximum power capability of the cell, it is imperative to observe whether there is an increased amount of binder material on the surface of electrodes after the cells have finished testing.

Current collectors in lithium-ion batteries can also degrade by corroding in the electrolyte solution. Corrosion becomes more likely in aluminum cathode current

collectors when the cell is near or above 100% state of charge (SOC) where the oxidizing potential is high [41]. In the anode, the common copper current collector is susceptible to micro-cracking at low SOC and when overdischarged. When it comes to the aluminum collector, researchers have identified that pitting occurs under the right electrochemical conditions [42, 43]. They also observed that the pits were filled with corrosion byproducts forming nodules on the surface. When scanning the surface chemistry using x-ray photoelectron spectroscopy, they found that there was a far higher concentration of fluorine compared to lithium and phosphorous stemming from the deposition of $LiPF_6$ salts from the electrolyte. This was independent of the mixture of solvents in the electrolyte solution. When the current collector corrodes, it raises the internal resistance of the cell due to the increased contact resistance between the collector foil and the electrode material mixture. Similar to this, the carbon additive (typically carbon black) that is used to promote conductivity between metal oxide cathode particles can oxidize further increasing the contact resistance between lithium metal oxide particles. The state of health of the conducting materials and binders needs to be studied under pulsed profiles using surface chemistry and electrochemical impedance techniques to identify how surface compounds develop on the electrodes and how they contribute to impedance growth.

Hypothesis to be investigated

Research in the field of lithium-ion batteries is extensive and branches into many applications. As previously discussed, there is little published research evaluating how lithium ion cells degrade and age when used to drive high pulsed power profiles. Based on what has been previously published, there is sufficient evidence to support the idea

that the implementation of a pulsed discharge profile on a lithium-ion battery will have a unique effect on a cell's capacity fade, surface chemistry, and impedance evolution. Most importantly, the degradation mechanisms that cause the cell to be rendered useless for the chosen application may be unique in pulsed cells compared to those cycled continuously at high rates. Specifically, the hypothesis, based on previous work, is that a bipolar-pulsed profile induces the preferential formation of high ionically resistant compounds that cause cells to degrade faster than those discharged at similar rates continuously. The work performed here is aimed at validating which specific degradation mechanisms, that were introduced above, are more favorable under high rate pulsed loading due to the rapid switching of polarity. While many of the techniques that are used to characterize cells and their electrode materials are similar to those used in everyday battery research, there are challenges associated with using them on commercial cells since there is no control over the building process. In many battery aging studies, the cells are custom built and therefore diagnostics are easier to conduct on the cells. To overcome these challenges, the common characterization techniques have been enhanced using custom apparatuses, equipment, and procedures. These additions have made it possible for a proper degradation study to be performed on commercial cell materials and systems with minimal effects. Steps have been taken so that full characterization of cell materials exposed to high rate pulsed loading could be performed. Several identical cells have been cycled using a unique, high rate, bipolar pulsed profile as well as similar high rate continuous procedure to correlate the changes observed in the materials to the type of procedure used. Once cycling was completed on each cell, electrode samples were extracted from various locations throughout the

cells jelly roll and studied using various analytical techniques. Additionally, a novel in-situ three-electrode measurement technique has been developed for use on commercially produced cells so that EIS and differential capacitance measurements can be made on each respective electrode. Through this work, degradation phenomena unique to high rate pulsed discharge have been identified.

Comment [DW2]: Read through this for grammar. There were soooooo many run-on sentences. Its ok to take a breath!!!!

Chapter 2: High-Frequency Pulsed Discharge

Much of the work documented here was built upon work initiated by Biju Shrestha from 2010 to 2013 [44, 45]. Shrestha cycled a few different identical 3 Ah LNCAO cells at high rates under both pulsed and continuous profiles. The results showed that the pulsed cell aged faster than an identical cell cycled at the same average rate in a continuous manner. In high power systems such as hybrid electric vehicles and grid energy storage modules, high frequency switch mode power electronics are placed between the module and the load that act as power regulators [46, 47, 48]. These voltage regulators extract current from the batteries in the form of high frequency pulses with varying duty cycle. The need to source high currents at high-pulsed rates begs the question of how this type of repeated operation will impact the life of the batteries. To study these related phenomena, Shrestha developed a novel test bed that is capable of switching power from a battery at high rates in a pulse width manner. A novel load was required as high frequency switching is nearly impossible using the vast majority of industrial cyclers that utilize mechanical relays to alter the load. As previously outlined, the majority of lithium-ion battery applications operate under continuous usage [49, 50]. The design of Shrestha's novel test stand (Figure 8) has been previously documented and the reader is referred to those articles for a more in depth description of its design and operation [51]. In short, the load utilizes fast switching MOSFETS arranged in parallel to create a high pulse width modulated discharge profile. Unlike industrial cyclers, the discharge current in the test stand is completely controlled by the overall resistance of the stand and the state of charge of the battery. Therefore, the output current changes as the cell's voltage decays.

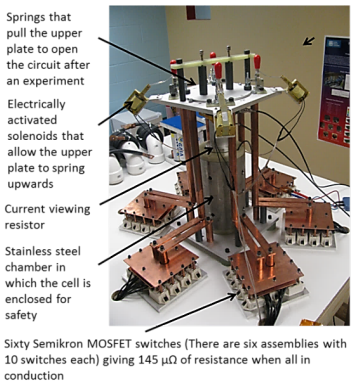

Figure 8: An image of the high frequency pulsed test-stand constructed in the Pulsed Power and Energy Lab

Shrestha's work was only aimed at studying the effects of high rate pulsed discharge and does not include any affects that may be introduced by high pulsed recharge from an electric generator. Three identical 4.1 V, 3.0 Ahr, $LiNi_xCo_yAl_{1-x-y}O_2$ cells were cycled under three different profiles respectively: a high rate pulsed discharge, a high rate continuous discharge, and a nominal 1C discharge profile [52]. The high rate pulsed discharge cell was cycled using the novel low impedance test stand. One cell was discharged at high pulsed rates but recharged using a nominal 1C, constant current (CC) – constant voltage (CV) procedure. The novel test stand was used to discharge the cell at a peak C rate of roughly 83C. The discharge frequency was 10 kHz and a 50% duty cycle was utilized. The second of the three cells was cycled at a continuous elevated discharge rate, equal to the average C rate recorded in the high rate pulsed discharge experiment, in attempt to discern the impact which the pulsed nature of the discharge has from the average high C rate itself. That particular cell was discharged using a 25C CC procedure and recharged using a 1C CC – CV procedure. Finally, the third cell is a control which was both charged and discharged using a 1C, CC – CV procedure. All three cells were cycled between 4.1 V and 1.5 V. Periodic 1C 'baselines'

were performed to map the capacity fade of each respective cell as a function of the number of cycles performed. The baseline procedure consisted of a CC-CV charge at 1C (3.0 A) to 4.1 V with a 0.3 A cutoff followed by an potentiostatic EIS collection which swept varying frequencies from 20 kHz to 10 mHz with a 10 mV amplitude. Then the cell was discharged using a CC-CV, 3.0 A procedure, again with a cutoff of 0.3 A. Another potentiostatic EIS was conducted at 0% SOC after the discharge was completed. There was a one-hour rest period between each of the charge/discharge steps before EIS was taken to allow the cell to reach equilibrium. This baseline metric was performed to ensure that there was a fair comparison of the capacity fade of all three cells throughout testing. The EIS data was used to evaluate the internal resistance evolution in each cell. An equivalent circuit model was constructed to simulate the spectrums collected from each baseline procedure and values were obtained for the electrical elements in the model. These modeling efforts were the first performed by the author of this dissertation and served as the foundation for the work to be discussed later. When modeling each cell's equivalent circuit, the change in each element's value in each baseline procedure was aid in identifying the electrochemical degradation phenomenon responsible for the observed capacity fade of each cell.

Degradation behavior observed from the pulsed discharge cell

As previously mentioned, the discharge rate of a cell evaluated using the novel test stand varies as the voltage and SoC decays due to the load's constant resistance nature. Figure 9 and Figure 10 show samples of the voltage and current profiles recorded during the 3rd and 400th elevated pulsed discharge cycles, respectively.

These plots show that it takes roughly 140 s for the cell to be discharged to 1.5 V, as per the data sheet that lists 1.5 V as the lowest discharge voltage when the cell is discharged at high rate. A better representation of the pulsed discharge behavior is shown in the rightmost portion of each figure, in which a zoomed in view of the first 400 µs of each waveform can be found.

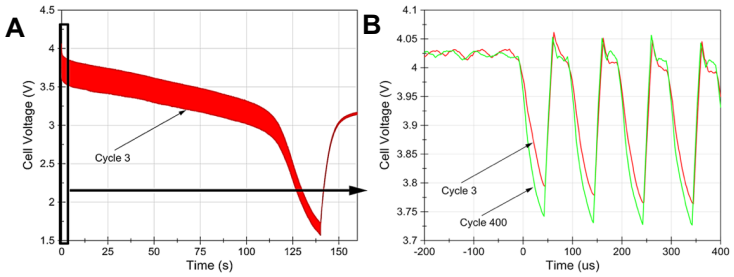

Figure 9: A) Voltage profile measured during discharge cycle 3 and B) a zoomed in plot of the first 400 µs during cycles 3 and 400 respectively

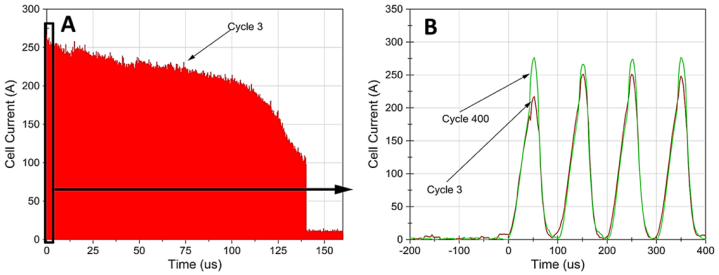

Figure 10: A) Current profile measured during discharge cycle 3 and B) a zoomed in plot of the first 400 µs during cycles 3 and 400 respectively (right)

The jagged nature of the waveforms is a result of the digitization of the signal. As can be seen, the peak current at the start of the discharge is just over 250 A (83C). By the end of the discharge, the peak discharge rate decreases to just over 100 A (33C). The average discharge current, when the duty cycle is taken into account, is just over 75 A

(25C). Figure 11 shows the thermal profile measured during cycles 3 and 400 respectively.

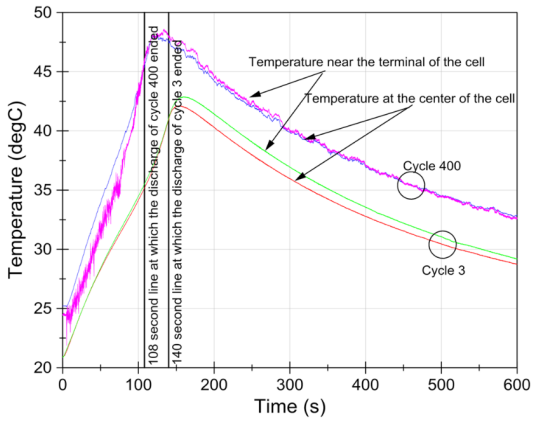

Figure 11: Thermal profiles measured near the center and near the terminals of the cell during the 3rd and 400th cycles respectively

During the discharge, the cell's temperature peaks just below 50^{o}C. While temperature effects were not a focal point of this particular group of tests, this temperature is within the manufacturer's suggested limits. Figure 12 shows the mapping of the 1C discharge capacity measured after every 100 cycles of elevated pulsed discharge using the baseline procedure.

The pulsed cell's initial capacity was recorded as 3.13 Ah at 1C and it decreased to 2.49 Ah after 400 cycles of pulsed discharge. This corresponds to an approximately 20% capacity fade, the industry standard for declaring that a cell needs to be replaced. Thus, in just 400 cycles of pulsed discharge cycling at a 50% duty cycle, the cell has faded to the point that replacement is needed. EIS can be a powerful tool in determining the electrochemical components responsible for capacity fade behavior in a cell. The

spectrums collected at 100% SoC in the baseline procedure for the pulsed cell are shown in Figure 13.

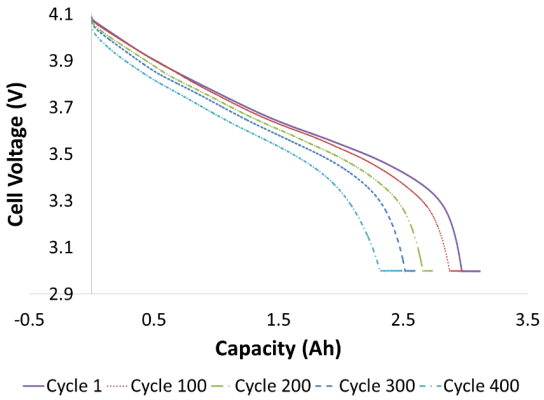

Figure 12: 1C baseline cell capacities measured after each 100 respective high rate pulsed discharge cycles

An EIS spectrum can be divided into four parts – the inductive tail (IT), mid frequency semi-circle (MF), low frequency semi-circle (LF), and the Warburg impedance (WI). The inductive tail is a higher frequency response shown on the left hand side below the zero of the y-axis. The inductive impedance is attributed to the small inductive loop created by the windings of the jellyroll and are negligent when observing aging phenomena. The displacement in the spectrum along the point where the curves cross the x-axis represents the rise of real impedance in the cell, a portion of which is made up of the resistance encountered as ions traverse the solid electrolyte interphase (SEI) layer, the bulk electrode impedance, and the ionic resistance of the electrolyte.

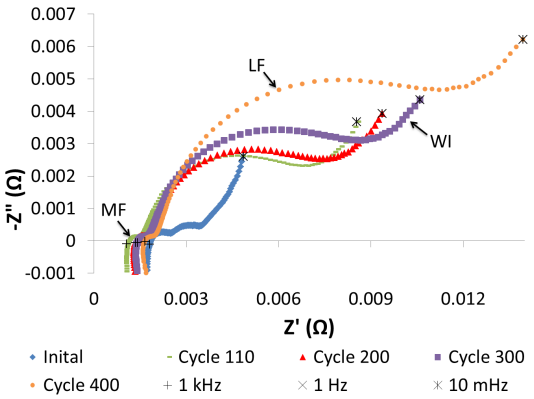

Figure 13: Nyquist plots measured near 100% SOC and 4.1 V after each 100 respective high rate pulsed discharge cycles

From the plot, it can be observed that the real impedance initially decreased, during the first 110 cycles, as the cell settled in. This is likely due to improved stability of the SEI layer, as well as the repeated ion diffusion processes, allowing ions to more easily intercalate. After roughly 110 cycles had been performed, the real impedance started to increase significantly. Despite the growth, after 400 cycles, the real impedance is still just slightly lower than its original value. Keep in mind that after these 400 cycles the capacity of the cell was 80% of its initial value meaning there is a decrease in the amount of lithium ions which are contributing to the energy storage process. In the analysis of the EIS curves that follow, Croce's model has been adopted [53], as it was by Ning, et. al. [54]. At low frequencies, shown in the far right section of Figure 13, the 45° line (typical characteristics of Warburg diffusion region) accounts for the solid-state diffusion of lithium ions in the bulk electrode material while the semicircle loops in the LF and mid-frequency (MF) regions corresponds to the respective electrode-electrolyte interface resistances [55]. A mild decrease in the width and height of the MF semicircle is observed, which may indicate a gradual growth of the SEI layer or minute structural

damage to the active particles on the cathode surface. There is also, however, a vast growth in the width and height of the LF semicircle indicating that there is a large increase in charge transfer resistance which includes both the double layer and SEI impedances of the anode and cathode. The charge transfer impedance could imply that the rate at which lithium ions can be de-intercalated from the anode and re-intercalated into the cathode during discharge decreases exponentially. Keep in mind that without curve matching and modeling, this analysis only gives us a simple idea of high rate pulse discharge degradation characteristics. Using EIS, the proper way to study individual electrodes to find the dominant degrading electrode is to use a three electrode setup with an attached reference electrode in a similar electrochemical environment.

It was previously mentioned that during battery cycling there is a natural buildup of precipitates that form on each of the electrode/electrolyte interfaces, especially near the anode making up the SEI layer. The data from the pulsed NCA cell suggests that cycling at a high-pulsed discharge rate accelerated the growth of the SEI and the corresponding diffusion of SEI precipitates into the electrodes that eventually blocks the diffusion of lithium ions. This increases the charge transfer resistance, thus decreasing the total usable capacity. It is also to be expected that a higher amount of electrode cracking occurs when the battery is cycled at high rates due to higher mechanical stress, of which are induced through more rapid volume expansion and contraction. The occurrence of cracking decreases the usable intercalation volume and increases the surface area on which passivation films form and grow. Analysis of this cycling condition

has shown that one interface degrades substantially more than the other when cycled using a pulsed discharge procedure.

Degradation in high rate continuously discharged cells

The second cell to be discussed has been discharged at a high continuous rate. The cell was cycled 400 times with the intent of comparing the results from this cell to those obtained from the high rate pulsed cell. This cell was cycled using a Maccor 4000 series industrial cycler that has five channels rated at 5.0 V and 240 A each. The 25C (75 A) discharge rate was chosen so that the continuous discharge rate of this cell is equal to the average discharge rate of the high rate pulse discharge over the course of its lifetime. While the choice of the 25C rate will leave unanswered questions, due to the large difference in peak rates between this cell and the pulsed discharged cell, the initial aim of this cell was to demonstrate the impact of average current rates. During the discharge, the cell's temperature peaks just below 34°C, which is roughly 16°C lower than the peak temperature during the high rate pulsed experiments (Figure 14). This is sensible given the substantial difference in I^2R losses. Figure 15 shows the 1C discharge capacity measured after every 100 cycles of elevated continuous discharge. Initially, the cell was able to supply 2.98 Ah at 1C, however, after 400 cycles the capacity decreased to 2.81 Ah, meaning a capacity fade of 5.7% occurred. These results suggest that pulsed discharge may affect cell aging though it is not perfectly conclusive since the peak C rates and temperatures, respectively, are slightly different between the pulsed and continuous cells.

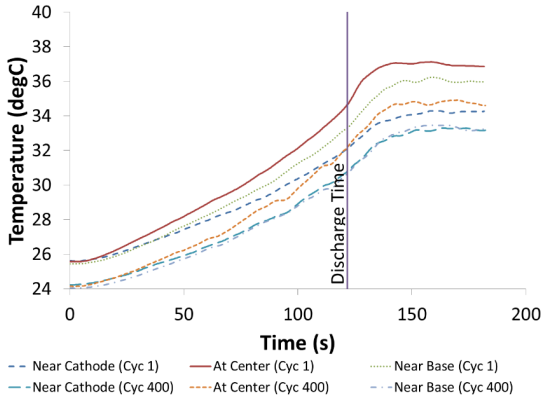

Figure 14: Thermal profiles measured during the 1st and 400th cycles respectively during elevated continuous discharge at 25C

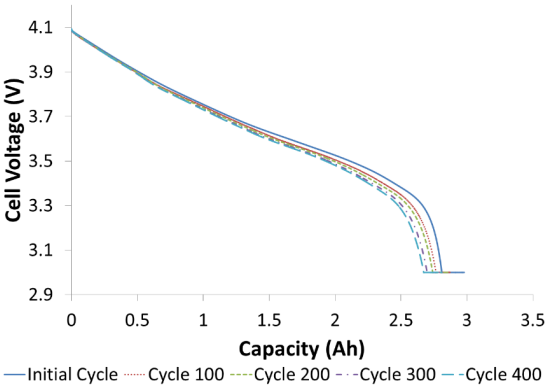

Figure 15: 1C Cell capacity measured during baseline procedure after elevated continuous discharge at 25C rate

From the EIS spectrums collected, shown in Figure 16, it is observed that the MF semicircle remains fairly consistent indicating that there is not much of an increase in the electrodes' passive film formation. The width and height of the low frequency semicircle increases considerably with cycle number, indicating an increase in internal charge transfer resistance. However, the degree to which the imaginary and real impedance increase in the continuous cell is far less than the magnitude of the evolution of the same region in the pulsed cell. Essentially, the EIS data indicates that the act of

fast switching may promote the MF impedance evolution accelerating the fade of available capacity in the cell.

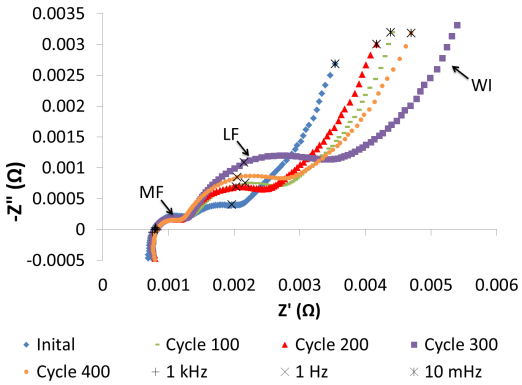

Figure 16: Nyquist plot at 100% SOC and 4.09 V after respective high continuous rate discharge cycles

Degradation observed at the nominal rate

A control cell was cycled using a 1C CC-CV recharge procedure and a 1C CC discharge procedure. The 1C baseline discharge capacity curves measured after every 100 cycles respectively are plotted in Figure 17. As expected, there is no appreciable capacity fade up to 400 cycles. EIS spectrums shown in Figure 18 confirm that there is minimal degradation with the impedance evolving only a small margin on the real axis. Both the LF and MF semicircles show no appreciable change indicating only minute changes to the cell's electrochemical state.

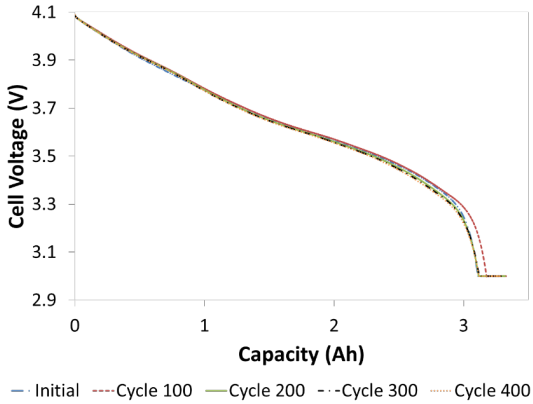

Figure 17: 1C baseline cell capacities measured after each 100 respective 1C control cycles

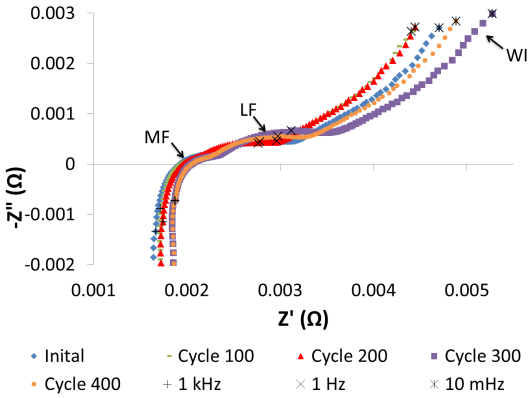

Figure 18: Nyquist plot at 100% SOC and 4.1 V after respective nominal, 1C rate continuous discharge cycles

The lack of change in the cell capacity or EIS response also indicates that the 1C recharges performed on the high rate pulsed discharge cell nor the high continuous rate discharge cell, had any measureable impact on the capacity fades observed on those two cells respectively. Therefore, this cell stands as an accurate reference to compare the degradation and impedance evolution observed in both the pulsed and continuously discharged cells, respectively. In the following sections, an analysis of each cell's

capacity fade and circuit element changes will be presented as a means for explaining each cell's impedance evolution.

Relating differences to physical phenomenon

When comparing the differences in capacity loss between the three NCA cells, as shown in Figure 19, it can be concluded that the elevated rate pulsed discharge has a greater impact on aging compared to elevated rate continuous discharge, if an average discharge rate is maintained.

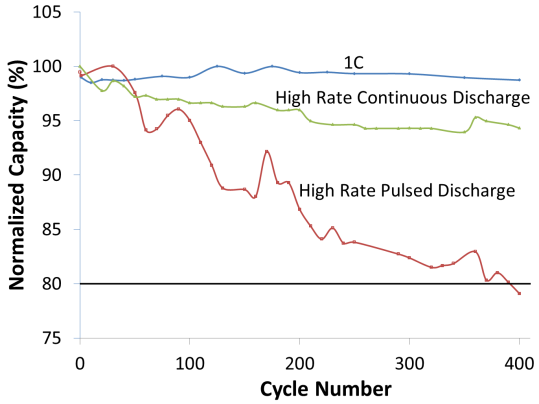

Figure 19: 1C baseline cell capacities measured after every 100 cycles of respective test cycles

It is reasonable to infer that the repetitive on and off discharge procedure induces additional fatigue on the cell since there are short moments of electrode relaxation followed by moments of extreme stress. The oscillation between loading and unloading of the battery creates a fatigue stress in the electrodes as compared to the constant loading of a continuously discharged cell. Damage to the electrodes during the high rate pulsed discharge procedure decrease the amount of viable sites for the Li ions to intercalate, thereby reducing the usable capacity. Based on the EIS spectrums from

each of the three cells, it is also a possibility that side reactions are more favorable under pulsed discharge conditions. Therefore, the SEI layer on the surface of the anode grows at an accelerated rate with respect to the high rate continuous discharge cell. The control cell cycled at nominal rates shows no indication of aging after 400 cycles, thus it can be determined that the aging measured on the high rate pulsed discharge cell and high rate continuous discharge cell is the result of only the effects induced by the respective high rate discharge profile. Calculating the percent capacity lost under each condition, the degree of accelerated degradation in the high rate pulse discharge cell is apparent. Over a fifth of the cell's original capacity was lost in the pulse discharged cell compared to just 5.68% in the high rate continuous cell. The sinusoidal nature of the capacity loss curve is a function of rest time between cycles. The time between cycling would often go a few days, or even weeks depending up on the laboratory schedule. It was observed that if a long period of time had lapsed between cycles, the capacity extracted from the first cycle performed after the rest would actually give more capacity than the cycle previously conducted. This is believed to be due to the cell having time to stabilize, allowing for lithium to fully intercalate into the anode. Also, the long rest period allows the soluble precipitate on the surface of the electrodes that are deposited during cycling to dissolve back into the electrolyte. This causes the lithium on the precipitate to return back to electrochemical process, thus increasing the capacity. However, none of this evidence alone is viable enough to make any conclusions as the specifically why the capacity fade in the pulsed cell is accelerated. The EIS spectrums collected on each of the cells can be used to derive information about physical phenomenon within the cell based on an equivalent circuit model of the entire cell. Through this method, viable

theories could be made about the differences in physical degradation traits within the cell and a direction for future experiments could be mapped out.

Modeling two electrode EIS spectrums

Analysis of a cell's periodic EIS spectrum provides insight to its degenerative behavior. Though useful for providing hints of what is occurring internally, a two-electrode EIS measurement does not provide enough specific information to indicate how individual elements within the cell is changing. This information would be valuable in discovering how different cycling scenarios change the manner in which cells degrade. Using ab equivalent circuit model of the cell under test, curve fitting tools can be used to estimate the parametric changes within the cell. Individual components and their impedances are calculated by running an equivalent circuit model against the collected EIS data. Each components impedance variation can be plotted against the cycle number to estimate the procedures impact on ESR. Since the majority of impedance evolution occurs in the mid frequency semicircle, the high frequency loop below the x-axis is not considered in this modeling analysis. Instead, the analysis begins at the point where the spectrum crosses the x-axis, representing the cell's real impedance.

Each equivalent circuit component represents a physical element in the cell. For example, resistors are used to model the cell's ohmic impedance in various portions of the cell. Another example involves using RC circuits to represent the capacitive double layers at each electrode/electrolyte interface. Because EIS is complex measurement, real and imaginary impedance components exist. Below is a list of some of the electrical components used in this type of modeling and their impedance response, Z, as a function of frequency.

Resistor:	$Z_R = R$	(3)
Capacitor:	$Z_C = \frac{1}{2\pi f C}$	(4)
Inductor:	$Z_L = 2\pi f L$	(5)
CPE:	$\frac{1}{Z_{CPE}} = Q°(j\omega)^n$	(6)
Warburg Element:	$Z_W = \frac{A_W}{\sqrt{\omega}} + \frac{A_W}{j\sqrt{\omega}}$	(7)

Where,

CPE	Constant Phase Element	j	Imaginary Number
Z_R	Resistive Impedance	A_w	Warburg Coefficient
Z_C	Capacitive Impedance	n	Capacitive Degree
Z_L	Inductive Impedance	Q°	Admittance at 1 rad/s
Z_{CPE}	CPE Impedance	f	Frequency
Z_W	Warburg Impedance	ω	Angular Frequency

Using these components, it is possible to model the 3 Ah NCA cells studied earlier, shown in Figure 20. The periodic EIS measurements are fit to the model shown in Figure 20 and the component values are extracted.

In Figure 20 the inductor (L) represents the inductance of the jelly roll. The initial resistor (Rs) represents the natural impedance of the electrolyte and electrical contact resistance within the cell. Comparison of this equivalent model to similar ones that have been previously published, it is inferred that the first of the RC parallel networks (Rp1 and C) is commonly assigned as the impedance contribution from the SEI layer and the resulting double layer formed at both electrode/electrolyte interfaces.

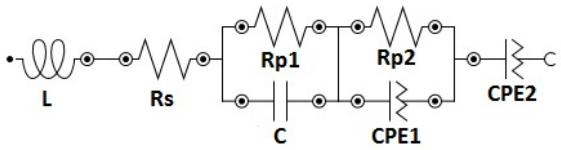

Figure 20: Equivalent circuit model used to simulate the impedance evolution of the NCA cell

Evolution of the double layer impedance relates to the changing difficultly of charge transfer at both electrode surfaces. The second RC parallel contains a constant phase element (CPE1) which represents an imperfect capacitor. If modeling is conducted using a traditional capacitor, inconsistencies between the model and real spectrum arise. These problems are solved with the use of a CPE. This indicates that this parallel RC represents a phenomenon that initially has both a capacitive and resistive nature but then changes to a purer resistive behavior as the cell ages. The final CPE (CPE2) at the far right of the circuit model represents the supplementary capacity of the cell or its ability to allow active material to diffuse through the lattice of both electrode particles. Traditionally, there is a Warburg element that is used in its place to model the diffusive properties of the anode and its double layer. The CPE acts as a similar element that allows for some variation in its behavior as the cell degrades. To validate that this model matches the EIS data collected from the NCA test cells, a spectrum generated by the model and one taken from the initial scan of the NCA pulsed cell is plotted together in Figure 21.

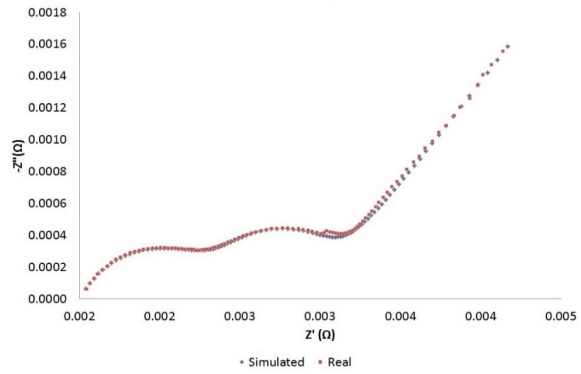

Figure 21: Simulated EIS curve fitted over real EIS data taken from an NCA cell after 1 cycle of pulsed discharge

From Figure 21, it is observed that the two curves are well matched proving this is an accurate model of the cell being studied. Using this model, the EIS measurements collected during each baseline procedure were simulated to collect the component results. The changes in the component values observed in the high rate pulsed and continuous cells, respectively, are plotted in Figure 22 from both pulse and continuous discharged cells. The inductive and capacitive elements do not vary appreciably in impedance from the initial baseline to the final baseline taken after 400 cycles for either the pulsed or continuous scenarios. Because of this, the focus on what is changing is turned to the three resistive elements and the two CPE elements. Rp1 from the pulsed cell has a much steeper increase in impedance compared to the other resistors in the pulsed cell or the RP1 from the continuous cell. Additionally, in both scenarios, the impedance contribution of CPE1 is always much greater than that of the CPE2 by several orders of magnitude. These results therefore indicate that it is the changing surface conditions of both electrodes that dominate the change in cell impedance.

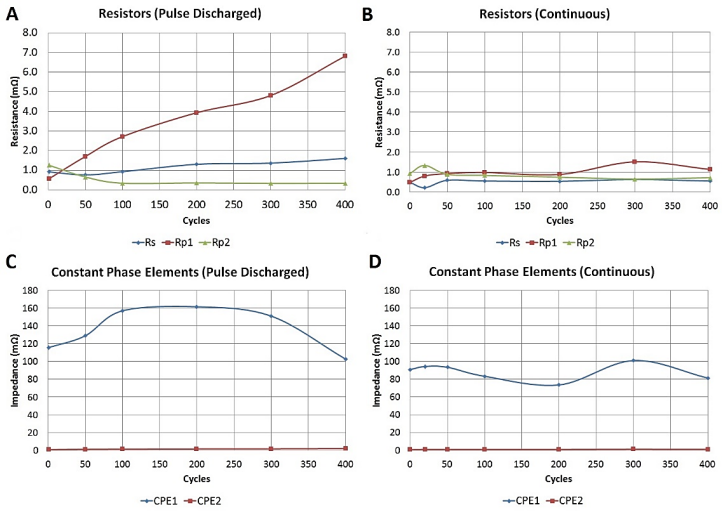

Figure 22: Modeled impedance evolution of A) pulse discharged cell resistors, B) continuous discharged cell resistors, C) pulse discharged cell CPEs and D) continuous discharged cell CPEs

There is a significant way the impedances change when comparing the pulsed and continuous high rate cells to each other. The resistor, Rp1, in the pulsed cell experienced a linear impedance rise whereas the continuously discharged cell has little evolution. The maximum-recorded impedance contribution from Rp1 is approximately 300% higher in the pulsed cell that was recorded during the last EIS measurement taken at 400 cycles. The maximum impedance in CPE1 for the pulsed cell is approximately 60% higher than the same component from the continuous cell. Additionally, the pulsed cell experiences a consistent increase in resistive impedance while the continuous cell shows fluctuations. This may be explained by the fact that during pulsed discharge, the electrodes experience a cyclic fatigue stress instead of a constant contraction or expansion of the lattice structure. It is possible that this could permanently damage the electrode leaving vacancies in the structure and releasing small pieces of electrode into the electrolyte mixture. These defects could open up new

surfaces on which SEI films can grow, causing more stress on the lattice of either electrode. These mechanisms retard the rate of diffusion of lithium ions from the cathode and diminish the integrity of the double layer at the electrode surfaces. Therefore, increased internal cell resistance in the NCA cell is due to a combination of SEI growth and a growing inefficiency of transporting ions through the double layer. It cannot be stated which phenomenon is dominant based on this two-electrode model but a common theory amongst battery researchers is that impedance rise stems mainly from the growth of SEI at the surface of one of the electrodes, normally the anode, which affects the amount of surface area available for lithium ion transfer. If the surface area at one or both electrodes reduces due to heavy SEI passivation, the capacity of the double layer formed at the surface would degrade accordingly. This is conflicting to other researchers who have observed that the SEI acts a protective layer as described in the introduction.

A characterization of the NCA cell's electrode materials to help confirm these theories should focus on the lattice distortions and the changing surface chemistry/morphology of both electrodes. However, the manufacturer of these cells didn't permit them to be dismantled and thus studying the surface chemistry wasn't possible. At this point, it was decided that future testing needed to be focused on the principle chemistry, lithium iron phosphate. Now that the degradation behavior for high frequency operation has been initially characterized, it is clear that the use of lithium-ion batteries in high pulsed rate applications opens up a new avenue of research that has never previously been touched upon by other researchers in the battery industry.

Chapter 3: Structural Analysis on Pulsed Lithium Iron Phosphates

The experimental results obtained from the NCA cells just presented has demonstrated that there are substantial differences in the capacity fade and impedance evolution of

lithium-ion cells when they are cycled at high pulsed rates. These differences may stem from the unique fatigue-like qualities that exist in pulsed discharge profiles. The impedance modeling presented in the previous chapter points to a decrease in the ion transfer rate in the double layer as pulsed discharge cycles occur. However, none of the tests conducted on the NCA cells in the previous study touch on the physical changes that occur within the electrode material or on the surface. Characterizing these changes may explain the reason for the impedance rise and the more exponential capacity fade behavior. Ultimately, the objective of this research is to identify specific chemical or structural changes that explain these differences. Therefore, the next set of studies are focused on the material characterization of cycled electrode materials. These studies were conducted on the cells of the LFP chemistry since it possesses characteristics which are favorable for high power systems.

Full characterization of cells in the Navy pulsed load

The previous study performed using NCA cells did not simulate the sinking role of the battery from the ship's generator. In the proposed onboard applications, the batteries must sink current at the generator's maximum rate intermittently in addition to sourcing power to the pulsed load. A bipolar pulsed discharge profile is used here to simulate this behavior. The cells evaluated here are discharged for five seconds at high rate and then recharged at the same high rate for one second. That five second / one second profile is repeated until the cells is discharged. Once discharged, the cell under test is recharged continuously at an elevated rate. Introducing the added aspect of elevated recharge introduces new factors that will contribute to the degradation rate. It is the goal of this

research to isolate the effects that stem from, or are enhanced by, the introduction of the bipolar pulsed charge/discharge operation.

In order to study changes in electrode structure and chemistry, it is necessary to employ x-ray spectroscopy techniques including x-ray diffraction and x-ray absorption spectroscopy. Degradation mechanisms such as new phase formations, structural breakdown, and atomic reordering can be identified using these techniques. The aim is to tie these structural changes to the observed impedance rise and capacity fade in the pulsed cells. This study performed here was conducted on four 2.6 Ahr, cylindrical, commercial off-the-shelf LFP cells. Three of these cells were cycled using a high rate pulsed profile while the fourth was cycled using a high rate continuous profile. All of the cells used are of the 26650 form factor and the manufacturer's data sheet properties are presented in

Table 1.

The cathode is an olivine structured LFP which is mixed with polyvinylidene fluoride (PVDF) and carbon black as binder material and conducting material respectively.

Table 1: List of specifications for the 2.6 Ahr, 26650 lithium iron phosphate test cell used in this study

26650 Lithium Iron Phosphate Test Cell	
Capacity	2.6 Ahrs
Nominal Voltage	3.2 V
Charge Cutoff Voltage (recommended)	3.65 V
Charge Cutoff Voltage (maximum)	4.1 V
Discharge Cutoff Voltage (recommended)	2.5 V
Discharge Cutoff Voltage (minimum)	2.0 V
Recharge Current (recommended)	2.6 A
Recharge Current (maximum)	5.0 A
Continuous Discharge Current (maximum)	42 A
Pulsed Discharge Current (recommended for 30 s)	26 A
Pulsed Discharge Current (maximum for 30 s)	50 A

The anode electrodes are graphitic carbon bound together with a mixture of carboxymethyl cellulose and styrene-butadiene rubber. In this study, scanning electron microscopy will be used to visually inspect the electrode material integrity before and after cycling. Additionally, using the x-ray spectroscopy techniques listed above the integrity of the crystal structure of both electrodes and the arrangement of cathode atoms in the lattice will be studied. X-ray absorption will also be utilized to evaluate the iron oxidation state in the cathode material. This information can help identify the

amount of lost active material in the cathode particles as well as quantify the concentration of delithiated iron oxide phases.

Prior to any high rate evaluation, each of the LFP cells studied is cycled five times the nominal 1C rate (2.6 A) using a constant current (CC) discharge and a constant current - constant voltage (CC-CV) recharge procedure between 2.5 V and 3.65 V, respectively. This is done to check proper functionality of each cell and to grow the initial layers of SEI at a low rate. Next, a 'baseline' procedure is performed in which the cell was cycled once at the 1C rate using the same CC discharge and CC-CV recharge procedure used in the initial five cycles and each cell's impedance is measured using EIS. The EIS spectrums are collected at 100% state of charge (SOC) using a sinusoidal signal with an amplitude of 10 mV across a frequency range of 0.01 Hz to 10 kHz recording thirty frequencies per decade. This baseline procedure is repeated after every set of twenty high rate cycles in order to characterize capacity fade and impedance growth over the cell's cycle life without the need to dismantle them. Once the initial baseline is completed, three of the cells are cycled using a high rate pulsed procedure while a fourth is studied using a high rate continuous procedure. This allows for a similar comparison between pulse and continuous degradation behavior as was made in the study conducted on the NCA cells. The pulsed procedure used to cycle the LFP cells is explained in step-by-step form in Table 2. A Maccor 4000 series industrial cycler equipped with five channels capable of supplying and loading 5 V and 245 A each is used to cycle all cells. The fourth cell in the experiment will undergo continuous discharge cycling with a similar procedure to the pulsed cells except for step three. In this cell, step three is replaced by a CC discharge at 15C similar to the recharge in step

four. A 75°C temperature cutoff is programmed into both pulsed and continuous discharge procedures to limit the thermal stress. The external temperature is monitored by three T-type thermocouples that are sandwiched between two thin layers of polyimide tape and attached to the face of each cell with equal spacing. The polyimide tape provides electrical insulation for the thermocouples from the cell body. The cells are cycled using the respective high rate procedure until the capacity put back in during the 15C CC recharge was 50% of its original value or until 100 cycles was reached, whichever came first. Afterwards, a final baseline procedure was performed prior to electrode material characterization.

Table 2: Cycling procedure, limits, and conditions for the pulsed discharged cells. Continuously discharged cells have a similar procedure, replacing step three with a CC 15C, 40 A discharge

Step #	Step Name	Description	End Condition
1	Baseline	1C (2.6 A) cycle of CC-CV Charge to 3.65V, CC Discharge to 2.0V	5 Cycles
2	EIS	90 minute rest, impedance spectroscopy (10mHz-10kHz, 10mV amplitude)	End of Analysis
3	Pulsed Discharge	5s CC Discharge, 1s CC Charge @ 15C (40 A)	Cell voltage $\leq$ 2.0V
4	Recharge	CC Recharge @ 15C (40 A)	Cell voltage $\leq$ 4.1V
5	Repeat	20 cycles of Steps 3 and 4. Rest between each cycle allows cell to cool to room temperature	20 Cycles Completed

It should be noted that the voltage limits in all cells are extended to 2.0 V in discharge and 4.1 V in recharge, respectively. This was designated by the Navy as a way to extend the operating time in order to increase the number of pulses in each discharge.

This extended voltage range is the maximum allowed for these cells based on the manufacturer's specifications. This was not predicted to be a large factor in degradation over the other aspects of the cycling profile because of the high cycling rates. At 40 A, the cells are not completely charged or discharged during cycling since they are not allowed to settle and "top off". While it has been shown in previous studies that higher cycling rates in LFP cells will activate more surface cathode particles, there is an insufficient amount of time for the slow diffusional processes to complete [56]. Also, the cell experiences a larger voltage drop when subjected to the 40 A load compared to a nominal rate discharge. As the internal cell impedance rises, this voltage drop will increase and more energy will be lost to heat production. Increasing the voltage range prolongs the cycle life of the cell in high rate applications by not allowing the voltage drop to exceed the cutoff limits before extracting any energy.

When examining this profile, thermal degradation is a concern when drying to narrow the focus to only degradation mechanisms caused by the pulsed profile. High temperature operation can increase the movement of ions in the cell giving a higher usable capacity, but the degradation rate will also be increased. As stated, the cycler monitors the external cell temperature and limits it to 75°C buy placing it in a rest until it reaches 40°C if the limit is reached. Even this limit is above the manufacturer's maximum rating which is listed at 60°C. However, this is the requested operating procedure that the Navy wishes to explore. In order to address this, the continuous cell which was cycled alongside the pulsed cells has the same temperature cutoff. Since the extra discharge time in the pulsed cell is minimal in comparison to the continuous

discharge, the residual thermal effects from it should be minimal as there are also rest periods between the discharge and charge steps to allow the cell to cool.

Another major concern with this profile is the abnormally high recharge current imposed. LFP cells like the ones used in this research, normally have a maximum charge rate of 5 A [11]. The LFP crystal structure doesn't allow for good electrical conduction between particles. This is due to the alternating arrangement of FeO_6 octahedrons and PO_4 tetrahedrons. When the lithium ions leave the matrix, the FeO_6 is octahedrons are still separated by the PO_4 tetrahedrons since they share common sites. Therefore, there is not one phase which is allowed to form a continuous chain. While this arrangement does in fact provide stability making it one of the safest lithium ion chemistries, it also decreases the electrical conductivity. High rate charging of this chemistries could lead to permanent phase shifts in the cathode material and breakdown of the binder materials. Like the thermal degradation concern, this was addressed by employing the same recharge rate to the continuous cell which was cycled simultaneously alongside the three pulsed discharged cells. Again, while there are one second 40 A pulses in the discharge profile, the assumption is that the full continuous 40 A recharge after the discharge step is more critical to the degradation rate of the cell. Therefore, any differences in the material degradation analysis between pulsed and continuously discharged cell is assumed to be entirely from the addition of the pulsed discharge profile.

In addition to the 1C capacity and EIS measurements, differential capacitance measurements are used to map the charge storage reaction across the voltage range used. This measurement is calculated for several of the 15C - CC recharge steps.

Differential capacity analysis can illustrate the charge storage process by mapping the derivative charge stored with respect to voltage change. Since the analysis involves looking at very small fluctuations in voltage it is normally performed on a low rate CC step, typically C/25. To perform this analysis on 15C recharges, each set of voltage data needed to be filtered to smooth the voltage profile from each of the chosen cycles. Therefore, voltage data was placed through an 13^{th} order Savitzky-Golav filter using National Instrument's DIAdem software before the differential capacity data is calculated. Because the voltage range was extended to prolong cell cyclability, the differential capacitance analysis will provide valuable information about the rate of successful charge storage within that range. It can also point to the root cause of capacity fade at high rates by showing whether the degree of charge storage decreases or if the internal resistance rise pushes the charge storage outside of the voltage range.

Analyzing the electrical degradation

Originally, the intent was to compare all four cells after one hundred cycles of operation under high rate continuous or pulsed discharge. However, the three cells which cycled under pulsed loading ceased to accept charge at the 40 A rate after less than 50 cycles. Since no charge was successfully stored the eventual 15C (40 A) charge capacity of the cell was 0 Ahrs at the end of the experiment. The three pulsed cells in the experiment are designated as PD01, PD02, and PD03 while the continuous cell is referred to as CONT. A linear fade in the capacity of the 15C CC recharge portion of the procedure was measured from all three cells, PD01, PD02, and PD03, respectively, for at least twenty cycles before a rapid fade was observed. This is opposed to the CONT cell that showed linear fade in the 15C recharge capacity through one hundred cycles. Though

the linear fade in the CONT cell was measured through one-hundred cycles, only the data collected from the first sixty cycles is shown so that comparison to the three PD cells is clearer. After approximately twenty cycles of linear fade, each of the three respective PD cells rapidly lost the ability to accept recharge current at the 15C rate. The recharge capacity rapidly decreased to 0 Ah within the next seventeen to twenty-five cycles, depending on the cell as seen in Figure 23.

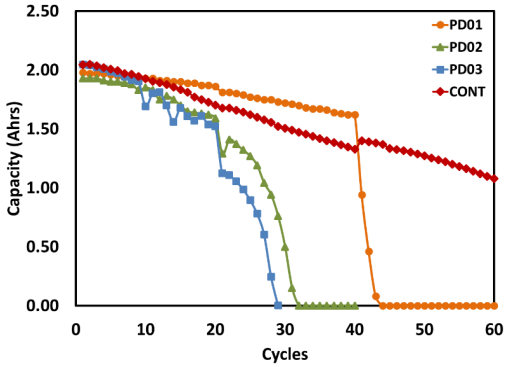

Figure 23: Capacity fade for PD and CONT cells formed using the measured capacities from the continuous 15C (40A) recharge step in each cycle

Despite each of the three PD cells being unable to accept 15C recharge, each one was still able to accept and store charge at the 1C rate. The 1C baselines performed between every twenty cycles revealed that only roughly 6% capacity fade was measured when compared with the initial 1C baseline measurement. In contrast, roughly 14% capacity fade was measured from the CONT cell as shown in Figure 24.

The data collected in this experiment suggests there is a critical time at which the charge transfer reaction slowed to the point where the recharge reaction can no longer be completed at the 15C charge rate. This hypothesis came from the notion that if there

was a rapid loss of active material due to the cycling conditions in the pulsed cells, then the fade rate would simply increase instead of the behavior observed.

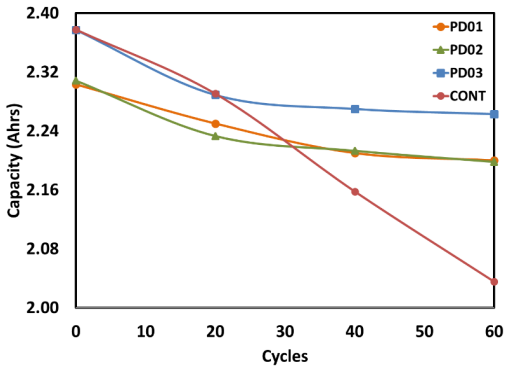

Figure 24: Capacity fade for PD and CONT cells formed using the measured capacities from the 1C (2.6 A) baselines taken after each set of 20 high rate cycles

While capacity fade is normally explained by a loss of active Li-ions to side reactions, it is unclear from this data alone whether or not that was the main mechanism behind the sudden decrease in the PD cells' recharge capacity at 15C. Another possible cause for the sudden inability to accept high-rate recharge is impedance growth which pushes the cell's over-potential above the voltage limitations imposed on the cycler. In short, eventually the over-potential required for the majority of the charge transfer and storage reaction to complete rises above the 4.1 V maximum. The differential capacitance analysis will paint a clearer picture of the evolving charge storage reaction over the life of the cell to better explain the source of this fade.

Using differential capacitance to track degrading charge phases

Differential capacity analysis can be used to determine if the magnitude of charge transfer across the voltage range follows the same trend as the capacity fade data collected in this experiment. Differential capacitance analysis is a technique that is

currently being embraced by many scientists in the electrochemical filed to identify the cycling characteristics in experimental cells. This is possible because differential capacitance can identify phases in the charge and discharge pattern which can be linked to the chemical behavior of the cell chemistry [57]. This can be utilized to show how each phase in the three pulsed LFP cells contributes differently as the cells degrade. In Figure 25A, the 15C recharge differential capacity curves from cell PD 01 of cycles 1, 20, and 40, respectively, are shown. It was decided in this experiment that only one cell would be analyzed using differential capacitance as all three pulsed cells experienced very similar fade behavior. In the analysis of PD 01, a gradual rise in charge transfer resistance is seen before the drop in charge acceptance that begins during cycle 41. Early in the life of the cell, the majority of charge storage occurred when the cell's voltage was between 3.65 V and 4.1 V. Comparison of the differential charge profiles from cycles 1, 20, and 40, respectively, show that there is a gradual increase in the charge storage activation voltage which is the voltage at which successful charge storage begins. Over the first forty cycles of cell PD01, the differential charge profiles were nearly identical with respect to their curvatures; however, the curves are compressed within a smaller voltage range as more 15C PD cycles are completed. The area under each of the curves, which represents the total charge stored in the cell during a cycle, reduced at a steady rate. This mirrors the trend seen in the capacity fade profile for the first forty cycles of cell PD01. It can also be seen in Figure 25A that in the first 40 cycles, there are several phases which the cell transitions between when it is charging. For example, there is a small plateau region between 3.7 V and 3.8 V in the first cycle which represents a steady rate of charge storage in that

voltage range. There are two more of these plateau regions occurring between 3.8V and 3.9V in the first cycle. In the first forty cycles in cell PD 01, the voltage range in which all these phase regions reside are reduced while the magnitude of the differential charge storage increases linearly.

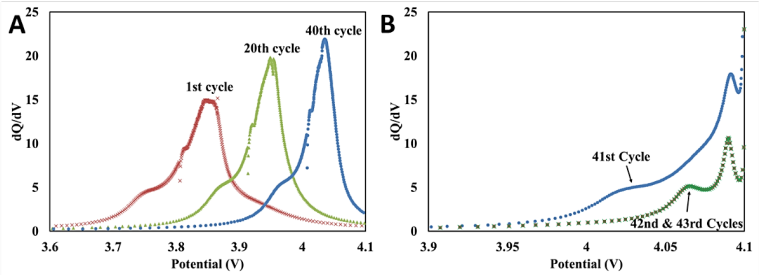

Figure 25: Differential capacitance spectrums derived from the CC 15C recharges of cell PD01 at A) cycles 1, 20, and 40. Separate spectrums were derived from the same step at cycles B) 41, 42, and 43 during the rapid capacity decline

On the other hand, the differential profiles of cycles 41 to 43, which are shown in Figure 25B, show that there is a dramatic reduction in the amount charge stored within the operating voltage range of 2.5 V to 4.1 V. From cycle 41 to 43, the charge storage time is shortened such that it occurs within a range of less than 100 mV. Also the individual phase regions seen in the analysis of the first 40 cycles are reduced in range to the point where they span no more than 50 mV. The final phase with the highest peak magnitude of differential charge storage no longer occurs within the applied voltage range. In fact, it can clearly be seen that the entire differential capacitance profile is pushed to the right along the voltage axis. This indicates that there is an abrupt increase in the cell's internal resistance. This is most clearly seen when comparing the differential curves from Figure 25A to those in Figure 25B. Between cycles 40 and 41, the activation voltage shifted to the point where the majority of the profile falls outside of the 3.65 V to 4.1 V range. However, the magnitude and curvature of the differential

curves are still similar to those of cycles 1, 20, and 40, respectively. It can be inferred that if the voltage were not limited to 4.1 V, the charge storage may still be successful at the 15C rate. Overall, the differential capacitance analyses and capacity fade measurements show that there was an abrupt slowing of the kinetics of the charge storage reaction due to a rapid rise in internal cell resistance. This rise prevented all three respective PD cells from accepting charge at the 15C rate within the 2.0 V to 4.1 V range in which they were cycled.

Discovery of mid-frequency separation in EIS spectrums

Once it was clear that a rise in the internal resistance had occurred, it was necessary to understand what had caused it to grow rapidly. Analysis of the electrochemical impedance spectroscopy (EIS) results at each twenty cycle interval was performed to characterize the evolution of cell impedance. The EIS measurements made from all three respective PD cells are shown in Figure 26, Figure 27, and Figure 28. In the data, there is a clear separation of the mid-frequency semi-circle, located in the 8 mΩ to 17 mΩ range, from one distinct semi-circle into two. The first semi-circle remains within the same real impedance range as the original spectrum did, while the second appears in the 17 mΩ to 28 mΩ range with roughly the same magnitude of imaginary impedance. Many researchers have attributed these mid-frequency semicircles to be a combination of three impedance elements including the charge transfer impedance, impedance of the SEI layer, and the bulk electrode impedances [58]. Since the bulk electrode impedance does not normally evolve much over cycle life, it was determined that most likely the separation was caused by a rapid growth of the SEI layer impedance and/or from rise in the charge transfer impedance in the cell. The charge transfer impedance

represents the ease of which ions can be exchanged through the double layer at each electrode interface. The efficiency of the charge transfer process is influenced by several factors, the most important being the contact area with the electrolyte at each electrode. If the contact area were reduced and the rate of ion transfer through the double layer declined, it would correspond to a decrease in that cell's ability to transfer Li-ions from the electrolyte to the electrode.

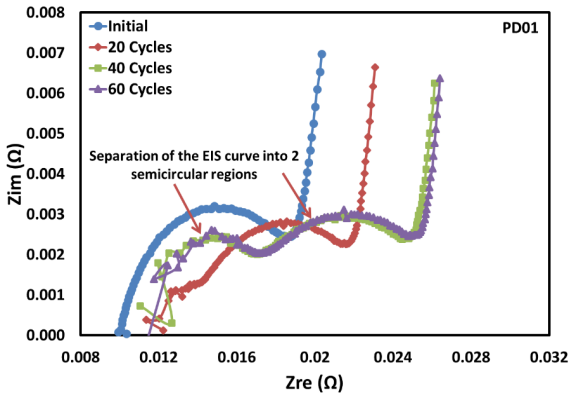

Figure 26: EIS spectrums of cell PD 01 taken at 20 cycle intervals after the 1C baseline

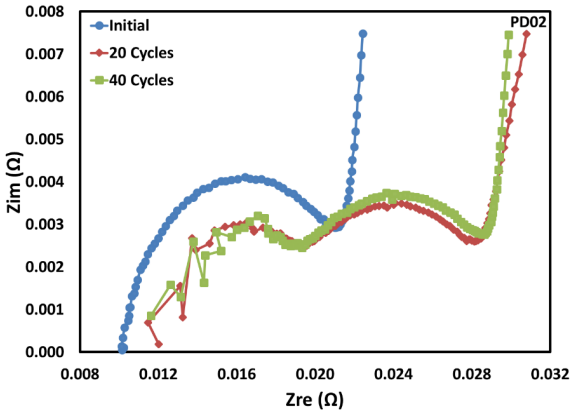

Figure 27: EIS spectrums of cell PD 02 taken at 20 cycle intervals after the 1C baseline

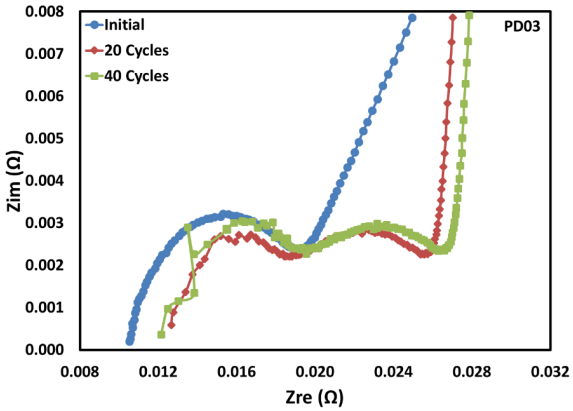

Figure 28: EIS spectrums of cell PD 03 taken at 20 cycle intervals after the 1C baseline

As mentioned, it's also equally possible that the separation in the PD cells was the result of an SEI film which most likely forms at the graphite anode-electrolyte interface. Normally, as the electrolyte solution reacts with active Li-ions to form the SEI layer, other byproducts, such as polyethylene oxide (PEO), form between the SEI and the

graphite anode through electrolyte co-intercalation, which increases the interfacial contact area between the SEI and graphite as the film grows.

This can result in a sharp decrease in charge transfer resistance and a slight increase in the double layer's capacitance [55]. Therefore, the formation of an SEI can actually provide stability and in some cases protect the anode material underneath from further side reactions with the electrolyte. However, if there is a persistent growth of an ionically resistant film, then the SEI formed would act as more of a barrier to Li-ion transfer instead of providing stability, causing this behavior [59]. This may be the reason that these cells performed poorly under high rate pulsed discharge. While these 2-electrode results couldn't validate these theories alone, it showed that one of these three impedance elements discussed evolves during PD cycling to affect the low frequency response of the cells. Low frequency response is correlated to diffusional phenomenon such as the movement of active Li-ions through mediums such as the SEI. As stated, particular chemical compounds which comprise the SEI can adversely affect the rate of diffusion of Li-ions into the anode. The SEI forms mainly by consuming active material during cycling, which corresponds to a drop in usable capacity. Therefore, it is important to subsidize the electrical characterization with chemical characterization of the electrodes and their surface films in order to get a full picture of the affects caused by cycling these cells under the pulsed loading. Comparing the results to those from the continuously discharged cell will outline the major differences between the degradation behavior of the two.

In comparison, when studying the CONT cell impedance spectrum, shown in Figure 29, the plot shifts along the real axis while having little increase in the imaginary scale.

Notice however, that there is no separation of the mid frequency semi-circles into two as was seen in the PD cells. The magnitude of the shift decreases in between each of the twenty cycle intervals. Physically, this is attributed to the gradual development of the SEI layer which, as mentioned, can stabilize and protect the electrode surface from further side reactions with the electrolyte. This gradual increase in the cell's real impedance is typical of the type of evolution found in literature of studies done on impedance evolution of LIBs [58].

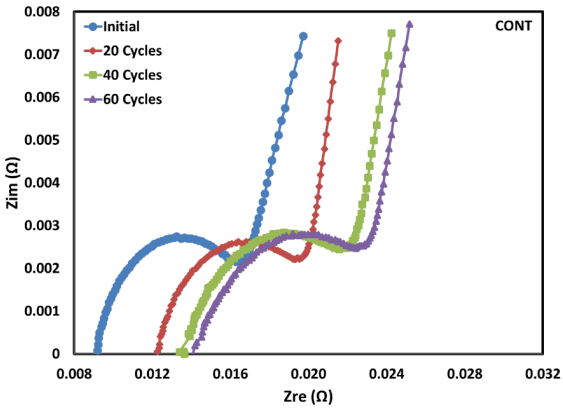

Figure 29: EIS spectrums of the CONT cell taken at 20 cycle intervals after the 1C baseline

This means that in the CONT cell, the SEI layer was not able to affect the low frequency, diffusional properties of the cell in a way that drastically influenced its impedance profile which is suspected in all the PD cells. Most importantly, the drastic difference in the effect of the low frequency region shows the CONT cell degraded in an entirely different manner compared to the PD cells. Also, the CONT cell impedance spectrum provides a reference for the type of evolution typically seen in this cell when operating at 15C rates. When discussing the causes behind the difference in impedance evolution, it is reasonable to suggest that the separation seen in the PD cells is not only

a result of the high cycling rate, increased cutoff voltages imposed, or high thermal stress. Thus, the major difference between the PD cells and the CONT cell which could explain this difference in impedance evolution is the profile under which each cell was cycled.

Chemical degradation characterization

In the introduction, it is mentioned that when lithium is extracted from the cathode matrix there is a small reduction in its volume. There is also a change in its structure as the atoms rearrange themselves to form new phases. In the LFP chemistry, the Fe^{2+} which exists when lithium is bonded to the cathode structure, changes to a +3 oxidation state when charging the cell. Accompanying this change is the reordering of atoms in the new $FePO_4$ lattice which slightly shifts the available sites which active lithium can occupy. While the olivine structure of LFP cathodes naturally provides stability making the location of these sites consistent, extreme cycling conditions can cause lithium to diffuse from deeper veins in the cathode particles which never fully reverse and return to their original sites due to the high rates at which the cell is cycled at. Moreover, the hypothesis of this research is that the fast switching speeds of pulsed loads exasperate this by not allowing time for them to diffuse back to their original sites before the flow is reversed or the load is shut off. As stated this may either promote side reactions or promote the existence of phase separation among the cathode particles. In the case of the three pulsed cells the investigation of the atomic order and phase purity of the cathode particles is critical towards the investigation of the hypothesis.

Several methods can be utilized to study these phenomena. X-ray spectroscopy techniques such as x-ray diffraction and x-ray absorption spectroscopy have both been

used by researchers to study degradation phenomenon [60, 61, 62]. Scanning electron microscopy can also be used to get surface images of electrode foils after being extracted from cycled cells. These characterizations are normally conducted on smaller coin cells created in a laboratory environment which makes the electrode material easier to extract after testing. In this research, an extraction procedure was developed to safely remove electrode materials from full sized 26650 cylindrical cells. Because of the reactivity of lithium-ion battery materials and chemicals with ambient air and moisture, all of the disassembly procedures are conducted within an Argon filled glove box that has an environment with less than 3 ppm water and oxygen. It should be noted that all extraction procedures are also conducted at 0% SOC for safety reasons. The procedure, outlined in Appendix A, begins with the peeling back of the crimped metal seal around the top cap of the cell by cutting small slits in the metal which can then be peeled back carefully using needle nose pliers. Afterwards, the current collectors which are welded to the top cap to make the positive connection are severed and pressed down gently towards the jelly roll to help prevent any accidental shorting. Secondly, there are small perforation-like cuts made in the side casing of the cell which are continuations of the lines where the slits were cut in the top cap seal. These perforations allow for the casing to be removed from around the jelly roll by peeling back sections of it until it can be pried apart. In this study involving the three pulsed discharged cells which rapidly faded in capacity, the jelly roll is unrolled and sections are removed from the outer, middle, and inner sections using a pair of ceramic scissors. The outer section of the roll is designated as the part of the roll which is closest to the casing of the cell while the inner section is designated to be the part closest to the core.

Any electrode samples are washed in a dimethyl carbonate (DMC) bath for ten minutes and then left to dry for another ten minutes in the glove box before they are analyzed. This extraction method is critical in the analysis of electrode materials using the methods mentioned above. The results obtained from each of the subsequent characterizations are presented and discussed below.

Micrographs of the post-cycled graphitic anodes

An elementary approach for visually inspecting anode material for the presence of a thick SEI layer is to use SEM to examine the surface of electrode particles for signs of micro-cracking, heavy surface film growth, and other structural deformities. For this study, SEM micrographs are taken using a Hitachi S-5000H Microscope utilizing a cold field emission source at 10 kV and 12 mA. It has a resolution of 0.6 nm at 30 kV and 3.5 nm at 1 kV and a working distance of 5-7 mm. Figure 30 shows images of a fresh graphite anode sample extracted from a non-cycled cell for reference. In comparison, Figure 31 shows the SEM micrographs of the anodic graphite particles from cell PD 01 which indicate that the surface film formation is heavy yet is not at a stage where it has formed a passivation layer over the entire surface. More interestingly, the degree of formation is not consistent between different sections of the roll. The formation is seen on the micrographs taken at the inner part of the roll while the outer section seems relatively unaffected.

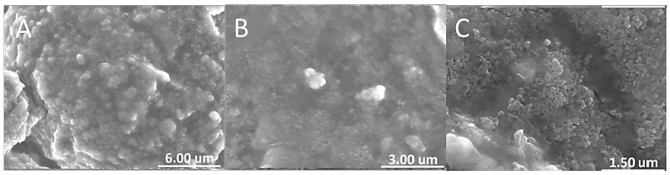

Figure 30: SEM micrographs taken from fresh graphite anodes extracted from a non-cycled cell at three separate magnifications increasing from A-C

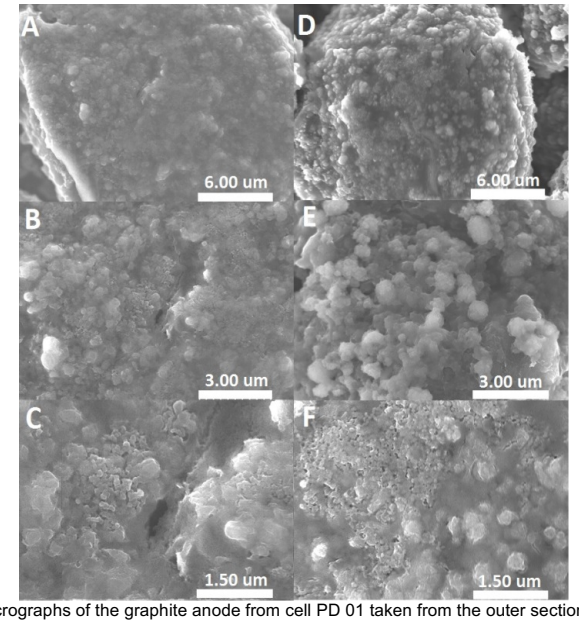

Figure 31: SEM micrographs of the graphite anode from cell PD 01 taken from the outer section (A-C) and the inner section of the jelly roll (D-F)

While the formation at the inner section is heavier, there are still areas on the graphite that resemble the material imaged at the outer sections. In other words, the surface of the inner electrode material contains a mixture of both SEI heavy and bare areas rather than complete passivation. This can be seen most clearly when comparing the two 10,000x magnification images in Figure 31 taken at the outer and inner sections of the jelly roll.

The outer section of the roll is relatively clean compared to the inner section that contains large spherical formations on the particle surface. It is possible that since the core of the cell is hotter than the outer edge, the thermal energy increases the favorability of side reactions in this region. Formation of an SEI layer does not always

indicate eventual failure of a lithium-ion battery. In most cases, the SEI formation stabilizes and actually protects the anode from further deposition. The result is a small increase in ohmic resistance as seen in the EIS spectrums. However, as the SEI layer grows into a passivation layer over many cycles, it consumes active material which results in permanent phase changes in the LFP material and capacity fade in the cell. In the tested LFP cells this does not appear to be occurring in the outer section of the roll, further proving that the rapid drop in high rate charge acceptance is caused by more than a critical buildup of the SEI layer or a breakdown in the structure of the anode material.

Crystallographic analysis of cycled electrode materials

X-ray diffraction spectroscopy (XRD) can also yield valuable information which can explain the cause for rapid capacity fade. The structural deformations and permanent phase changes mentioned can be identified using XRD by monitoring the graphite and LFP peak positions and also examining the spectrum for new phases. When charging an LFP cell, the metal oxide cathode transitions from an $LiFePO_4$ phase to $Li_{1-x}PO_4$. In fully delithiated regions of the cathode, the metal oxide further oxidizes to become $FePO_4$. Therefore, there is a transition in the Fe from a Fe^{2+} state to a Fe^{3+} state [56]. If there is loss of active material, a different set of diffraction peaks may begin to arise in the XRD spectrum representing the oxidized cathodic phases. Additionally, an X-ray diffractometer used in a Θ-2Θ Bragg configuration relates a change in the equilibrium peak position on the spectrum to an increase or decrease in the interplanar spacing, d, of the diffracted planes through Bragg's Law.

$$n\lambda = 2d \sin\theta \quad (8)$$

This is due to the fact that each crystallographic plane of atoms in the olivine structure has a designated diffraction peak position. That peak represents that plane and all others in the same family. Essentially, all the crystallographic planes that belong to a single peak in the XRD spectrum have an equal spacing between them, d. When this spacing is altered by either a phase change or physical stress, the diffracted x-ray signal will be detected at a different angle. These transitions are the effects that are studied when conducting XRD scans on extracted LFP materials in cell PD 01 of the pulsed study. A Bruker D500 X-Ray Diffractometer utilizing Cu Kα1 monochromatic x-rays in a Bragg configuration at 40 kV and 30 mA is used to collect the crystallographic spectrum for this cell. From the evidence gathered in SEM micrographs, it is imperative that the electrode material be analyzed to identify phase separations and large order crystal defects. In cell PD 01, broad spectrum scans of the cathode material from 20°-70° shown in Figure 32, indicate minimum permanent phase separation when compared to spectrums taken from fresh cells. The majority of the peaks appear at their original positions for $LiFePO_4$ with only a few small unidentified signals. Thus there is still an abundance of active material remaining which can contribute to charge transfer thus supporting the conclusions drawn from the micrographs. XRD scans suggest that there is no large order permanent phase transformation in the LFP cathode of cell PD 01. There is also no appreciable shift in the spectrum from its theoretical position or any expansion of individual peak widths. This is demonstrated more clearly when comparing the XRD spectrum of cell PD 01 to that of the CONT cell in Figure 32.

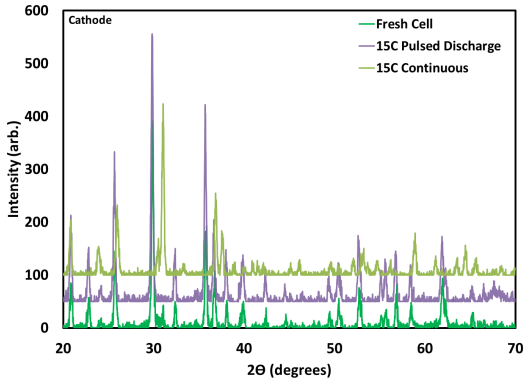

Figure 32: LFP cathode XRD patterns collected from a fresh electrode, PD 01, and CONT

It is clear that in the CONT cell, the spectrum shows phase shifts with LFP peaks such as the one originally located at approximately 2Θ=29.87° shifting to a final position of 31.04° after 100 cycles of continuous cycling at 40 A. While minute, this still corresponds to a decrease in the interplanar spacing of atoms in those planes. Thus it is reasonable to infer that the reduction in spacing between atoms occurs as part of a natural shrinking of the cathode olivine structure when it is delithiated. Some diffraction signals, such as the one which registered at 62.20° in both the control sample and the one from PD 01, completely disappear in the post-cycle CONT cathode spectrum. This is a significant difference in the final state of the cathode crystal integrity between pulsed and continuous cathodes. However, shifts in the cathode spectrum can be difficult to analyze accurately due to the lack of uniformity in the peaks between scans.

On the other hand, hexagonal graphite has a very distinct high intensity peak located at approximately 2Θ=26.38°. This peak is ideal for identifying small shifts which can be attributed to an evolution of internal stress in the lattice [63]. Broad spectrum and

focused range XRD scans of the graphite anode in cells PD 01, CONT, and a fresh LFP cell are seen in Figure 33. The other two peaks in the spectrum correspond to the copper current collector which the graphite is deposited on. The graphite peak shifts from its theoretical position of 26.38° to 26.448° on average as a result of the stage mounting process for scanning which involves pressing the electrode material onto a flat piece of stainless steel which is laid into a silicon putty on the sample stage. The peak position of the cycled graphite from cell PD 01 is located at 26.88° making the differential $d\Theta = 0.22°$ in reference to the fresh cell spectrum. This relates to a decrease in interplanar spacing between the $(002)_{hex}$ planes from 3.365 Å to 3.313 Å. Since this change is negligibly small, it is unlikely that it indicates large order defects which would be responsible for such intense cell degradation as seen with cell PD 01 or any of the other two pulsed discharged cells in this experiment. Instead, it reveals that the overall bulk order of the graphite matrix is widely intact after cycling. This corresponds well to SEM micrographs presented previously which showed no signs of micro-cracking on the surface of the anodic graphite. It is reasonable to conclude that if degradation byproducts, such as degraded electrolyte compounds, penetrated deeper into the graphite, a larger shift in the XRD spectrum would be observed. Because the opposite is seen in both the cathode and anode XRD spectrums, it is more likely that the surface condition of either electrode is drastically changing during the rapid capacity fade of these cells.

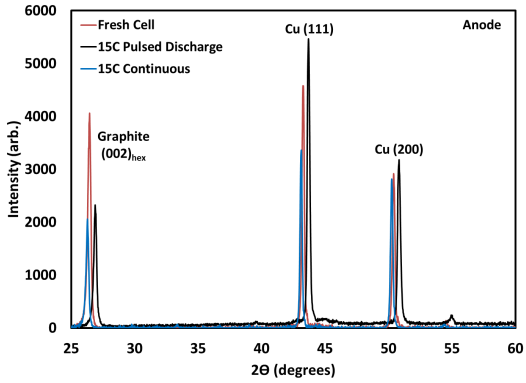

Figure 33: Graphite anode XRD patterns collected from a fresh cell, PD 01, and CONT

Evaluating the iron oxidation state and atomic order in LFP electrodes

At this point it is clear that there is a difference in the degradation behavior between cells cycled at high rates with a continuous discharge profile and those cycled using pulsed discharge profiles at the same rates. This difference clearly cannot be explained by a simple expedited loss of active material or physical damage to a cell's electrode material. Therefore, based on the evidence collected so far, it was reasonable to conclude that the difference between continuous and pulsed cells had to be chemical in nature. The hypothesis at this point narrowed to the idea that the fast switching of a pulsed profile creates more favorable conditions for particular side reactions to occur which produces a compound detrimental to the charge or discharge reactions or that it causes a breakdown in the electrode structure where the inactive materials become unstable. It was clear that an analysis needed to be conducted that would allow the identification of side reactions post-mortem. Therefore, additional samples extracted from cells PD01, PD02, and PD03 along with three other cells which were cycled in a similar manner were taken to Brookhaven National Laboratory in Long Island, New York

in order to conduct x-ray absorption spectroscopy using a synchrotron radiation beamline. The three additional cells were cycled after PD 01, PD 02, PD 03, and the CONT cell using slightly different parameters which are described in Table 3. These cells didn't show the rapid fade that was seen in the previous three PD cells. The most noteworthy change is the lowering of the external temperature limit to 60°C. It is interesting that the cells did not exhibit the same behavior as the previous pulsed cells since the temperature was thought to have a negligible impact as previously described. In fact, one of the cells cycled alongside the two 60°C cells has the exact same profile as that of PD 01, PD 02, and PD 03 and it also exhibited linear fade up to 320 cycles when the experiment was terminated for time considerations.

These three cells will serve as an important contrast when comparing their x-ray absorption spectroscopy spectrums to those from the initial three pulsed cells since the CONT cell was excluded due to time constraints. In the interest of clarity, the first set of PD cells (PD 01, PD 02, and PD 03) which were originally cycled for this study and the second set (designated PD 04, PD 05, and PD 06) which was cycled for the purpose of proving clarity to the XAS analysis will be presented separately. The experimental procedure utilized on cells PD 04, PD05, and PD 06, respectively, is presented in Table 3.

As mentioned, a synchrotron radiation beamline at Brookhaven National Laboratory (BNL) provided the source for x-ray absorption spectroscopy of the LFP cathode samples (XANES and EXAFS). Using the Fe K-edge energy of the cycled cathodes, the amount of Li missing from the cathode host structure can be quantified. This is accomplished by comparing the edge shift in each of the first set of PD cathodes

relative to an LFP powder sample to the edge energy positions measured for FeO, FeOOH, and γ-Fe_2O_3 reference samples which each have known oxidation states. Both transmission (TR) and electron yield (EY) detection modes were used to analyze both the bulk and surface LFP particles respectively, in the extracted samples.

Table 3: Cycling Parameters for cells PD 04, PD 05, and PD 06

Cell	Cycling Description	Temperature Limit (°C)	Voltage Range (V)
PD 04	15 C (40 A), 5s/1s PD w/ a 40 A continuous recharge, 320 cycles	75	4.1-2.0
PD 05	15 C (40 A), 5s/1s PD w/ a 40 A continuous recharge, 60 cycles	60	4.1-2.0
PD 06	15 C (40 A), 5s/1s PD w/ a 40 A continuous recharge, 100 cycles	60	4.1-2.0

The three sections of the jellyroll, inner, middle, and outer respectively, were analyzed and compared to an LFP foil that was made by spreading LFP powder uniformly on electrically conductive tape. The XANES and EXAFS data analysis was carried out using the IFEFFIT suite of programs named Athena and Artemis, respectively [64, 65]. After characterization of all six cells mentioned, the analysis showed little difference in the oxidation state and atomic order between PD cathodes and a reference LFP foil. Cathodes extracted from cells PD01, PD02, and PD03 showed a 0.69 eV, 0.52 eV, and 0.4 eV shift respectively in their Fe edge energies relative to the edge energy measured in the LFP foil. This is illustrated in detail in Figure 34 and Figure 35 which also reveals no variability between the sampled cathode sections with regards to the edge energy or curve profile.

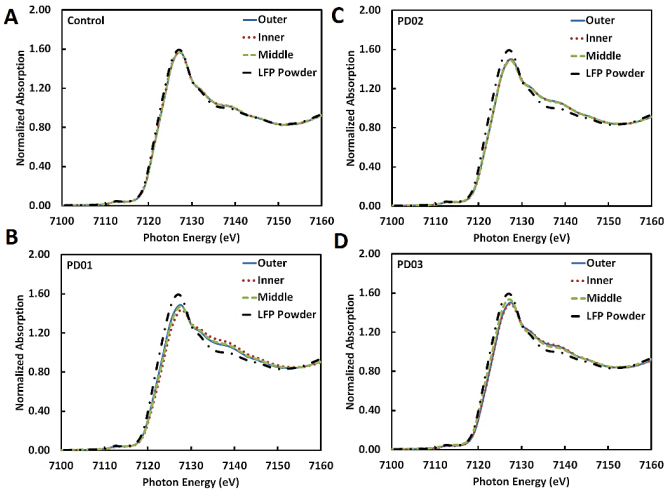

Figure 34: LFP cathode transmission XANES spectra taken in the Fe K-edge of A) a fresh cell, B) PD 01, C) PD 02, and D) PD 03.

Any delithiated LFP particles populated by Fe^{3+}, like in $FePO_4$ rich particles, would yield a positive shift in the edge energy from its lithiated Fe^{2+} position due to the increased energy required to remove an electron from its orbital [56]. However, the small shifts in edge energies of the PD cathodes suggests the abundance of particles in these three cells still exists in the Fe^{2+} oxidation state, meaning they still are bonded with Li. By this evidence and that seen in the crystallographic analysis, a loss of active Li would not explain the rapid capacity fade in PD cells even though it is known that Li-ion cells which are cycled at rates well above their nominal rate also have a greater degradation rate.

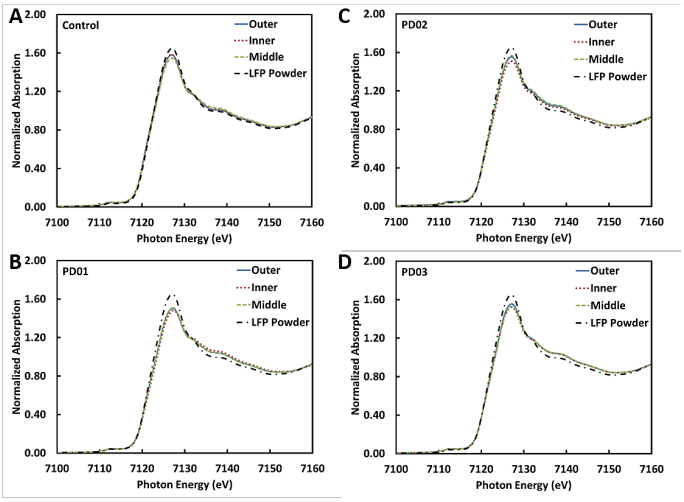

Figure 35: LFP cathode electron yield XANES spectra taken in the Fe K-edge of A) a fresh cell, B) PD 01, C) PD 02, and D) PD 03.

When utilizing surface sensitive EY detection, the magnitude of edge shifts was even smaller with a maximum of 0.12 eV indicating almost complete lithiation of particles near the electrolyte-cathode interface. These conclusions were further supported by EXAFS Fourier transforms which revealed an equally unsubstantial change in the atomic order of the PD cathodes. The EXAFS spectrums, shown in Figure 36, revealed that the atomic order in PD cathodes closely resembled the LFP foil and control. There was an increase in the signal from atoms at a spacing of 3.4 Angstroms which is the Fe-Fe interatomic distance of olivine structured LFP. This indicates that the olivine crystal structure is still intact in the majority of particles for PD cathodes. Across the EXAFS spectrum, the differences seen in PD cathodes are subtle in comparison to the LFP foil which indicate no large change in order of the atoms. Most notably, the position of the Fe-O peak at 1.5 Å doesn't shift again indicating that the degree of lithiation is

unchanged. In their study, Hong et al presented the breakdown of this peak into the separate bond distances represented.

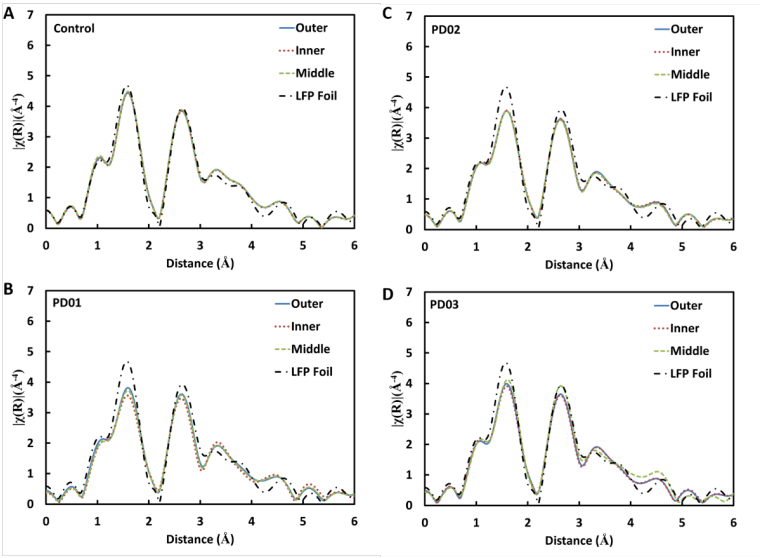

Figure 36: Transmission LFP cathode EXAFS spectra showing the atomic order in A) a fresh cell, B) PD 01, C) PD 02, D) PD 03

As the degree of lithiation decreased, the peak shifted towards a lower spacing distance indicating its transition towards pure $FePO_4$ [60]. However, no such shift was observed in the 1.5 Å peak from EXAFS spectrums of the PD cathodes. All in all, EXAFS revealed that the post-cycle atomic order of the three PD cathodes was not only identical to each other, but also nearly unchanged compared to the LFP foil respectively. This demonstrated consistency in the final chemical state between all three PD cathodes and reinforced that the rapid capacity fade didn't stem from active material loss.

To quantify the relative amount of Fe^{2+} in PD cathodes and the control, the edge shift calculated between the LFP foil and each PD cell were compared to the differences in

edge energy between reference samples of known oxidation states. Data shown in Figure 37 was calculated by comparing the PD cell edge shifts to the 4.52 eV per unit change in valence obtained by measuring the edge positions of FeO, FeOOH, and γ-Fe_2O_3. The magnitude of the edge difference between each of the reference samples illustrated a linear correlation between oxidation states of Fe^{2+}, Fe^{3+} and Fe^{4+}. By use of this method it was revealed that cathode samples from cells PD01, PD02, and PD03 had Fe^{2+} concentrations of 85 %, 88%, and 91% respectively when using edge shifts taken from TR data. With EY detection data, PD01, PD02, and PD03 were calculated to be populated by 97%, 100%, and 100% of Fe^{2+} phases. From this it clear that there exists a differential in the concentration Fe^{2+} phases between the bulk and surface LFP particles in all of the three PD cathodes. The PD profile used in this study may explain this phenomenon as it creates a localization of Li-ions at the electrolyte-anode interface due to the repetitive reversal of ion flow. Also, it's been shown that the number of active intercalating LFP particles and their homogeneity across the interface is highly dependent on the electrochemical cycling conditions, including rate [56]. In the end, the quantitative XAS data from all three PD cathodes didn't suggest there was an accelerated loss of active material on the surface or the bulk LFP particles based on the concentration of Fe^{2+} phases. It is logical to infer that if the capacity fade in these PD cells wasn't a result of active material loss, then it is instead a physical component, which impedes the intercalation of Li-ions.

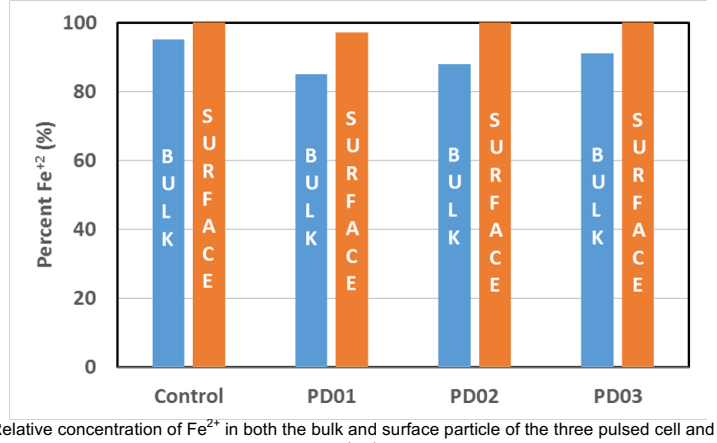

Figure 37: Relative concentration of Fe^{2+} in both the bulk and surface particle of the three pulsed cell and a fresh LFP cathode.

When comparing the XAS results from cells PD 01, PD 02, and PD 03 to those from the second set of pulsed discharged cells, a clear difference can be seen. Cells PD 05 and PD 06 are cycled with an identical profile to PD 01-03 but have a set external temperature limit of 60°C instead of 75°C. Cell PD 04 was cycled alongside cells PD 05 and PD 06 with the exact same profile as the original three in order to establish a baseline for the second set of cells. This way the lower temperature limit cells can be accurately compared to the first set. However, while cell PD 04 had the exact same profile, it didn't exhibit the same rapid fade behavior seen before. This cell survived testing and was still able to accept charge at the 40 A rate after 320 cycles where the testing was stopped. This demonstrated an inconsistency in the degradation behavior of these cells. Therefore, it is even more important to discover what conditions were necessary to cause the catastrophic event which rendered the initial three cells useless at the 40 A rate. In cells PD 05 and PD 06 there is also no abrupt capacity fade and also exhibits a similar amount of lost capacitance up to 60 cycles as cell PD 04. Therefore, it is concluded from all the evidence to this point that even though the external

temperature was higher than the manufacturer's recommended limit, there is no effect on the capacity fade behavior. Secondly, in all three of these cells a large positive shift was registered in the Fe K-edge energies (Figure 38). In both detection methods there is at least a 3.9 eV shift in the edge energy. There is also a broadening of the edge peak almost into two separate peaks.

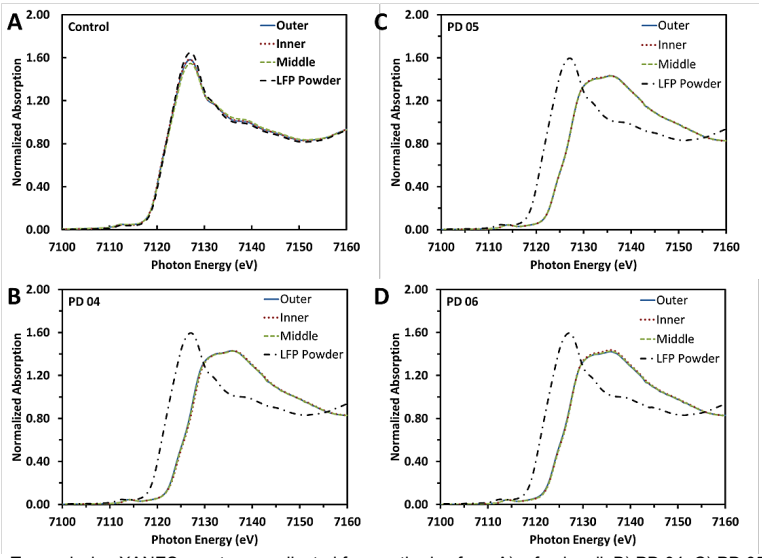

Figure 38: Transmission XANES spectrums collected from cathodes from A) a fresh cell, B) PD 04, C) PD 05, D) PD 06

This indicates that there are mixed oxidation states of Fe in the lattice of the cycled cathode samples in cells PD 04-06. In the EXAFS (Figure 39) analysis, the Fe-O peak at approximately 1.5 Å is shifted slightly left towards a lower atomic spacing further indicating that there is clearly detectable lost active material in these three cathodes. There is also a higher intensity in the signals for higher order atoms above 3.0 Å. This behavior indicates that the octahedrons of the FeO_6 groups and the tetrahedrons of the PO_4 groups are brought closer together after the cycles are conducted which is

indicative of areas which are delithiated. The broadening of the edge peak seen in XANES spectrums of this second group of cells shows the type of behavior expected when there are areas of $Li_{1-x}FePO_4$ and $FePO_4$.

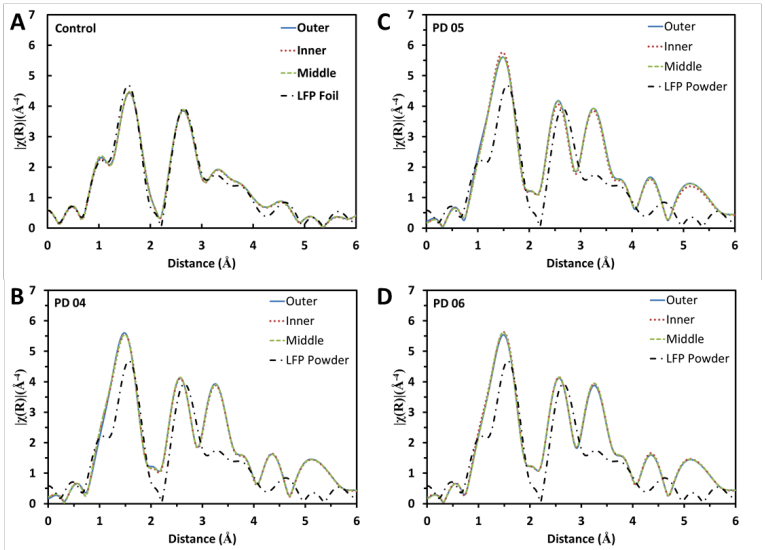

Figure 39: Transmission EXAFS spectrums of LFP cathodes from A) a fresh cell, B) PD 04, C) PD 05, D) PD 06

When putting the XANES edge shifts through the same quantitative analysis as before, it is affirmed that the amount of Fe^{2+} in the positive electrode is diminished by as much as 96.0% in Transmission mode and as much as 87.0% in electron yield detection mode (Table 4). While this percentage doesn't relate back to the actual amount of available capacity in the cell, it does signify the difference in lithium absence from the lattice between the failed pulsed cells and the ones that continued to accept charge at 40 A.

It is also interesting that the differential between the amount of Fe^{2+} on the surface and in the bulk is greater in the three initial pulsed cells which had rapid fade compared to

the last three cells. Most importantly, the results of these cells prove that the rapid capacity fade in the initial group of LFPs didn't occur as a result of a degradation phenomenon which consumes a large amount of active material such as rapid SEI growth. This analysis also proves that the initial three cells didn't suffer a large order permanent phase shift which reduces the sites for active material to occupy. Therefore, there are only a few explanations that could describe the capacity fade and impedance evolution behavior from cells PD 01, PD 02, and PD 03. Either the binder and non-active materials in the cell degrade severely causing a sharp drop in the conductivity or a physical component is preventing the lithium-ions from being successfully intercalated into either of the electrode matrices. No matter which one is responsible for the rapid capacity fade, it is unclear which aspect of the cycling profile creates the conditions favorable for it to occur. This study using XAS and XRD techniques has however provided evidence that thermal stress, permanent atomic order shift, and rapid SEI growth are not the causes for rapid fade. Due to the conclusions of this study, it was decided at this point that the pulsed profile needed to be broken down to identify which steps in the procedure are critical in causing the failure of these LFP cells to operate at high rates. The approach chosen was to examine the chemical composition of the electrode materials as a function of cycles conducted for each broken down procedure. Since the XAS data also indicated a non-homogeneous order between the surface and bulk particles, a depth analysis would also need to be performed using this same technique. The ideal characterization method for the compositional study of these cycled electrode materials is x-ray photoelectron spectroscopy.

Table 4: Results of the quantitative analysis conducted on XANES spectrums from cells PD 03-PD 06 by using FeO, FeOOH, and γ-Fe_2O_3 reference samples

Cell	TR Edge Shift (eV)	TR Fe^{2+} Phases (%)	EY Edge Shift (eV)	EY Fe^{2+} Phases (%)
PD 04: 320 cycles 45% Capacity	4.35	4	3.93	13
PD 05: 60 cycles 88% Capacity	4.25	6	3.91	13
PD 06: 100 cycles 85% Capacity	4.27	6	3.93	13

Chapter 4: Compositional profiling using XPS techniques

The structural analysis of pulsed lithium iron phosphate cylindrical cells revealed almost no change to the atomic order and crystal structure in the rapid fade, pulsed discharged cells. However, there are several mechanisms that XRD and XAS techniques cannot accurately characterize. XRD spectroscopy is hindered by the fact that it works only on crystalline materials. Therefore the only way to draw any conclusions using XRD, if a person wants to study the amorphous binder or conducting particles, is to study the effects they have on crystalline phases surrounding them like the olivine LFP or graphitic carbon in the LFP cells studied. There are times when the degradation products, such as decomposed electrolyte or dissolved metal compounds, do not appear in concentrations high enough in the electrode sample to register a meaningful signal in XRD. This becomes a problem when trying to identify degradation mechanisms such as binder decomposition and metal dissolution. XAS requires a synchrotron beamline for accurate atomic measurements making it an expensive and complex technique to utilize on a large amount of cells. It is also limited in that it cannot be utilized to determine atomic concentrations of compounds. The analysis conducted to quantify the amount of Fe^{2+} in the post cycled cathode electrode particles was done in reference to other samples which had been separately scanned. The calculated percentages were not atomic concentrations but rather ratios to the edge energy position of samples with known oxidation state. It is difficult to prove the hypothesis if there is no characterization of the precise amount of compounds which have been grown, transferred, or decomposed on or in the electrode materials.

X-ray photoelectron spectroscopy (XPS) is being used by battery scientists to study the surface chemistry of electrode materials in different electrochemical systems [66]. It has been widely used to study the effect of different electrolyte additives on the chemical composition of surface films formed on an anode surface [67]. For this research, it will be very useful to study the changing surface chemistry. XPS spectrometers in certain configurations are also capable of depth profiling using Argon sputtering. XPS can be used to obtain detailed and accurate results compared to XAS due to the standardization of the technique. This means that the signals measured from an XPS test can be identified by comparing their location to those published in reference tables. Similar to XRD peaks, previous researchers have characterized the XPS response of many pure compounds and raw materials. In a complex system or surface film, like those common on the surface of lithium-ion battery electrodes, the individual compounds which comprise the film can be broken down and identified. This is possible due to the basic principle of XPS. This spectroscopy method works similar to an x-ray diffractometer introducing an incident x-ray beam of known energy and wavelength and measuring the response. XPS is done within a vacuum and the detector measures the kinetic energy of a valence electron which is emitted. When an incident x-ray hits an atom, it may transfer enough energy to knock off valence electrons from certain orbitals as illustrated in Figure 40. The detector reads and calculates the binding energy of this released electron by using the following basic conservation of energy equation:

$$E_{binding} = E_{photon} - (E_{kinetic} + \emptyset) \quad (9)$$

Where:

$E_{binding}$ Binding Energy

E_{photon}	X-Ray Photon Energy
$E_{kinetic}$	Kinetic Energy of Electron
ϕ	Work Function

The work function, ϕ, can be described as the minimum amount of energy needed to knock a particular electron from its orbital. This is determined during calibration by scanning a reference sample and shifting the spectrum based on a signal from a compound with a well-known binding energy.

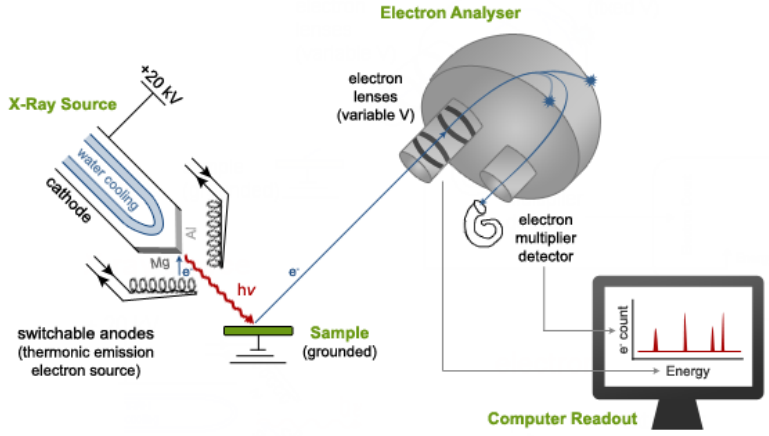

Figure 40: A diagram outlining the working principle of x-ray photoelectron spectroscopy [68]

During a scan, the spectrometer passes a range of different emission energies which excite different levels of electron orbitals. The calculated binding energy is unique to a certain orbital of a specific element and is characteristic to that orbital alone. Therefore, XPS is a valuable tool that can be used to identify surface compounds and calculate their atomic concentration on battery electrodes [69]. The work being presented in this chapter involves using XPS to compare the surface chemistry between lithium iron phosphate cells cycled under different profiles. As mentioned in the previous chapter, it is important to break down the pulsed profile into individual steps to see which one is

most critical in causing rapid fade behavior unique to pulsed cells. This is shown and discussed in the following sections.

Surface profiling of the LFP and graphite electrodes

After cells PD 01, PD 02, and PD 03 were analyzed using XAS, the remaining samples were taken to the Naval Surface Warfare Center-Carderock Division in Bethesda, Maryland for XPS analysis. While a more extensive study needed to be conducted using XPS on fresh cells, it was also advantageous to study the surface chemistry of the initial lithium iron phosphate cells in order to establish a baseline. Acquiring this data allows the subsequent tests to be directly compared to the originally discovered phenomenon prompting this line of research. XPS is used to identify compounds precipitating from side reactions and quantify their chemical compositions. By completing this characterization, it is possible to identify the side reactions themselves. The XPS work is conducted using a Physical Electronics model 5400 X-ray photoelectron spectrometer. The electrode samples are sensitive to air exposure, so it is important that the transfer process from glove box to spectrometer not involve any exposure. The samples were transferred via a sealed custom-built chamber into the intro chamber of the spectrometer. This transfer chamber wasn't purged before removal and still contained the argon gas from the glove box when attached to the intro chamber. To minimize sample-outgassing, the intro chamber is evacuated for several hours before transferring the sample into the analysis chamber. Data from each sample is collected at room temperature using a non-monochromatic Al Kα (1486.6 eV) X-ray source operating at 400 W (15 kV and 27 mA) for all electrode materials. The analyzed

area is set to 1.0 x 3.5 mm^2 and all spectra are collected at an electron takeoff angle of 45°.

Testing began with a full range scan of emission energies known as the survey scan. These spectra, taken from a range of 0 – 1200 eV, are collected at an analyzer pass energy of 89.45 eV, 0.5 eV/step and an integration interval of 50 ms/step. The resulting survey spectra is an average of 15 cycles with a total acquisition time of 30 min. Multiplex scans are conducted in areas of interest including the C 1s, O 1s, F 1s, Li 1s P 2p, and Fe 3s photoemission regions. These are collected at pass energy of 35.75 eV, 0.2 eV/step and an integration interval of 50 ms/step. The resulting spectra from these areas are analyzed using deconvolution software which fitted the spectra by combining set of peaks with a Shirley-type background and a combined Gaussian-Lorentzian line shape. There are several regions in these scans which cannot be utilized for compositional analysis due to their interaction with neighboring regions which also exist in the electrode samples. For example, the Fe 2p region is distorted by contributions from inelastically scattered photoelectrons of the F 1s line and, hence, the Fe 3s spectra is collected instead. No information about Li in the cathode can be obtained due to overlap between the Li 1s and the Fe 3p regions and the significantly higher cross section of the Fe 3p line relative to the Li 1s line. This overlap also prevents the use of the Fe 3p region for composition and chemical state determination of iron. This is very important in the anode side when checking for signs of metal dissolution. In addition to these exclusions, the spectra for cathode and anodes are shifted to align with well-known peaks in their published binding energies. This ensures that the identifications of the surface compounds are accurate. The spectra for the cathodes are calibrated with

Comment [GT3]: ??

Comment [GT4]: ??

respect to the binding energy of carbon black at 284.4 eV while the spectra for the anodes are calibrated with respect to hydrocarbons at 285.0 eV. The atomic concentrations are calculated using the integrated areas and the sensitivity factors provided by the manufacturer of the spectrometer. In this part of the research, XPS will also be utilized to create an atomic concentration depth profile of each set of electrode materials. Depth profile analyses are done using 4 keV Argon ions with a raster size of 5 x 5 mm^2 for the etching. The sputtering was made in 1.0 min intervals for a total sputtering time of 20 min. Multiplex spectra are collected in the same orbital regions listed above in between these 1.0 minute intervals using a pass energy of 35.75 eV and increments of 0.2 eV. The etching rate is determined by testing the process on a reference silicon wafer with a 1000 Å SiO_2 film. The etch rate was is determined to be approximately 20 Å/min. These parameters are monitored throughout the process and changes are made based on the survey scans.

Qualitative Analysis

The surface and depth profile analyses are split into separate procedures to preserve the samples. During the surface analysis, the argon control valve is shut and the power supply for the plasma electrodes remains off. XPS spectrums collected from extracted electrodes reveal key compositional differences between the surface chemistry on cells PD 01 and PD 02 and those on the CONT cell. In the interest of time, cell PD 03 was not analyzed and would be represented by the results found in cells PD 01 and PD 02. In the anode C 1s region (Figure 41), the peak assigned to Li_2CO_3 at 290.36 eV, which is a common side reaction product in lithium-ion batteries, was far more intense in the CONT anode spectrum than the same peak in spectrums collected from PD 01 and PD

02 respectively. Surprisingly, the anode C 1s spectrums PD 01 and PD 02 closely resemble the spectrum from an anode extracted from a fresh, uncycled LFP cell of the same batch (Figure 41). Accordingly, the signals which correspond to decomposed electrolyte, such as O-C=O and C-O bonds, are also far more intense in the CONT cell.

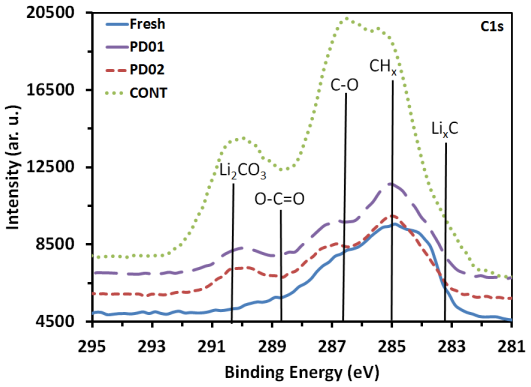

Figure 41: C 1s XPS spectrums of graphite anodes from a fresh cell, PD 01, PD 02, and CONT

This is an expected result previously published by multiple researchers showing these compounds reduce further to become Li_2CO_3. The stark contrast in the amount of reduced electrolyte compounds point outs several important facts about the anode electrolyte interface. First, the SEI layer is clearly more developed and may passivate the graphite particles on the anode in the CONT cell. This allows for the particles to be protected from further side reactions and may also provide a consistent low impedance medium for lithium ions to pass through at the 40 A rate. While there are smaller signs of this in the two pulsed discharged anodes, the intensity is greatly reduced in the signal. The hydrocarbon signal at 285.0 eV also represents impurities developed from decomposing electrolyte. Secondly, this analysis has shown once again that it is the continuous cell which shows the more commonly reported signs of cell degradation

despite being the cell that did not fail. This evidence further supports the hypothesis that the dominant degradation mechanism in high rate pulsed discharged cells is atypical. Third, these spectrums hint that it may be a degradation of the cathode that causes the large impedance rise and capacity fade. Normally, the focus of degradation research is on the anode electrode where the majority of the SEI growth occurs during the charging process. However, some researchers have claimed that the SEI layer actually only contribute a small amount to the impedance rise in a cell and can actually slow the rate of evolution. This seems to be the case in cells PD 01-03 and in the CONT cell for different reasons. In the case of the pulsed discharged cells, the cell's impedance rose rapidly while the XPS scans of the C 1s region in the anode show very low concentrations of SEI compounds. In the continuously discharged cell, there are high concentrations of SEI compounds corresponding to a rise in impedance. However, the rate of progression clearly slows as more cycled are conducted. For these reasons, it will be interesting to examine the C 1s region of the cathode as well to get a picture of the whole cell's chemical state.

Analysis of the XPS spectrums from the C 1s region of cathodes from cells PD 01 and PD 02 reveal a possible instability in the binder material. It is shown in Figure 42 that there is an additional large peak appearing at approximately 286.2 eV not present in the fresh cathode sample. This peak is assigned to C-O bonds like it was in the anode side, but there is another element to consider in the cathode that would appear in this region. The previous chapter briefly mentioned that the binder for the cathode material in these LFP cells is PVDF which has a carbon backbone structure. This compound has a signal that appears near the binding energy of C-O bonds. This is especially significant due to

the fact that the anode spectrum from the same region showed small amounts of decomposed electrolyte byproducts like C-O.

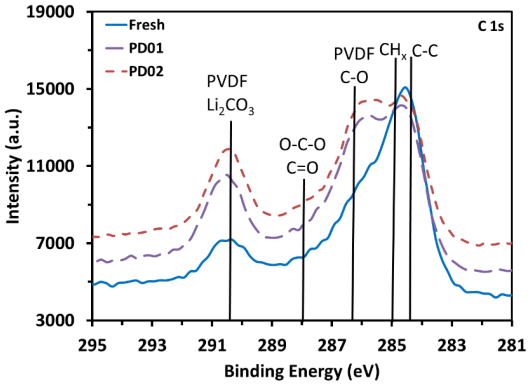

Figure 42: C 1s spectrums taken of LFP cathodes from a fresh cell, PD 01, and PD 02

These signals come from compounds formed in side reactions similar to the ones presented below in systems containing organic carbonates such as ethylene carbonate (EC) and dimethyl carbonate (DMC) as electrolyte.

$$EC + 2e^- + 2Li^+ \rightarrow (CH_2OCO_2Li)_2 + CH_2 = CH_2 \quad (9)$$

$$EC + 2e^- + 2Li^+ \rightarrow Li_2CO_3 + CH_2 = CH_2 \quad (10)$$

$$DMC + e^- + Li^+ \rightarrow CH_3OCO_2Li + CH_3 \quad (11)$$

$$Li_2O + EC \rightarrow LiOCH_2CH_2OCO_2Li \quad (12)$$

The lack of C-O signal in the anode means that these side reactions did not occur nearly as frequently as they did in the CONT cell. Accordingly, this also means that the C-O/PVDF signal in the C 1s region of the cathode spectrum may be mostly PVDF. Binder signal also appears near 290.4 eV where it coincides with the signal from the secondary reduction product Li_2CO_3. Lithium carbonate is a stable byproduct forming when the metastable electrolyte decomposition products from the above side reactions

are reduced further. This usually occurs due to impurities inside the cell, particularly water vapor. The common reactions which form lithium carbonate are shown below.

$$(CH_2OCO_2Li)_2 \rightarrow Li_2CO_3 + CO_2 + C_2H_4 + \frac{1}{2}O_2 \quad (13)$$

$$2ROCO_2Li + H_2O \rightarrow Li_2CO_3 + 2ROH + CO_2 \quad (14)$$

However, the same argument applies to these reactions and the initial decomposition products. It is likely that the peak at 290.4 eV is also dominated by signals from the binder. If these claims are both true, it would signal instability in the binder under the pulsed discharge cycling conditions. Binder dissolution, discussed in the introduction chapter, can occur under extreme temperatures. Binder material can react with electrolyte solvents and even be transported across to deposit on the anode surface [70]. In this case, the binder material is found in high concentrations on the electrode surfaces. It is argued that the results obtained from the C 1s region are described in this way. To complete the investigation into this claim, it is necessary to look at the other scanned regions, especially the F 1s region, for further evidence of binder dissolution.

The F 1s region from the anode electrode revealed a far higher magnitude signal from the region assigned to the compound LiF. As seen in Figure 43, the spectrums for the anodes from cells PD 01 and PD 02 shift towards the line at approximately 684.9 eV which is assigned to LiF. In contrast, the CONT cell and the fresh cell show more electrolyte salt compounds. There are several side reactions which can contribute to the formation of LiF during cell operation. First, after the side reactions occur to form Li_2CO_3, there can be a further reduction which produces LiF via reactions with cell impurities. Particularly, the $LiPF_6$ conducting salts tend to contain small traces of

hydrofluoric acid contaminant which can react with the lithium carbonate to produce LiF via the following reaction.

$$Li_2CO_3 + HF \rightarrow LiF + H_2CO_3 \quad (15)$$

LiF can then be deposited on the surface of the anode and impede the diffusion of lithium ions. Unlike Li_2CO_3 that forms a passivating and protective film, LiF has been identified as an ionically resistive compound which is sometimes found after long term storage of cells which use $LiPF_6$ as conducting salts. In the case of the pulsed cells, it is evident that the lithium fluoride formed preferentially when compared to the F 1s spectrums of the CONT and fresh cell. If a large concentration of LiF forms on the surface of the anode it will make it difficult for lithium ions to be exchanged during charging and discharging. This reduces the usable capacity at high rates and increases the internal cell resistance. It would explain the unusual evolution of the impedance and the rapid fade in capacity in the pulsed cells. Second, there is another interesting source for the LiF that could correspond to the findings on the surface of the cathode in the C 1s region. The LiF may also precipitate due to the dissolution of the binder material from the cathode.

Comment [GT5]: ??

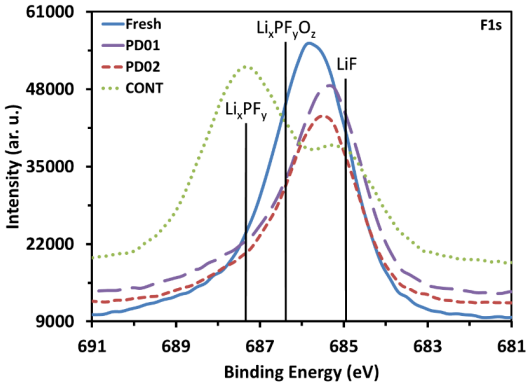

Figure 43: F 1s spectrums taken on graphite anodes from a fresh cell, PD 01, PD 02, and CONT

It has been reported previously that SEI compounds can break off and again react with the electrolyte to form more stable compounds [36].

With the unusual cycling conditions of the pulsed cell, it is possible that the pulsing induced a reaction between the broken off SEI compounds and the PVDF binder which produced LiF as a byproduct. While this claim is not documented in literature, it may explain the high concentration of PVDF on the cathode surface and the high LiF concentration on the anode surface. There are several documented reactions for the reduction of $LiPF_6$ which can produce both LiF and HF including:

$$LiPF_6 \rightarrow LiF + PF_5 \quad (16)$$

$$PF_5 + H_2O \rightarrow PF_3O + 2HF \quad (17)$$

$$PF_5 + 2xLi^+ + 2xe^- \rightarrow Li_xPF_{5-x} + xLiF \quad (18)$$

$$PF_3O + 2xLi^+ + 2xe^- \rightarrow Li_xPF_{3-x}O + xLiF \quad (19)$$

Many of these reactions involve degraded salt compounds, lithium-ions, and electrons and could mean that the pulsed discharge profile creates favorable conditions for them to occur. This is due to the localization of charged particles at the surface of each

electrode where the double layer forms. It is in this layer that the lithium ions are exchanged between the electrolyte and the electrode and where the stripped electron which passed through the load/power supply is rejoined with the ion. During the pulsing, there is a constant direction reversal of the charge flow. For a short while the same lithium-ions and electrons are localized at the interface. This may create more opportunities for the side reactions to occur. This is the leading explanation for why the cells are unable to accept charge at the 40 A rate only in the pulsed cells. This raises new questions about the cell design needed in order to power such a system.

When analyzing the F 1s spectra for the cathode electrode in Figure 44, the intensity of the PVDF signal located at approximately 687.7 eV is clearly magnified in the pulsed discharged cells in comparison to the fresh cell. In all three spectrums, the peak appears directly over or within 0.2 eV of the PVDF line. However, the intensity of the peak in the pulsed cells is approximately double in this region. This shows that the high concentration of PVDF seen in the C 1s region is not the result of decomposed electrolyte compounds overlapping in the same regions. The majority of the signal in these areas of the C 1s spectrum must come from raised concentrations of PVDF at the surface. The broadness of the peak in both the pulsed cells and the fresh cell indicates that there are partial contributions from salt compounds like $LiPF_6$ and $Li_xPF_yO_z$ which are located at 688.4 eV and 686.3 eV respectively. There is very little contribution from LiF considering the levels found on the surface of the anode. Surface films are normally studied at the anode interface since they normally form as a result of inefficiencies in the charging reaction [71]. This could explain why there is a high concentration of LiF at only the anode surface. If the LiF film forms simply because of the small increase in

Comment [GT6]: ??

charging time in the pulsed cells, it disproves the claim that the fast switching nature is the catalyst which induces this fade. The two ideas are mutually exclusive and will need to be investigated separately by using some sort of in-situ technique which can monitor the state of health of the cell as more pulsed cycle experiments are conducted. This will be addressed and discussed later.

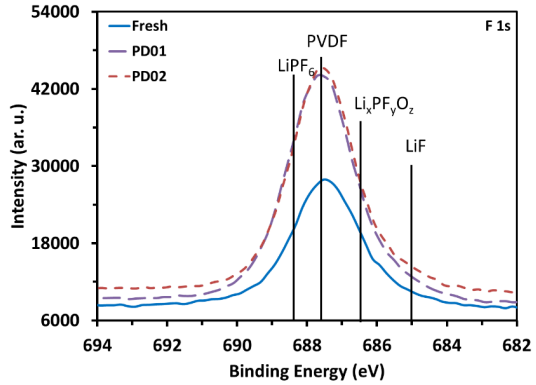

Figure 44: F 1s spectrums collected from LFP cathodes from a fresh cell, PD01, and PD 02

When analyzing the anode O 1s region in Figure 45, the spectrum reaffirms that there is a small concentration of Li_2CO_3 on the surface of the pulsed anodes in comparison to the CONT. The peak assigned to Li_2CO_3 and carbon-oxygen double bonds from decomposed electrolyte at approximately 531.8 eV is far more intense in the CONT cell. The level of these compounds in the pulsed cells very closely resembles the spectrum of the fresh anode. This has been true in both the O 1s region and the C 1s region. If the CONT weren't taken, it could be argued that the pulsed cells were near to their fresh state or were only cycled a few times. This spectrum reveals very small concentrations of SEI compounds on the surface with the majority of it being Li_2CO_3 based on its corresponding peak in the C 1s region.

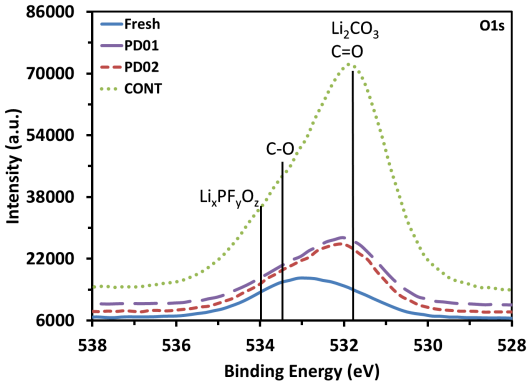

Figure 45: O 1s spectrums of graphite anodes extracted from a fresh cell, PD 01, PD 02, and the CONT cell

Accordingly, the O 1s region of the cathode shown in Figure 46, the magnitude of the signal in the regions assigned to Li_2CO_3 and carbon-oxygen double bonds is actually higher in the fresh cathode spectrum than in the pulsed cathodes. While the difference is relatively small, this can indicate the breaking down of Li_2CO_3 into LiF via the reaction in equation 15.

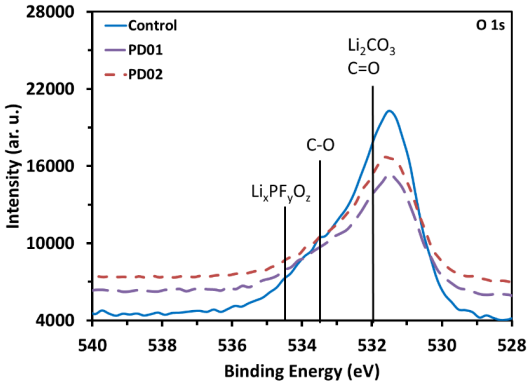

Figure 46: O 1s spectrums of LFP cathodes extracted from a fresh cell, PD 01, and PD 02

The O 1s spectrums from both the anode and the cathode electrodes reveal that the magnitude of decomposed electrolyte SEI compounds on the pulsed discharged electrodes are comparable to the amount detected on a fresh cell.

The P 2p region in both electrodes shown in Figure 47 and Figure 48 indicate no signs of the cathode phosphate structure breaking down in the pulsed cells and again reveal a stark contrast in the magnitude of degraded byproducts on the surface of the anodes. In the CONT cell, there is an obvious higher degree of deposited electrolyte salt, Li_xPF_y, on the surface of its anode compared to the anodes from the two pulsed cells, PD 01 and PD 02. This peak located at 137.0 eV is almost missing from the spectrum of the two pulsed cells and shows slightly less intensity than the fresh anode in this region.

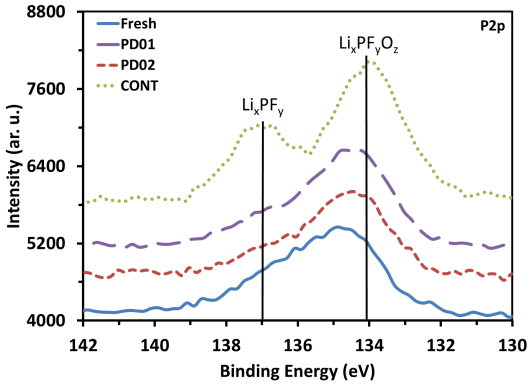

Figure 47: P 2p spectrums taken of graphite anodes from a fresh cell, PD 01, PD 02 and the CONT cell

On the cathode side, the pulsed cells show a slight broadening of the original peak centered around 133.6 eV assigned to $LiFePO_4$. This response is expected in that the new contributions from oxidized electrolyte salts ($Li_xPF_yO_z$) will distort the signals of the native LFP material. As indicated in the C 1s and F 1s regions, there is a much stronger contribution from PVDF which may mask some of the signal from the LFP particles. This

will be an interesting aspect to observe when the depth profile studies are conducted on these electrodes. The final multiplex spectra taken in this study were in the Li 1s and Fe 3s regions which showed little signal. It was difficult to learn anything valuable from the qualitative data alone. This should be addressed in the depth profiling and peak deconvolution analysis which is presented in the next section.

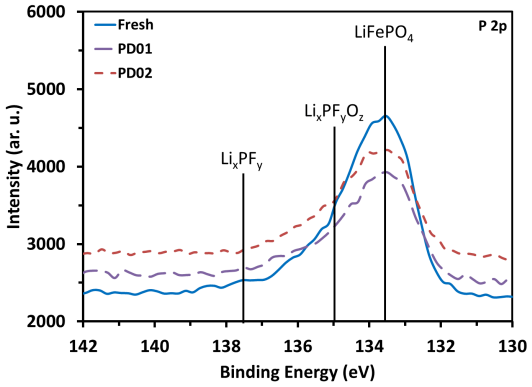

Figure 48: P 2p spectrums of LFP cathodes extracted from a fresh cell, PD 01, and PD 02

From a qualitative standpoint, the cathode spectrums from the two pulsed cells and CONT cell reveal there may be binder dissolution in the pulsed cells. It also surprisingly shows that the surface profiles of the pulsed cells are very similar to the fresh electrodes extracted from an uncycled cell. The CONT cell provides a stark contrast in that the spectrums revealed large signals from areas assigned to common degradation byproducts such as Li_2CO_3 and $Li_xPF_yO_z$. These findings also confirmed that the degradation mechanism which caused the eventual failure of the pulsed cells was consistent. The profiles between the two pulsed cells nearly overlap each other in all multiplex spectra collected. In order to get a proper perspective of the degree of difference between each of the electrode samples, a quantitative analysis will be

conducted to deconvolute the peaks in to their individual contributions. Furthermore, a depth profiling should be conducted using the Argon etching capabilities of the spectrometer to ascertain the penetration of the degradation products into the electrode material.

Quantitative Analysis

Deconvolution of the XPS spectrums is important in determining the actual atomic concentrations of the compounds identified in the qualitative analysis. The deconvolution works by fitting a set of Gaussian style peaks to the multiplex data and calculating the percent area covered by each contributing peak. It is possible to calculate the atomic concentration of each compound by multiplying the percent area by the total amount of atomic concentration of each element determined by the spectrometer during the survey scans performed before the multiplex scans. It is important to note that the atomic percentages presented in this section are the concentrations of an element which are a part of a specific compound's structure. For example, the atomic concentration of Li_2CO_3 in the C 1s region represents the amount of carbon atoms bonded with a binding energy characteristic to the lithium carbonate compound. While the amount of carbon identified as part of Li_2CO_3 can be a direct comparison to the actual atomic concentration of Li_2CO_3 due to the 1:1 ratio of C in Li_2CO_3. When viewing the contribution from the O 1s region it is important to account for the ratio change. There are 3 oxygen atoms to each Li_2CO_3 molecule. During the deconvolution, analysis efforts were made to only include peaks with a full width half maximum (FWHM) at or below 2.00 eV. Studies have shown that in an ideal scenario, deconvoluted peaks shouldn't have a FWHM of no more than 1.40 eV. This is not

always possible experimentally as there can be ghost signals which can arise and distort the signals. Therefore, a broad peak that seems as if it should be multiple peaks contributing is actually a result of distortion of the signal in the spectrometer or satellite signals. These aspects cannot be controlled and thus are taken into consideration when discussing the results of the quantitative analysis.

Comment [GT7]: ??

Table 5, Table 6, Table 7, and Table 8 show the results of the deconvolution of peaks for the anodes of cells PD 01, PD 02, CONT, and the fresh cell. Deconvolution of the peaks in the C 1s region quantified the Li_2CO_3 concentrations in the surface films of each cell as 3.0 at. %, and 2.9 at. %, 5.1 at. % of the total concentration of atoms on PD01, PD02, and CONT anodic surface films, respectively. The signal from the peak at 286.7 eV, assigned to C-O single bonds stemming from non-stoichiometric side reactions, would also intensify. The concentration of C-O bonds detected on PD01 and PD02 anodes were 5.6% and 5.2% respectively in contrast to 11.02% detected on the CONT anode.

Table 5: Quantitative analysis results obtained by deconvoluting peaks in multiplex spectrums in cell PD 01 anodes

Region	Binding Energies (eV)	FWHM	Concentration (at. %)	Assigned Compound
C1s	283.7	1.24	2.6	Li_xC
	285.0	1.86	9.7	Hydrocarbon
	287.1	1.92	5.6	C-O
	288.6	0.95	0.5	C=O
	290.0	1.86	3.0	Li_2CO_3
O1s	531.9	1.89	14.0	Li_2CO_3, C=O
	533.3	2.22	8.3	C-O
F1s	685.4	1.95	23.0	LiF
	687.5	2.50	5.3	Li_xPF_y
P2p	134.4	2.27	2.3	Phosphates
	136.5	3.07	1.2	Li_xPF_y

Li1s	56.0	1.93	24.6	LiF, Li_2CO_3

Table 6: Quantitative analysis results obtained by deconvoluting peaks in multiplex spectrums in cell PD 02 anodes

Region	Binding Energies (eV)	FWHM	Concentration (at. %)	Assigned Compound
C1s	283.7	1.22	1.7	Li_xC
	285.0	1.98	9.6	Hydrocarbon
	287.1	1.82	5.2	C-O
	288.9	1.93	1.2	C=O
	290.1	1.63	2.9	Li_2CO_3
O1s	531.9	1.89	15.8	Li_2CO_3, C=O
	533.5	2.10	8.7	C-O
F1s	685.5	1.93	22.5	LiF
	687.4	2.35	4.9	Li_xPF_y
P2p	134.4	2.25	2.4	Phosphates
	136.7	2.35	0.8	$LiPF_6$
Li1s	55.9	2.06	24.0	LiF

Table 7: Quantitative analysis results obtained by deconvoluting peaks in multiplex spectrums in cell CONT anodes

Region	Binding Energies (eV)	FWHM	Concentration (at. %)	Assigned Compound
C1s	283.27	1.48	1.6	Li_xC
	285	1.9	10.4	Hydrocarbon
	286.73	1.98	11.0	C-O
	288.87	2.02	3.4	C=O
	290.36	1.91	5.0	Li_2CO_3
O1s	531.76	2.04	23.3	Li_2CO_3, C=O
	533.5	2.31	8.8	C-O
F1s	684.96	1.91	5.3	LiF
	687.36	2.32	10.4	Li_xPF_y
P2p	134.01	2.32	1.6	Phosphates
	137	1.86	0.6	$LiPF_6$
Li1s	55.5	2.19	18.5	Li_2CO_3, LiF Li_xPF_y

Table 8: Quantitative analysis results obtained by deconvoluting peaks in multiplex spectrums in fresh anodes

Region	Binding Energies (eV)	FWHM	Concentration (at. %)	Assigned Compound
C1s	283.8	1.18	4.2	Li_xC
	285.0	2.00	9.0	Hydrocarbon
	286.9	2.00	5.5	C-O
	289.0	2.00	1.3	C=O
O1s	531.5	1.75	1.8	Li_2CO_3, C=O
	533.0	2.57	11.3	C-O
F1s	685.7	2.09	30.1	$LiF/Li_xPF_yO_z$
	687.8	2.84	4.1	Li_xPF_y
P2p	134.7	2.43	1.8	Phosphates
	136.8	2.43	1.0	$LiPF_6$
Li1s	54.1	1.75	2.6	Li_2O, LiOH
	56.3	1.97	27.2	Li_2CO_3/LiF

In the anodic O 1s region, the amount of oxygen detected that was assigned to Li_2CO_3 or C=O bonds at 531.9 eV was 14.0 at. %, 15.8 at. %, and 23.3 at. % of the surface compounds in PD01, PD02, and CONT anode surface films respectively. It's interesting that the calculated concentration of Li_2CO_3 is greater in the CONT anode surface film yet it continued to store charge at 15C. From deconvolution of the F 1s spectrum, the LiF concentration in PD01 and PD02 surface films were 22.5 at. % and 23.0 at. % respectively, while only 5.3 at. % in the CONT film. This was the greatest differential in concentration detected of a single surface film compound between the PD and CONT films. As mentioned in the quantitative analysis discussion, it's been documented that metastable products from side reactions like Li_xPF_y, $Li_xPF_yO_z$, and Li_2CO_3 can decompose further by reacting with impurities in the cell to form LiF, which is an ionically resistive compound [71]. The quantitative XPS analysis shows that in the early development of the surface films on PD01 and PD02 anodes the conditions were more

Comment [GT8]: Values to go along with % ??

Comment [GT9]: ??

favorable for the formation of LiF while the CONT cell developed films rich in reduced electrolyte compounds like Li_2CO_3. Regardless of which specific reactions are taking place, LiF, an ionically impeding compound, was clearly more favorably precipitated on the anodes of the two pulsed discharged 26650 LFP cells when the Navy's high power pulsed loading was being simulated. Based on the EIS evolution and the evidence from, XRD, XAS, and XPS analysis in both qualitative and quantitative forms, the preferential formation of LiF is the principal cause for the difference in degradation behavior between pulsed discharged cells and continuously discharged cells at high rates. It is still possible that the LiF stems from the dissolution of the binder material in the cathode electrode. Deconvolution of the cathode regions will assist in proving or disproving this claim. In conclusion, XPS has shown that pulsed discharged cells developed surface films that contained high concentrations of LiF which led a dramatic increase in the low frequency impedance resulting in a rapid capacity fade at 40A charging rates.

On the other hand, the deconvolution of the peaks in the cathode spectrums reveal that there is a large increase in there is a large increase in the atomic concentration of fluoride and carbon bonds which are characteristic of PVDF. are characteristic of PVDF. Due to the lack of samples available from the continuous cell, CONT, there was no cell, CONT, there was no cathode analysis conducted on that cell. Table 9, Table 10, and

Table 11 present the results of the deconvolution analysis of cathodes in cells PD 01, PD 02, and the fresh cell. Initially when examining the data, the pulsed cells are again nearly identical in their atomic concentration profiles across all analyzed sections. In the C 1s region, it is clear that the concentration of PVDF increases dramatically in the pulsed discharge cells. The concentration of carbon bonds which registered as PVDF in cells PD 01 and PD 02 were 17.3 at. % and 17.2 at. % respectively while the fresh cell

was 12.9%. The increase in PVDF concentration can also be drawn from the deconvolution of the F 1s peak which showed 32.0 at. % and 31.7 at. % of atoms on PD 01 and PD 02 respectively are fluorides which are part of the PVDF molecule. In comparison, the fresh cell showed only 16.6 at. % of atoms were fluorides from PVDF. It was originally expected, based on the concentration of LiF atoms found in the deconvolution of spectrums on the anode side, that there would be a substantial amount of LiF contributing fluorides on the surface of the cathode. However, the concentration of LiF fluorides detected on cathodes from both pulsed cathodes are 1.5 at. % while the fresh cell registered 0.6 at. %.

This raises some questions about which side reaction produced the formation of the LiF on the anode surface in the pulsed cells. In one case, the pulsed discharging may make the formation more favorable by the promotion of the decomposition of metastable electrolyte compounds to form LiF. On the other hand, if the fluoride in the cathode binder decomposed and reacted with the electrolyte, it is possible that they were transported across the separator and deposited as LiF on the surface of the anode. In both cases, the high concentrations of PVDF on the surface of the cathode and high concentration of LiF on the anodes only appear in cells which have been pulsed discharged. This proves that the nature of the switching in the pulsed discharge profile plays a major role in making the conditions favorable for these events to occur.

Table 9: Quantitative analysis results obtained by deconvoluting peaks in multiplex spectrums from PD 01 cathodes

Region	Binding Energies (eV)	FWHM	Concentration (at. %)	Assigned Compound
C1s	284.4	1.24	18.4	C-C
	286.0	2.00	17.3	PVDF
	288.1	2.00	3.3	O-C-O
	290.5	1.39	8.3	$PVDF/Li_2CO_3$
	290.7	3.59	0.0	C satellite
O1s	531.4	1.73	9.5	$LiFePO_4$
	533.2	2.30	4.0	C-O
F1s	685.3	1.61	1.5	LiF
	687.6	2.20	32.0	PVDF
P2p	133.6	1.76	1.7	Phosphates
	135.0	2.60	1.3	$LiPF_6$
Fe3s	93.6	3.39	2.6	$LiFePO_4$

Table 10: Quantitative analysis results obtained by deconvoluting peaks in multiplex spectrums from PD 02 cathodes

Region	Binding Energies (eV)	FWHM	Concentration (at. %)	Assigned Compound
C1s	284.4	1.24	19.0	C-C
	285.9	2.00	17.2	PVDF
	287.9	2.00	3.3	O-C-O
	290.6	1.52	9.0	$PVDF/Li_2CO_3$
	290.7	3.59	0.0	C satellite
O1s	531.4	1.72	8.3	$LiFePO_4$
	533.1	2.30	4.7	C-O
F1s	685.3	1.62	1.5	LiF
	687.6	2.25	31.7	PVDF
P2p	133.5	1.79	1.7	Phosphates
	134.9	2.97	1.1	$LiPF_6$
Fe3s	93.2	3.63	2.5	$LiFePO_4$

Table 11: Quantitative analysis results obtained by deconvoluting peaks in multiplex spectrums from LFP cathodes from a fresh cell

Region	Binding Energies (eV)	FWHM	Concentration (at. %)	Assigned Compound
C1s	284.4	1.24	28.5	C-C
	285.7	2.00	12.9	PVDF
	287.7	2.00	2.7	O-C-O
	290.5	1.59	4.6	PVDF/Li_2CO_3
	290.7	3.59	0.0	C satellite
O1s	531.5	1.69	16.7	$LiFePO_4$
	533.2	2.30	7.9	C-O
F1s	685.0	1.64	0.6	LiF
	687.5	2.63	16.6	PVDF
P2p	133.5	1.77	3.2	Phosphates
	134.7	2.58	2.0	$LiPF_6$
Fe3s	93.1	2.83	4.5	$LiFePO_4$

XPS quantitative analysis has shown evidence that binder dissolution occurs in the cathodes of pulsed discharged cells while the anodes have a high concentration of LiF. In comparison to a cell cycled with a continuous discharge profile, the analysis proved that the linear fade is a cause of the side reactions which consume active material and degrade electrolyte solvents which forms metastable compounds that deposit on the surface of the anode. This is conventional behavior which has been widely discussed among battery scientists. However, the unique events which occurred in the pulsed electrodes cannot be explained by conventional theories. This is due to the fact that the discharge profile is the only difference between the cells. Therefore, the act of overcharging, overdischarging, high thermal stress, or high rate cycling cannot alone explain the degradation phenomenon in the pulsed cells. The concentration profiles seem to indicate that the rapid fade of the pulsed LFP cells corresponds to a growing LiF rich surface film and increased contact resistance in the cathode due to binder

dissolution. At some point, there is a critical concentration of fluoride compounds on the surface of both electrodes which causes the internal resistance to rise rapidly and slow the kinetics of the charging process.

Depth profiling of the LFP and graphite electrodes

In order to understand the critical point where the surface concentration shifts to an unfavorable degree, depth concentration profiles of the electrode materials must be considered. One-minute etching sessions are conducted on both cathode and anode samples for a total period of twenty minutes. This corresponds to a 400 Å depth profile of the electrodes post-cycling. The idea is to study the degree of penetration of the binder dissolution and the fluoride compound buildup in the cathode and anode respectively. This is essential since it was seen in the qualitative XPS analysis that the failed pulsed electrodes had spectrums which were very similar to the fresh electrodes. Therefore, it is important to see if the profiles differ with respect to the depth axis and if so, at what point the pulsed electrode profile directly mimics the fresh profiles.

In Figure 49, Figure 50, Figure 51, and Figure 52 the trend for the atomic concentration of the scanned elements is shown as a function of the amount of etching time for the anode from cells PD 01, PD 02, CONT, and the fresh cell respectively. As with the surface profiles, the two pulsed cells show nearly identical atomic concentration depth trends. The fluoride concentration is higher in the fresh anode across the entire depth than either of the pulsed cells. In all three anodes, the fluoride concentration rebounds after the surface scan and increases to approximately 40.0 at. % in the fresh anode and approximately 37.0 at. % in the pulsed cells. In both cases the fluoride concentration trends negatively as deeper scans are conducted. This behavior may be explained by

the presence of $LiPF_6$ salts which have impregnated the anode. This is natural and will provide good ionic conductivity to the graphite when the cell is cycled. It is even more interesting that the fluoride and lithium concentrations trend almost identically for the first eight minutes of etching in cell PD 01. The random spikes in concentration can be explained by the randomness at which certain sections of the electrode foil are wetted with electrolyte and thus when analyzing a small area, the concentration of electrolyte salts would also fluctuate. However, the top 160 Å of electrode material are nearly uniform in lithium and fluoride concentration indicating that there exists a consistent film in this depth. Also, there is a large drop in the concentration of oxygen atoms and carbon atoms between the surface and 20 Å depth. This may be the area where the degraded electrolyte side reaction products are formed and deposited. The deeper material shows a drop in carbon and oxygen due to the fact that these products are further reduced to form LiF which intercalates into the graphite. The fresh cell also has a sharp drop in the oxygen concentration but levels out after the first minute of etching compared to the gradual decrease seen in the two pulse anodes. When comparing these to the concentration profile of the CONT anode, it is clear that the oxidized electrolyte products are more persistent with respect to depth meaning the surface film is much thicker. Like the first eight minutes of etching in cell PD 01, the concentration trend is relatively flat across the entire twenty minutes of etching.

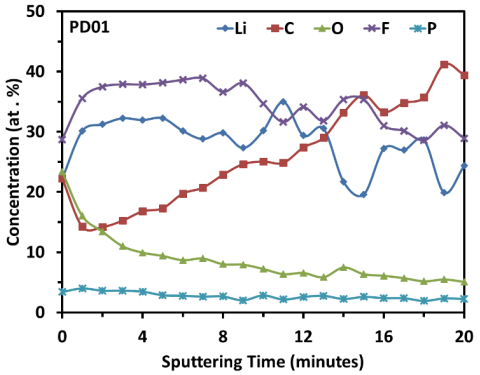

Figure 49: Atomic concentration vs. sputtering time of all scanned regions of anodes from cell PD 01

The fluoride concentration is almost 20% less across the analyzed depth compared to the two pulsed anodes and the fresh anode. This data demonstrated that in normal linear fade at high cycling rates, the side reaction products deposit on the surface and form a thick passivating film over the surface of the graphite particles which has a consistent concentration profile with respect to depth. This demonstrates the consistency of the degradation process in the CONT cell. On the other hand, high rate pulsed discharged cells for very thin films comprised mainly of fluoride compounds which doesn't necessarily have a consistent composition depth profile. Under the same amount of conducted cycles, the pulsed discharged anodes develop a shallower surface film with high concentrations of fluorides throughout.

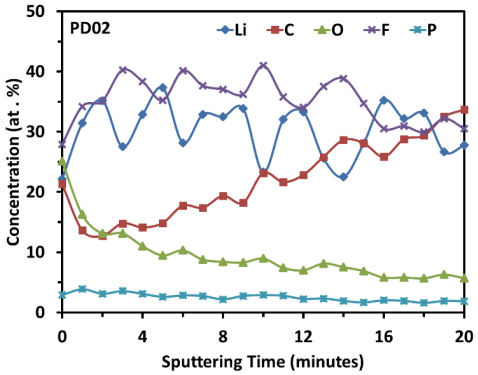

Figure 50: Atomic concentration vs. sputtering time of all scanned regions of anodes from cell PD 02

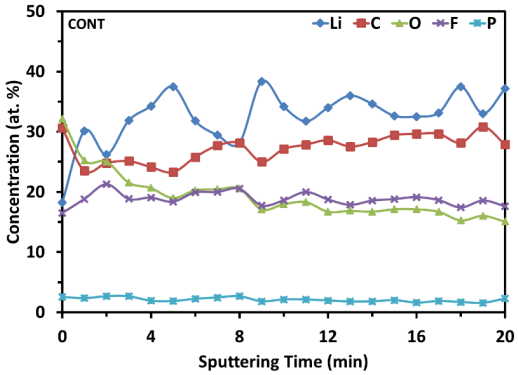

Figure 51: Atomic concentration vs. sputtering time of all scanned regions of anodes from the CONT cell

When looking at the same analysis on the cathode side seen in Figure 53, Figure 54, and Figure 55, the data indicates the depth of the PVDF dissolution is shallow. While the surface concentration of fluorides is higher on the initial surface scan (above 30%), it immediately drops after one minute of etching.

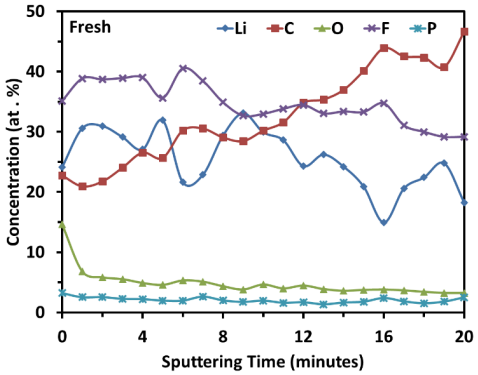

Figure 52: Atomic concentration vs. sputtering time of all scanned regions of anodes from a fresh cell

After one minute the fluoride concentration is approximately cut in half in both cells PD 01 and PD 02. In response, the iron and oxygen concentrations immediately increase and level off within the top 60 Å. This means that the high concentration of PVDF detected in the surface profiling exists only at the electrode-electrolyte interface. If binder dissolution really occurred, then it only happened in the top layer of electrode material. The carbon signal in the pulsed cell depth concentration profiles also decreases sharply in the top 60 Å of material. The major difference between the pulsed cathodes and the fresh cathode in the carbon depth profile is that after one minute of sputtering the carbon concertation increases slightly in the pulsed cells while the fresh cathode shows a linear decrease in the top 60 Å. This could be due to the small amount of SEI product which deposits on the surface of the cathode.

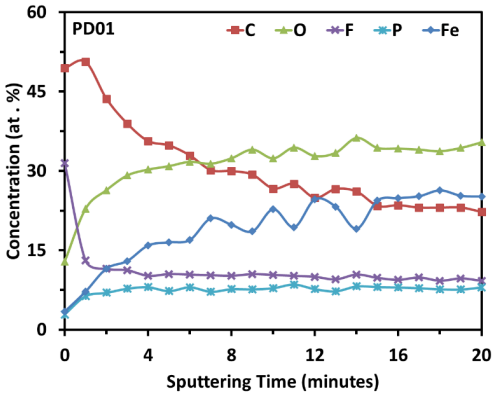

Figure 53: Atomic concentration vs. sputtering time of all scanned regions of cathodes from cell PD 01

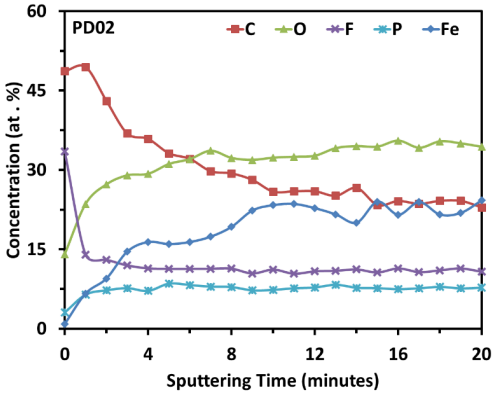

Figure 54: Atomic concentration vs. sputtering time of all scanned regions of cathodes from cell PD 02

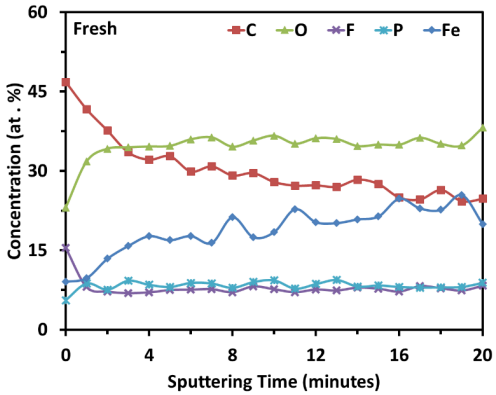

Figure 55: Atomic concentration vs. sputtering time of all scanned regions of cathodes from a fresh cell

The most important conclusion gained from this analysis is that the degradation in the pulsed cells which causes them to fail exists mainly within the top 200 Å of cathode and anode material. This validates the conclusions made from other analysis techniques in this research that the fast switching in pulsed discharged cells creates favorable conditions for certain degradation events to occur at the interfaces.

To achieve more information about the changing identified compounds as a function of etch depth, the individual anode multiplex scans are plotted on top of each other. This illustrates which compounds are present at different depth to enhance the information which was presented in the elemental depth charts above. Only the anode side was analyzed since based on the initial depth analysis, the effects are confined to the top 40-60 Å of the cathode electrodes. Cell PD 05 which was discussed in the XAS section and used as a compare and contrast against the results found in cells PD 01-03, is also plotted and discussed here to provide a reference to a cell which underwent pulsed discharging but didn't fail. Because the pulsed cells were so similar in surface and depth

profiles, the PD 02 spectrums are the only ones shown in this section. In the anode C 1s region seen in Figure 56, Figure 57, and Figure 58, it is clear that the same is true for the anodes. Only the initial 40 Å shows any signs of change from the native peak, C-C bonds, which become the only peak which appears after that depth.

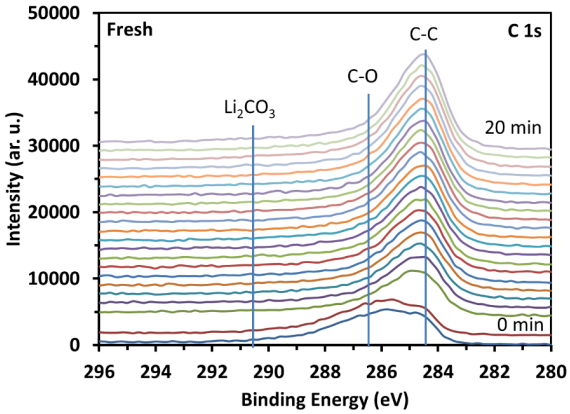

Figure 56: C 1s depth spectrums for 20 minutes of etching on graphite anodes from a fresh LFP cell

The plot from the C 1s region of the CONT anode in Figure 59 shows a similar effect with the degradation compounds only appearing in the first 3-5 spectrums. The SEI layer only spans a maximum of 60-100Å of the depth of the graphite anode. This corresponds well with the elemental depth analysis.

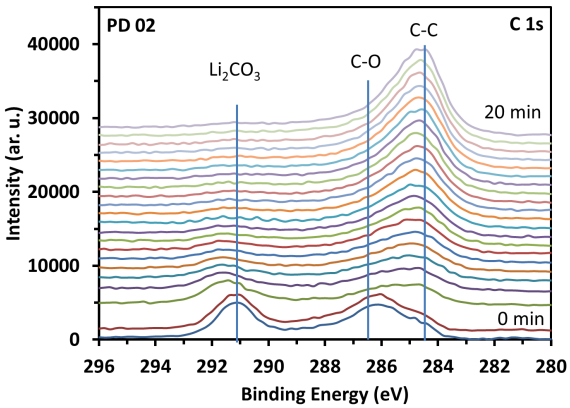

Figure 57: C 1s depth spectrums for 20 minutes of etching on graphite anodes from cell PD 02

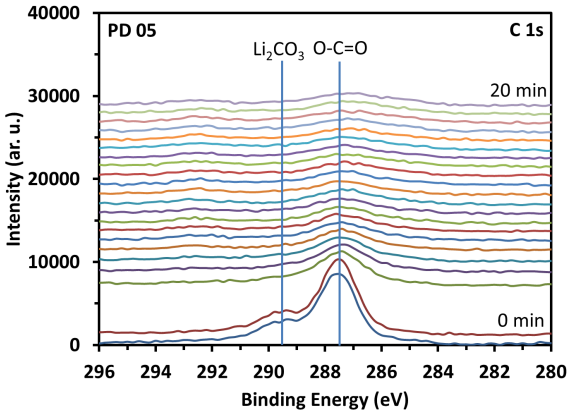

Figure 58: C 1s depth spectrums for 20 minutes of etching on graphite anodes from cell PD 05

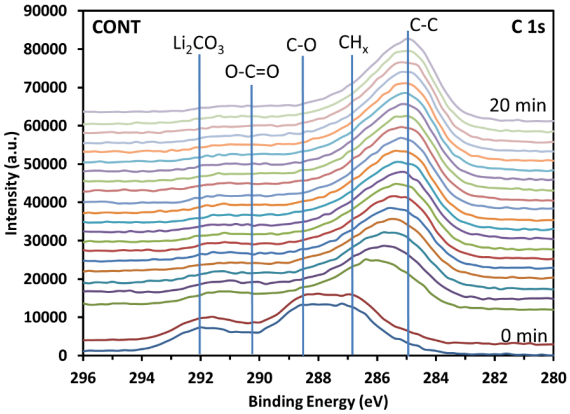

Figure 59: C 1s depth spectrums for 20 minutes of etching on graphite anodes from the CONT cell

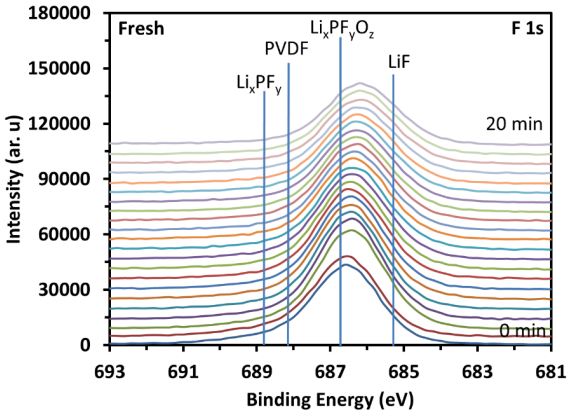

Figure 60: F 1s depth spectrums for 20 minutes of etching on graphite anodes from a fresh cell

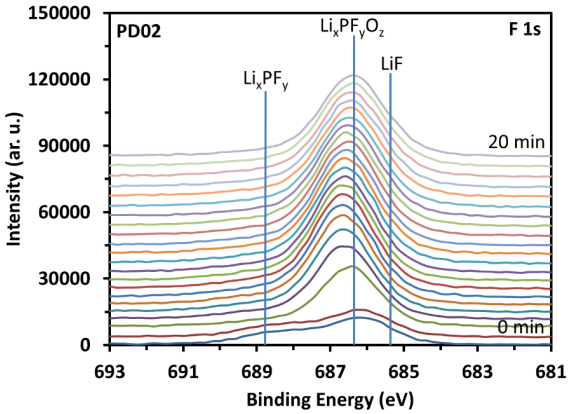

Figure 61: F 1s depth spectrums for 20 minutes of etching on graphite anodes from cell PD 02

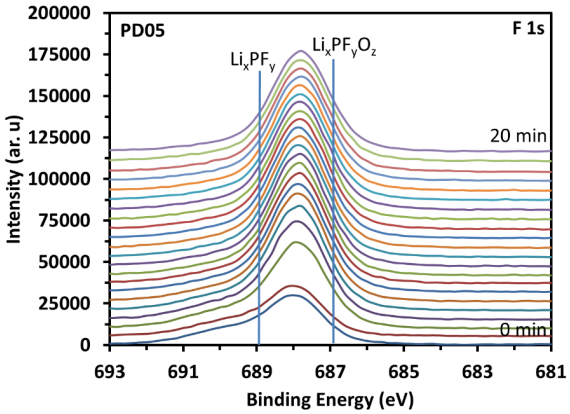

Figure 62: F 1s depth spectrums for 20 minutes of etching on graphite anodes from cell PD 05

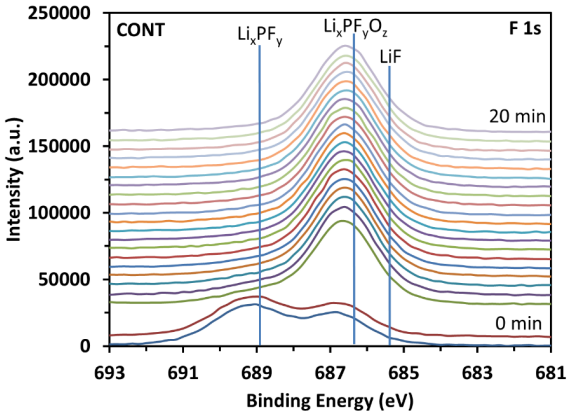

Figure 63: F 1s depth spectrums for 20 minutes of etching on graphite anodes from the CONT cell

In both the fresh anode and PD 02 the spectrums in this region become flat as deeper material is scanned. This indicates that there is very mild oxidation of the carbon in the anode of the pulsed cells. As stated, the pulsed cell spectrums were very much like the ones seen in the fresh anode. However, in the CONT cell, the spectrums never flatten at any of the scanned depths. This shows the deeper degradation which exists in the CONT cell and magnifies the mild degree of degradation in the pulsed cells even though they failed to accept charge at 40 A after the same amount of cycles.

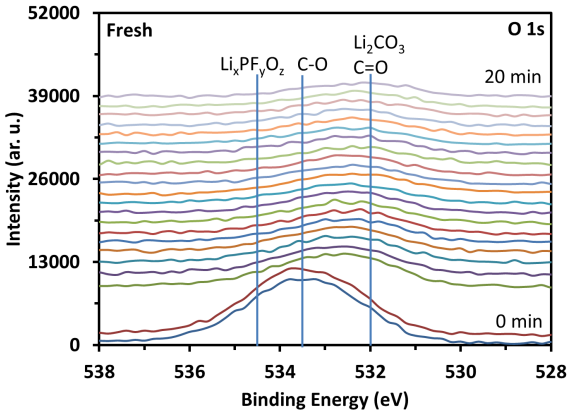

Figure 64: O 1s depth spectrums for 20 minutes of etching on graphite anodes from a fresh cell

In the P 2p regions of the analyzed anodes shown in Figure 68, Figure 69, Figure 70, and Figure 71, cell PD 02 is the only analyzed cell showing a large response after 3 minutes of etching. The peak corresponds to oxidized electrolyte salt compounds or $Li_xPF_yO_z$. The electrolyte salts break down early and deposit on the anode before the LiF films develops over it and mask the signal on the surface scans. This signal dies off in intensity after two etching sections meaning that there is not deep penetration of these compounds into the graphite matrix.

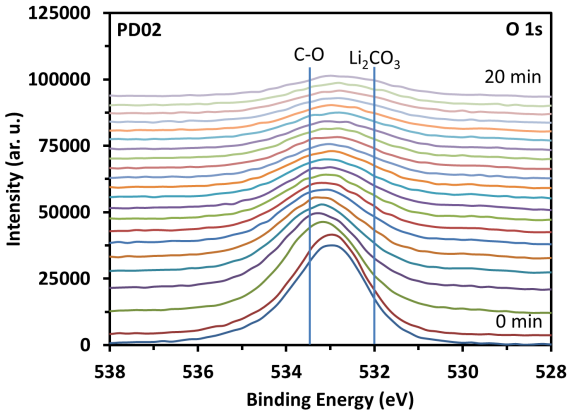

Figure 65: O 1s depth spectrums for 20 minutes of etching on graphite anodes from cell PD 02

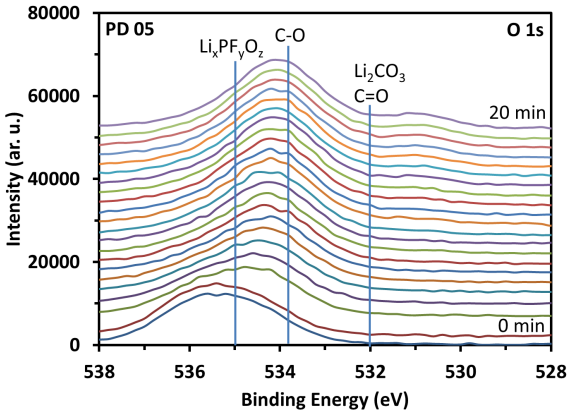

Figure 66: O 1s depth spectrums for 20 minutes of etching on graphite anodes from cell PD 05

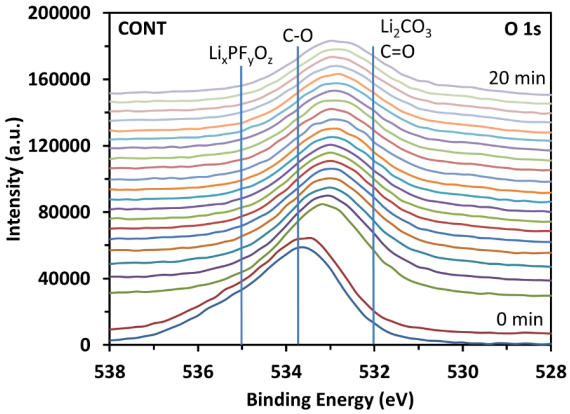

Figure 67: O 1s depth spectrums for 20 minutes of etching on graphite anodes from the CONT cell

Both cells PD 02 and PD 05 depth spectrums show a shallow signal in the P 2p region even at twenty minutes of etching. The fresh graphite electrode flattens after four minutes of etching. In the CONT cell, the same shallow peak exists after 20 min of etching as in the two pulsed cells, PD 02 and PD 05. The spectrums collected from the CONT cell and cell PD 05 are very similar with the intensity of the peak from CONT being greater than PD 05. The anomaly in this region exists only in cell PD 02 at 40 Å depth.

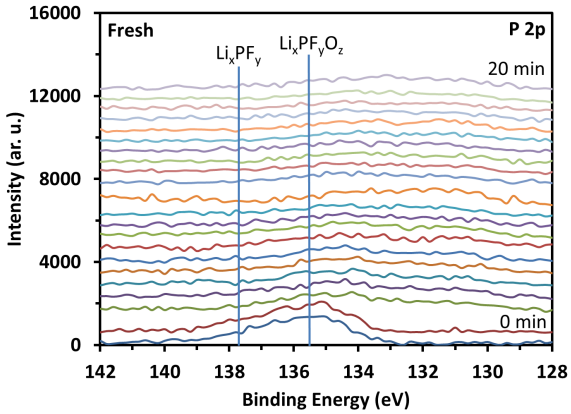

Figure 68: P 2p depth spectrums for 20 minutes of etching on graphite anodes from a fresh cell

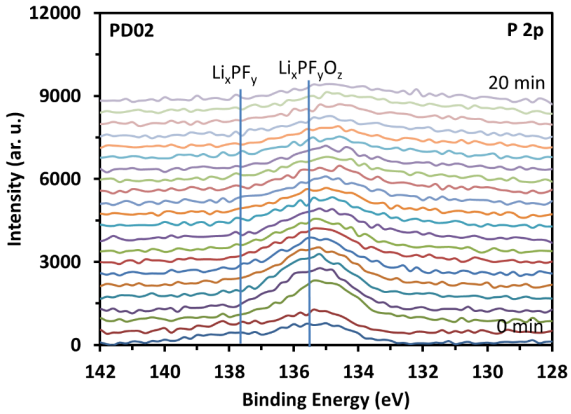

Figure 69: P 2p depth spectrums for 20 minutes of etching on graphite anodes from cell PD 02

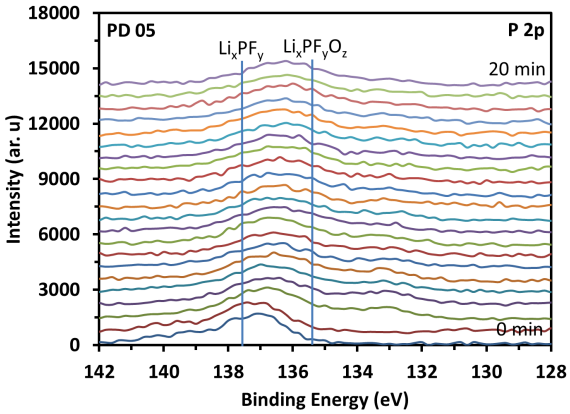

Figure 70: P 2p depth spectrums for 20 minutes of etching on graphite anodes from cell PD 05

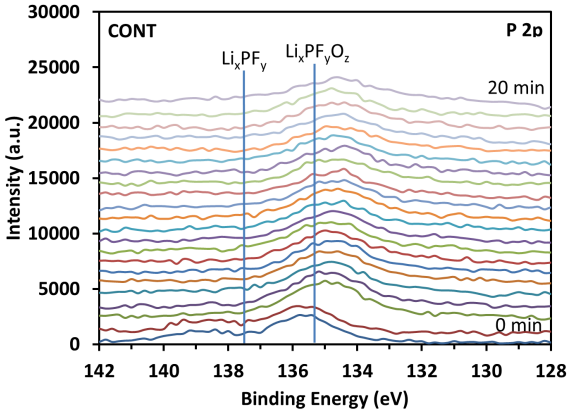

Figure 71: P 2p depth spectrums for 20 minutes of etching on graphite anodes from the CONT cell

These spectra help to lay out a comprehensive story for what degradation events occurred in these cells. From the XPS depth analysis, it is concluded that the films developed in failed pulsed cells are thin and contain high concentrations of LiF only in the top 20-40 Å of the extracted electrodes. The P 2p region seems to indicate that the process begins with the early oxidation of the electrolyte salts which intercalate into the graphite matrix. When the LiF is formed from the breakdown of the salts, the film shields

the signal from the oxidized salt products. This means that the high concentration of PVDF found on the surface of the pulsed cathodes is an independent event which does not contribute to the LiF formation on the anode as originally theorized. At this point, the data collected has given insight into the specific chemical reactions which occur which contribute to the unique fade characteristics in high rate pulsed discharged cells which experienced a lack of ability to charge at high rates after less than one hundred cycles. From here, the chemical reactions and degradation phenomenon discovered from surface/depth profiling and atomic structure analysis should be tied to specific cycling profile steps which are mainly responsible for creating the favorable conditions for them to occur. The final piece of the hypothesis which is not yet heavily supported by data collected in this research is that the high frequency switching nature of pulsed profiles induces these phenomena. In order to validate this, a similar atomic composition analysis needs to be conducted on cells cycled with profiles containing different pieces of the pulsed profile.

Breaking down the pulsed profile

It was noted in the introduction that steps were taken to eliminate contributions to degradation made by aspects of the cycling profile such as thermal stress, over-charging, and over-discharging by installing the same parameters in the profile for the continuous cell. However, in order to understand which cycling procedures induce the conditions favorable for the identified chemical reactions to occur, the profile must be broken down. In this section, data is presented on cells which are cycled with profiles that are partials of the original pulsed profile. XPS analysis will also be conducted on these cells to see what each cycling step adds or subtracts to the overall electrode

composition post-mortem. Three profiles are tested in this section. In the first test profile, the one second recharge in the discharge profile will be eliminated and replaced with a rest step so that it mimics the duty cycle experiments presented in Chapter 1. In the second profile, the 40 A continuous recharge step will be replaced by a 1C, 2.6 A continuous recharge in order to isolate the high rate pulsed discharge steps. Finally, there are two cell cycled using the exact same procedure as the initial pulsed cells which showed rapid fade. In order to completely rule out any equipment malfunctions as well, these cells were cycled at the Naval Surface Warfare Center-Carderock Division on a similar industrial cycler as was used to cycle the initial cells. It should be noted that other profiles were tried but were deemed unable to present any useful data. For example, pulsed discharge cycles were conducted with a reduced voltage range of 3.65 V to 2.5 V which is the nominal range for the LFP chemistry. In these cells, it was found that the 40 A continuous recharge step didn't successfully store any usable capacity even in the first cycle. Thus, the discharge step depleted what capacity was stored in the initial low rate charge of the cell and never recovered. This confirmed that even though the voltage range is extended in the initial pulsed discharge experiments, the level of charge and discharge do not exceed the normal limits of the cell. This is due to the fact that the voltage-drop in the cell under a 40 A load is far greater than the drop under nominal rate. Therefore, there is no actual overcharging or overdischarging of the cell in the case of the failed cells. Table 12 shows the list of procedures that are tested in this study and their designations.

Table 12: Cycling parameters for Cell 1-4 in the effort to break down the PD profile

Cell #	Cycling Procedure	End Capacity	Cycles Performed
1	40 A, 5s/1s Rest PD, 4.1-2.0V, Continuous 40 A Recharge	0 Ahrs	22
2	40 A, 5s/1s PD, 4.1-2.0V, Continuous 40 A Recharge	0 Ahrs	12
3	40 A, 5s/1s PD, 4.1-2.0V, Continuous 40 A Recharge	0 Ahrs	33
4	40 A, 5s/1s Rest PD, 4.1-2.0V, Continuous 2.6 A Recharge	2.08 Ahrs (2.6 A Rech)	100

Figure 72 shows the capacity fade for Cell 1, 2, and 3 which fades rapidly as seen in the previous experiment. Cell 4 which underwent 3A recharge showed linear fade but was not plotted with the other cells due to the incompatibility of comparing the 40 A continuous recharge to the 2.6 A recharge in Cell 2. The capacity for Cell 4 shows linear fade of the 2.6 A recharge capacity in the first 25 cycles. In contrast, Cells 1, 2, and 3 fade rapidly in the first 12 cycles in similar fashion to cells PD 01-03 in the initial study. Cell 1 is cycled with a rest step in replacement of the one second recharge that is in the original pulsed profile used in Cells 2 and 3. The results of the fade behavior reinforce the previous claim that the extra charging time introduced with the one second recharge step is not the deciding factor between fading rapidly and the traditional linear fade behavior.

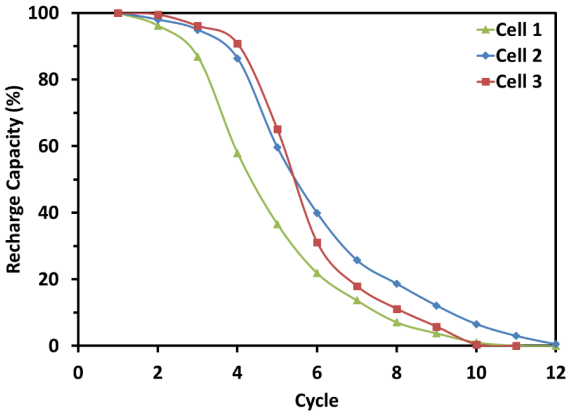

Figure 72: Percent capacity fade plot for Cells 1, 2, and 3.

EIS spectrums of the four test cells are shown in Figure 73 and reveal the same phenomenon seen in the original study with the mid-frequency semi-circle separating into two separate semi-circles. Most interestingly, the EIS spectrum taken of Cell 04, the only cell which did not show rapid fade, did show signs of narrowing and stretching along the real impedance axis. This means that although Cell 4 did not show rapid fade in the 2.6 A recharge capacity, that perhaps performing a 40 A cycle would reveal that similar electrochemical degradation is occurring within it as well. These experiments have shown that this separation is indicative of the failure mode discovered in the materials characterization presented in the previous chapters. However, the previous analysis concluded that the impedance rise which caused the rapid capacity fade in the original study on these LFP cells, is caused by the rapid switching nature of the pulsed profile. This switching consistently changed the direction of the flow causing active material to preside for longer times near the interface of the graphite electrode and the electrolyte where side reactions occur. Combined with the fatigue-like stresses that this type of profile places on the material and the thin surface film, the conditions become

favorable for the breakdown of compounds in the surface film to form LiF rich films. The fact that Cell 1 failed in the same fashion indicates that this is not the method that causes the precipitation of LiF rich films. In Cell 1, the one second rest would allow a short moment for the cell to settle before the load was turned on again and the circuit completed. Therefore, it is possible that the failure mechanism in this cell may be different from the rest. This will be discussed next as the results of the XPS surface analysis is presented.

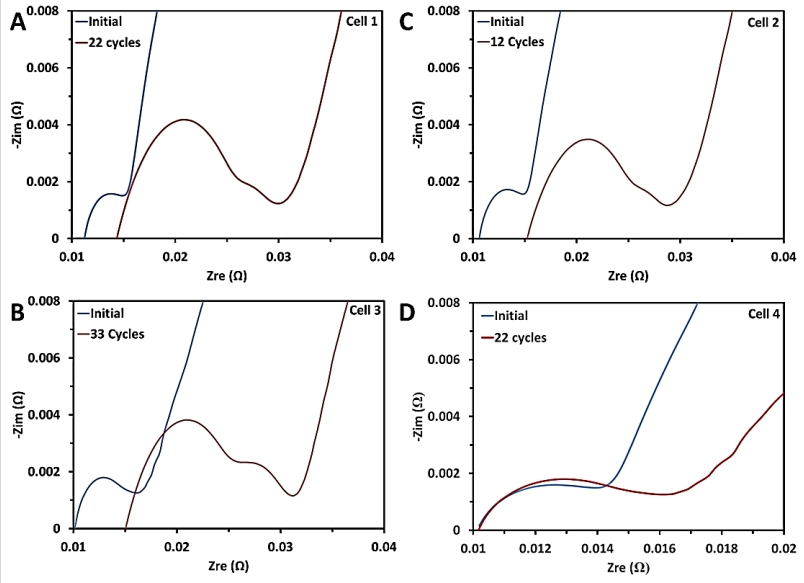

Figure 73: EIS spectrums collected on Cell 1-4 before and after cycling is performed

Due to limited access to the XPS spectrometer at the Navy research center, the surface and depth analysis of Cell 4 was not completed. The real interest in this analysis is to examine the consistency of the failure mechanism in Cells 2 and 3 while comparing their surface profiles to what is found in Cell 1 to see if they exhibit the same surface chemistry. Ultimately, it will be interesting to see if the same side reactions are

responsible for the fade in Cell 1 as was in Cell 2 and 3 along with the original pulsed cells. Because of these reasons, it was decided that the analysis should focus on the graphite anodes for proper comparison. Figure 74 shows the C 1s region for Cells 1, 2, and 3 which shows very similar spectrums for all three cells. In fact, the three cells have C 1s regions that are like PD 01 and PD 02 in the previously presented data.

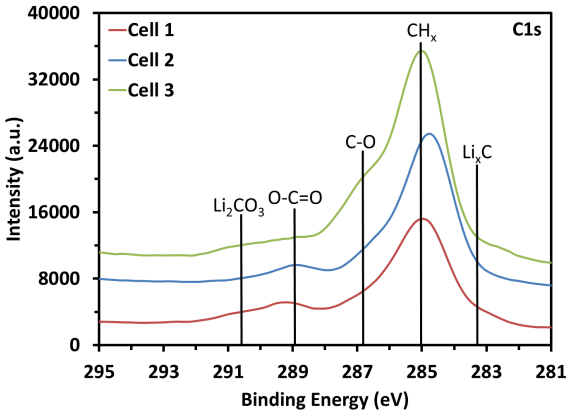

Figure 74: C 1s spectrums from anodes of Cells 1, 2, and 3 in the breakdown study

Again, compared to the continuously cycled cell, the intensity of the peaks is far lower with the concentration of decomposed electrolyte products like O-C=O and Li_2CO_3. In the previous spectrums for PD 01 and PD 02 a peak exists at approximately 286.8 eV which was assigned to C-O bonds which stemmed from partially decomposed electrolyte solvents. This peak is virtually non-existent in the C 1s spectrums of Cells 1, 2, and 3.

In the F 1s region shown in Figure 75, Cell 1 shows a very different degree of the peaks which appeared in Cells 2 and 3. In all three cells there seems to be a stronger contribution from electrolyte salts. This is evident by a presence of the peak located at

approximately 687.3 eV which is assigned to Li_xPF_y. In the previous cells PD 01-03, this peak was suppressed and only the one peak near 685 eV was present. Interestingly, Cell 1 which was substituted with the one second rest step, has a far stronger signal from the 685.0 eV peak which is assigned to LiF.

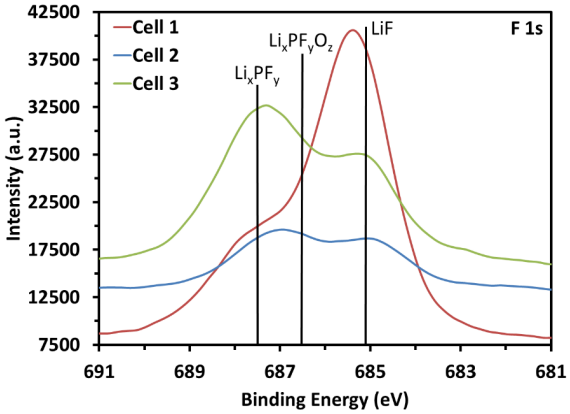

Figure 75: F 1s spectrums from anodes of Cells 1, 2, and 3 from the profile breakdown study

Compared to the spectrums from Cell 2 and 3 in this region, it would seem that the concentration of LiF is actually higher in the anodic surface film of Cell 1. Like the EIS results, this data indicates that the bipolar nature of the original pulsed procedure is not the detrimental factor to failure of these LFP cells. While all three cells had the same capacity fade and EIS behavior, the Cell 1 spectrum in the F 1s region shows that the conditions were even more favorable for the formation of LiF.

In the O 1s region shown in Figure 76, Cell 3 shows an intensity in the Li_2CO_3/C=O peak which is comparable to the CONT cell. Even though all three cells failed in the same number of cycles, Cell 3 developed a film containing higher concentrations of decomposed electrolyte compounds. Cell 1 and 2 are similar to the spectrums from the

initial pulsed degradation study with low intensity and slightly skewed towards the peak position for oxidized electrolyte salt, $Li_xPF_yO_z$ assigned to 534.0 eV. The high concentration of electrolyte compounds found in Cell 3 indicate that the reaction to form LiF when cycling using the original pulsed profile is not one which dissolves electrolyte compounds and re-precipitates as LiF. Therefore, of the original chemical reactions proposed, there are only two more possibilities. The first is the direct reduction of electrolyte salts which can strip fluorides from the $LiPF_6$ molecule and react with lithium ions at the anode interface. The second is the dissolution of the cathode binder PVDF which can travel across the separator and react at the anode surface. Due to the corresponding signals from the areas assigned to degraded electrolyte salts in this study and the previous one conducted on cells PD 01-03 it is most likely that the source of the fluoride is the electrolyte salts. This means that pulsed discharging promotes the breakdown of electrolyte salts. None of this can be definitively proven without also doing an in-situ analysis that can model this breakdown, such as three electrode EIS. The data gathered in this research project has made a strong case that electrolyte salts are more unstable when the cell is cycled under a pulsed discharge profile.

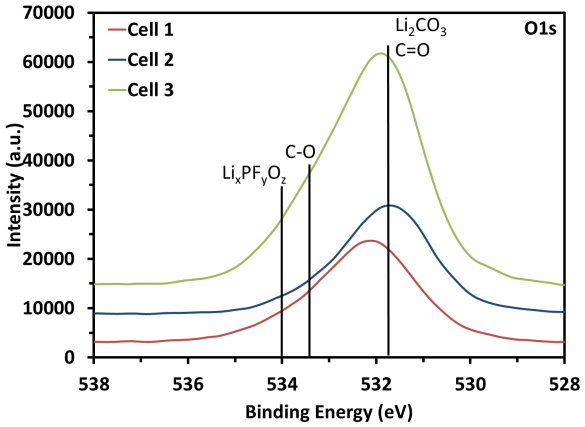

Figure 76: O 1s spectrums from anodes of Cells 1, 2, and 3 from the profile breakdown study

The spectrums collected from the P 2p region shown in Figure 77, further supports that the electrolyte salts are breaking down and resulting in the failure of the cell at high rates. Cell 3 which showed a larger signal from the area assigned to Li_2CO_3, also has a large signal near 134.0 eV which is assigned to $Li_xPF_yO_z$ phosphorus bonds. Oddly, in Cells 1 and 2, there is a very small presence of Li_xPF_y which appears around 137.0 eV. This may indicate that the breakdown of electrolyte salts occurs when the salts become unstable and react with the electrolyte solvents. The reaction may release fluorides that in turn reacts with lithium ions to form LiF. All in all, the P 2p region along with the data collected in the other regions has narrowed the possibilities of the reactions which can form the LiF which consistently deposits in high concentrations in cell which fail at high rates.

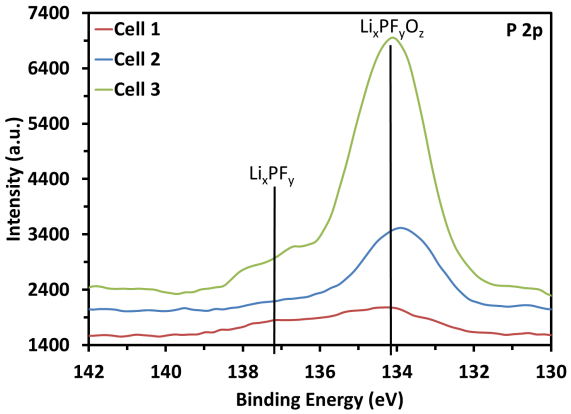

Figure 77: P 2p spectrums from anodes of Cells 1, 2, and 3 from the profile breakdown study

As before, a quantitative analysis is conducted by deconvolution of the peaks in the spectrums presented above. The results for Cell 1, 2, and 3 in each scanned region are shown in Table 13, Table 14, Table 15 below. As expected, the LiF concentration in Cell 1 was far higher than in Cells 2 and 3 with 17.39 at. % of fluorine atoms contributing to LiF bonds. This is over four times the amount in Cells 2 and 3 with 3.83 at. % and 4.60 at. % respectively. The concentration of oxygen atoms that contribute to Li_2CO_3 is lower than expected with the contribution from Cell 2 actually being higher with respect to the other atoms in their respective films. This can be explained by the higher concentrations of C-O bonds (approximately 8.6 at. %) and decomposed electrolyte salts, like Li_xPF_y and $Li_xPF_yO_z$ which are detected on the anode surface of Cell 3. Therefore, the fact that the Li_2CO_3 concentration is comparable to the other two cells still indicates that the atomic concentration of this compound is high relative to the concentration profiles of the other two cells. Again, it is interesting that Cell 3 had such higher concentrations of electrolyte compounds even though it failed in the same number of cycles and ran with the same profile as Cell 2 whose spectrums mirrored Cell 1.

Table 13: Results of the deconvolution of peaks for Cell 1 anodes

Region	Binding Energies (eV)	FWHM	Area %	Concentration (at. %)	Assigned Compound
C1s	283.06	1.48	6.28	2.20	LiC_x
	285	1.83	61.8	21.65	CH_x
	286.66	1.64	13.33	4.67	C-O
	289.28	2.97	18.59	6.51	Li_2CO_3, C=O
O1s	532.18	2.4	94.01	19.26	Li_2CO_3, C=O
	534.22	1.57	5.99	1.23	C-O
F1s	685.39	1.92	75.59	17.39	$LiF/Li_xPF_yO_z$
	687.58	2.26	24.41	5.61	Li_xPF_y
P2p	134.47	3.01	81.03	0.98	$Li_xPF_yO_z$
	137.24	2.03	18.97	0.23	$LiPF_6$
Li1s	55.27	2.04	100	20.27	Li_2CO_3 Li_xPF_y

Table 14: Results of the deconvolution of peaks in Cell 2 anodes

Region	Binding Energies (eV)	FWHM	Area %	Concentration (at. %)	Assigned Compound
C1s	285	1.66	78.78	38.92	CH_x
	286.49	1.85	14.86	7.34	C-O
	289.23	1.76	6.36	3.14	Li_2CO_3, C=O
O1s	531.99	2.15	93.3	23.33	Li_2CO_3, C=O
	533.78	1.53	6.7	1.68	C-O
F1s	685.18	1.91	50.67	3.83	$LiF/Li_xPF_yO_z$
	687.31	2.22	49.33	3.72	Li_xPF_y
P2p	134.17	2.1	86.97	2.30	$Li_xPF_yO_z$
	136.54	2.64	13.03	0.35	$LiPF_6$
Li1s	55.54	2.04	100	15.39	Li_2CO_3 Li_xPF_y

Table 15: Results of deconvolution for spectrums from Cell 3 anodes

Region	Binding Energies (eV)	FWHM	Area %	Concentration (at. %)	Assigned Compound
C1s	285	1.66	73.41	30.52	CH_x
	286.66	1.99	20.68	8.60	C-O
	289.48	2.54	5.91	2.46	Li_2CO_3, C=O
O1s	531.79	1.95	72.85	22.72	Li_2CO_3, C=O
	533.22	2.15	27.15	8.47	C-O
F1s	685.12	1.93	43.49	4.60	$LiF/Li_xPF_yO_z$
	687.4	2.32	56.51	5.97	Li_xPF_y
P2p	134.19	2.15	90.18	3.77	$Li_xPF_yO_z$
	136.89	1.92	9.82	0.41	$LiPF_6$
Li1s	55.65	2.12	100	12.48	Li_2CO_3 Li_xPF_y

The depth profiles for Cell 1 through Cell 3 show possible signs of metal oxide deposition in the anodes of Cells 2 and 3 but not Cell 1. In the C 1s regions of all three cells shown in Figure 78, Figure 79, and Figure 80, it can be clearly seen that the identified hydrocarbon peak in Cells 2 and 3 is more persistent as a function of depth compared to cells PD 01-03. Even after seven minutes of etching, the peak can still be seen making the C-C graphite peak broaden. In Cell 1, the hydrocarbon peak dissipates within the first few minutes of etching. This may indicate the depth of which the degrade electrolyte diffuses into the graphite matrix is greater in these cells. As mentioned in Equations 9-12, EC and DMC electrolytes can creak down to form metastable compounds which contain C-H bonds. It is unknown why this did not appear in the depth profiles taken on the initial pulsed cells.

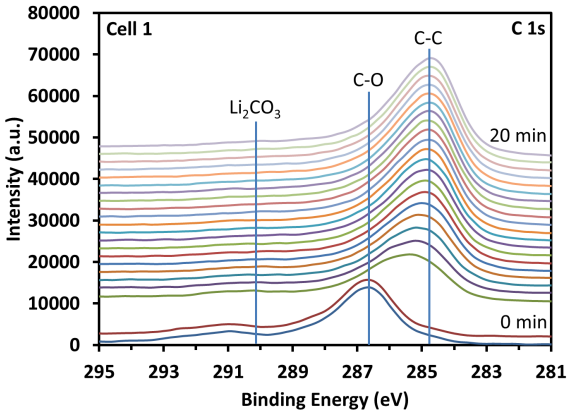

Figure 78: C 1s depth profile spectrums for Cell 1 anodes through 20 minutes of etching

In the O 1s region shown in Figure 81, Figure 82, and Figure 83, there is a new peak which arises after the three to four minutes of etching at a lower binding energy than the Li_2CO_3/C=O peak in Cell 3. It should be noted that these spectrums have not been corrected for the shift error in the spectrometer. In the multiplex spectra, all the peaks are shifted in accordance with the hydrocarbon peak. Based on the C 1s region the shift in these cells would be approximately 3.0 eV less than the current position. This shifts this new peak into a region where metal oxides usually appear according to XPS peak position databases [72].

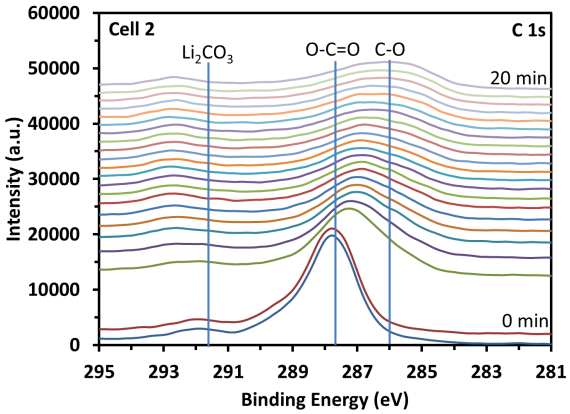

Figure 79: C 1s depth profile spectrums for Cell 2 anodes through 20 minutes of etching

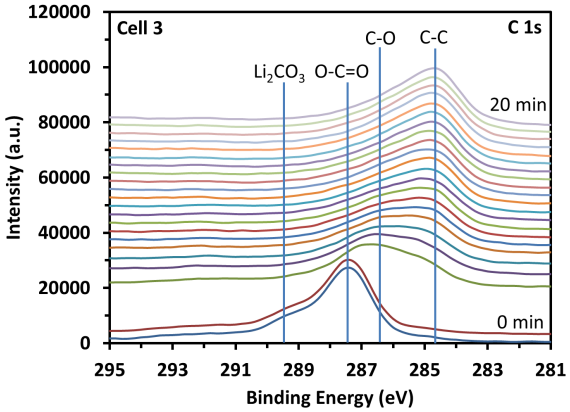

Figure 80: C 1s depth profile spectrums for Cell 3 anodes through 20 minutes of etching

This could be sign of metal dissolution where the cathode particles break down and metal ions are intercalated into the graphite anode. This peak doesn't appear in Cell 1 which had the one second rest step meaning that the charge step is critical for the metal dissolution to occur. A possible explanation for the dissolution in the case of these cells is the cyclic fatigue the cathodic matrix experiences causes the iron oxide octahedrons

to conglomerate and form larger phases which may be susceptible to breakdown under the bipolar pulsed discharge cycling conditions.

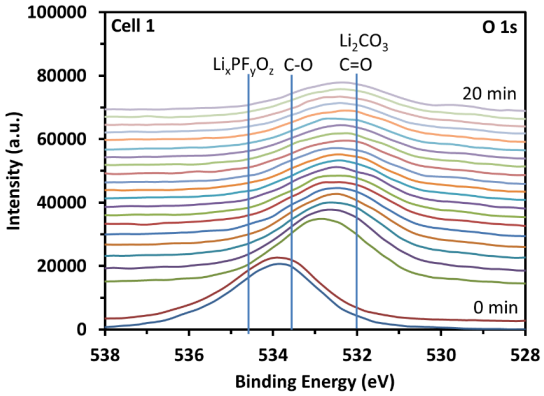

Figure 81: O 1s depth profile spectrums from Cell 1 anodes for 20 minutes of etching time

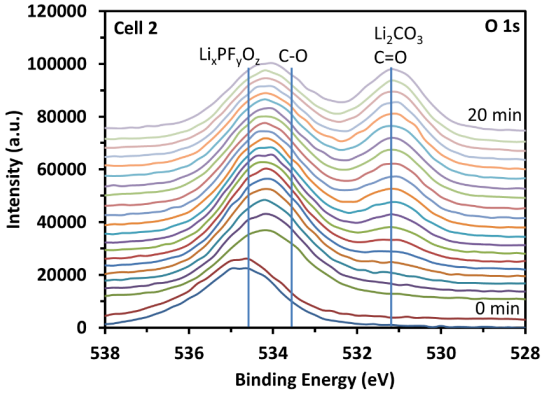

Figure 82: O 1s depth profile spectrums from Cell 2 anodes for 20 minutes of etching time

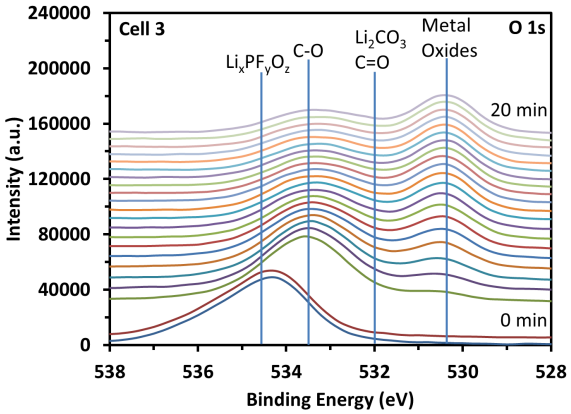

Figure 83: O 1s depth profile spectrums from Cell 3 anodes for 20 minutes of etching time

The spectrums from the F 1s region in Figure 84, Figure 85, and Figure 86 show that there is no penetration of the surface SEI fluoride compounds, like LiF, to the deeper layers of the graphite anode. After the first minute of etching (20 Å), only the peak for $Li_xPF_yO_z$ appears. This shows once again that the LiF film only exists in the top 20-40 Å of the anode but is enough to fail the cell at the 40 A rate. This may outline the need to place specific additives in the cell to influence the composition of the surface film and to suppress the LiF precipitation.

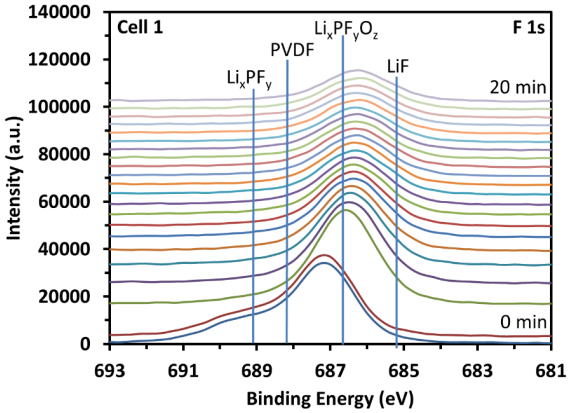

Figure 84: F 1s depth profile spectrums of an anode taken from Cell 1 with 20 minutes of etching

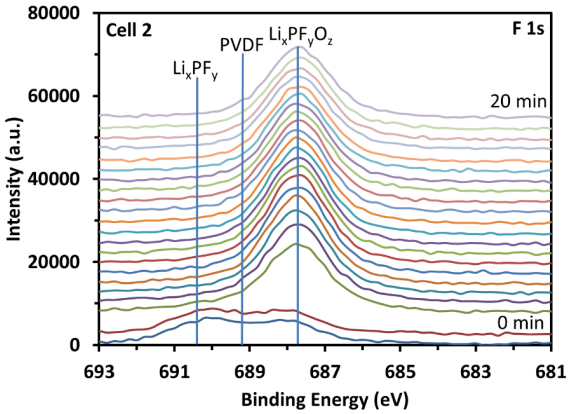

Figure 85: F 1s depth profile spectrums of an anode taken from Cell 2 with 20 minutes of etching

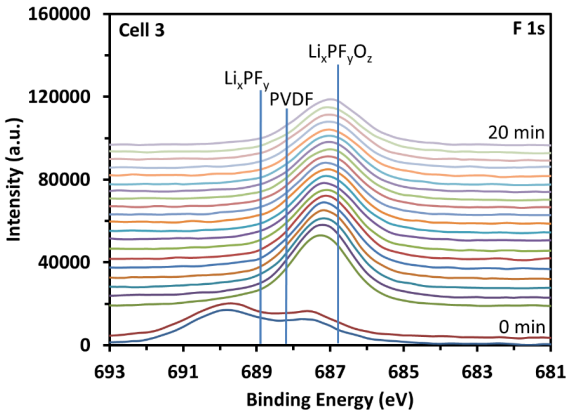

Figure 86: F 1s depth profile spectrums of an anode taken from Cell 3 with 20 minutes of etching

Finally, the P 2p region seen in Figure 87, Figure 88, and Figure 89 show that there is no signal from this region in Cell 1 and 3 after the first ten minutes of Argon etching. That corresponds to a 200 Å penetration into the graphite anode matrix. In Cells 2 however the phosphorus signal is still apparent after 20 minutes of etching which indicates a deeper diffusion of degraded salt compounds during the cycling life. Again, it is not thought that this difference influences the speed at which the cells reach the critical state of failure. However, it is interesting that Cell 1 and Cell 3 showed similar depth profiles in this region when it was expected that Cell 2 and 3 would be more compatible considering they were cycled using the exact same profile. In any case, there are key differences discussed in this section which outline the critical differences between Cell 1 and Cells 2 and 3. While all three cells were unable to accept charge at the 40 A rate after testing with their respective profiles, Cell 1 shows a greater isolation of degradation products to the surface of the graphite electrode material compared to

Cells 2 and 3. The one second charge step must promote the deeper intercalation of salt compounds. Furthermore, it may be the difference in determining the stability of the cathode crystal structure as the O 1s region indicated possible signs of metal ion deposition in the graphite anodes of these two cells and not in Cell 1. While this may not be the ultimate reason for the cell's inability to charge at 40 A, it may create sites for further side reactions with electrolyte products and increase stress on the graphite causing capacity fade. This is very valuable when using these results to determine the viability of base loading a generator using LFP 26650 cells or other cylindrical form factors as an interim power sink. These results determine that it may be more viable to place the cells in an actively controlled environment to limit the batteries role or to use them only as a source when the load is operating. This will reduce the number of possible pulses in a single discharge but may increase cycle life.

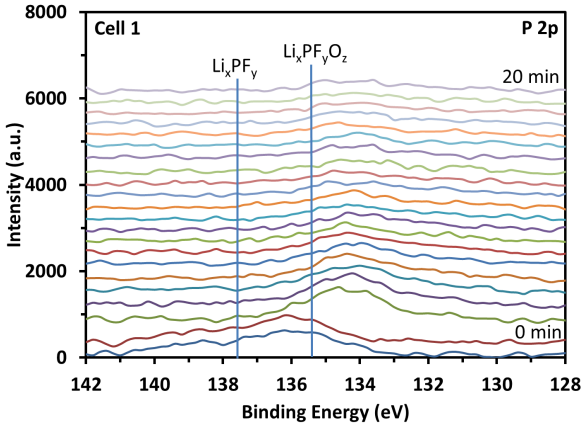

Figure 87: P 2p depth profile spectrums of anodes taken from Cell 1 with 20 minutes of etching time

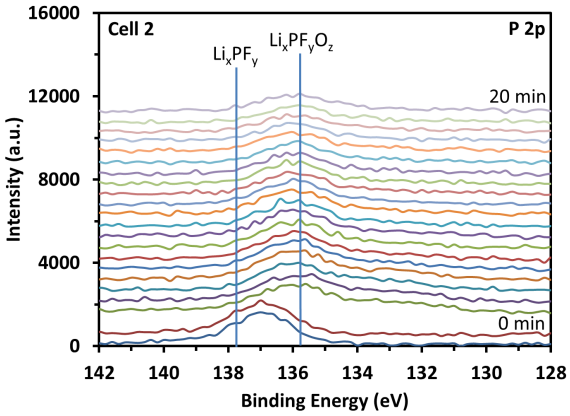

Figure 88: P 2p depth profile spectrums of anodes taken from Cell 2 with 20 minutes of etching time

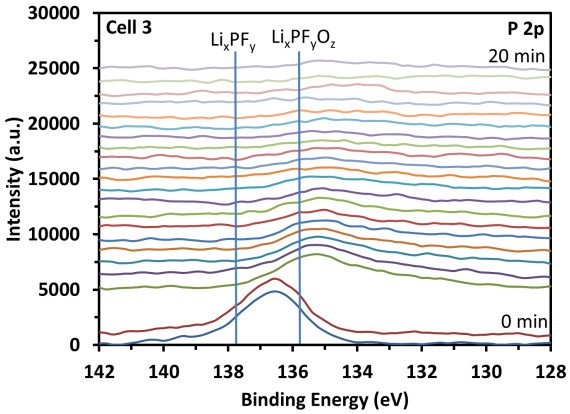

Figure 89: P 2p depth profile spectrums of anodes taken from Cell 3 with 20 minutes of etching time

Chapter 5: Conclusions and Future Work

The future role of lithium-ion batteries in high power applications requires them to operate under conditions that they are not necessarily designed for. In this body of work, two chemistries, nickel cobalt aluminum (NCA) and lithium iron phosphate (LFP), were studied to characterize their degradation behavior under high rate pulsed discharge operation to mimic the manner in which they could be used to both augment a motor-generator set during heavy load times or baseload the motor-generator during periods of load inactivity. Early testing of high frequency switching in NCA cells found that there was a faster rate of capacity fade compared to cells cycled under a continuously discharged high rate profile. LFP cells, cycled using a 40 A pulsed discharge profile, were found to show rapid capacity fade within 60 cycles of operation, especially concerning their ability to accept high rate recharge currents. Electrochemical impedance spectroscopy and differential capacitance analysis revealed an abrupt shift in the internal resistance of the cells that no longer were able to accept high rate recharge, and an extinguishing of the majority of charge phases. A characterization of the electrode material's atomic structure in post-mortem analysis revealed that these cells experienced very little shift in atomic order, permanent phase change, or cathode active material loss. An examination of the surface chemistry of the LFP cathode and graphitic anode electrodes showed signs of binder dissolution in the cathode and thin film formations on the anode that were rich in fluoride compounds, particularly LiF. Depth profiling revealed that these films were actually confined to the top 20-40 Å of the anode. The conclusion made was that the highly ionic resistant LiF film caused a slowing of the charge kinetics and along with the contact resistance increase in the

cathode caused the cell to no longer accept charge at the 40 A rate. Breaking down the profile to discover which step was most detrimental to the performance of these LFP cells revealed that the formation of the LiF films weren't dependent on the short one second charge pulse in the pulsed discharge profile. The recharge did however affect the amount of metal oxide signals found in the depth profiles of the anode in post-mortem analysis. It is concluded that the short recharge pulse promotes instability in the cathode causing metal dissolution and binder decomposition. Additionally, it was concluded that the switching nature of the pulsed profile, whether it contained the short recharge pulse or not, promotes the breakdown of $LiPF_6$ salts. Therefore, in order to use cylindrical LFP cells as a prime power supply for a high power pulsed load, a power systems architecture should be implemented to limit the role of the battery module. In addition, manufacturers will need to implement new additives and electrolyte formulations in order to influence the chemical composition of the surface films that develop. These advancements and control structures are key to making lithium-ion batteries a power source for future high power pulsed systems such as electric vehicles, grid storage, and shipboard power systems

Comment [DW10]: I reworded. Is that ok?

Work for future students

Towards the end of this research, an effort was made to develop an in-situ characterization technique that could be used on COTS cells to monitor the state of health without dismantling the cell or changing the form factor. The initial idea was to utilize a three-electrode reference system in order to separately collect information from the cathode and anode half cells. Through this, half-cell EIS and differential capacity profiles could be collected in interim. The initial design involved fabricating a custom,

novel three-electrode chamber shown in Figure 90. After initial testing, it was concluded that the components added too much resistance to the system making the resulting spectrums useless for any analysis. It was decided that the apparatus needed to fit inside the cell so that the entire assembly could be seal within the battery's casing in order to ensure a uniform and sealed environment for both the cell and the three electrode device.

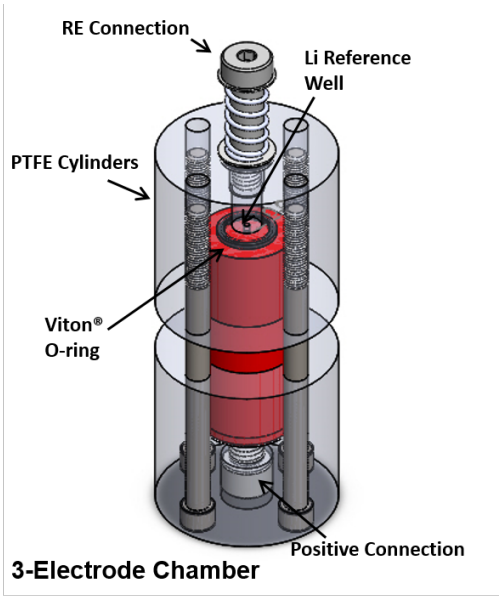

Figure 90: Diagram of the initial design for a three electrode chamber

The procedure involved securing un-dosed and un-crimped cells from the manufacturer in order to insert a glass capillary tube down the core of the cell with a piece of reference lithium metal attached to a copper wire inside. The process to assemble this apparatus is outlined in Appendix A. Initial testing showed promising results with the two half-cell EIS spectrums matching well in initial scans. An example of a successful in-situ

three electrode cell is pictured in Figure 91. An initial scan of both half cells can be seen in Figure 92. Adding both half-cell spectrums together yields a profile which matches the two electrode spectrum within 3% at all frequencies scanned (Figure 93).

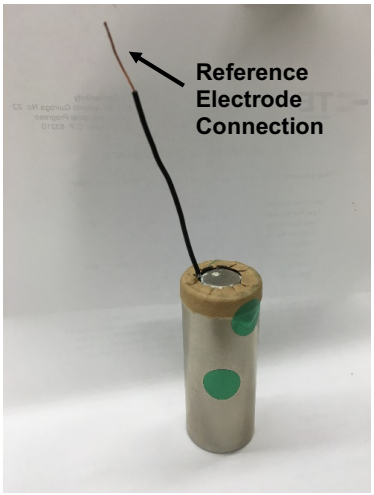

Figure 91: Picture of an assembled three-electrode 26650 cell with a copper wire connection for the reference

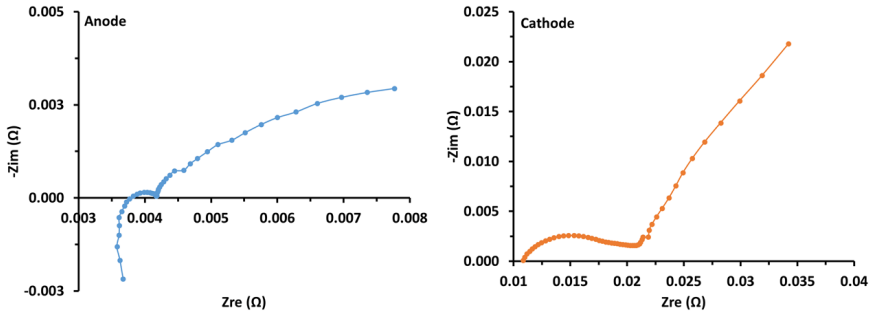

Figure 92: EIS spectrums from the half-cells of the custom three electrode cell

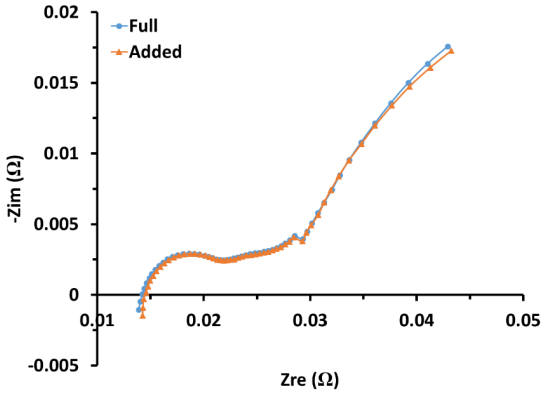

Figure 93: Diagram of the full two-electrode spectrum compared to the added spectrum from the two half-cell scans

Initial testing shows that this design is capable of providing in-situ differential data and in-situ EIS analysis without the dismantling of the cell. It also shows that this design is capable of withstanding the harsh cycling conditions that exists in the pulsed discharge profile proposed. This design would be ideal for collecting both EIS spectrums and differential capacitance data between intervals of high rate pulsed discharge. It is also ideal for modeling impedance elements since the two half-cells can be separated making their independent study possible. A full in-situ diagnostic on the high power 26650 LFPs would be highly beneficial towards the full understanding of the degradation evolution in the failed pulsed discharged cells.

The device currently has issues which must be overcome before it can be deemed fully dependable. Currently, about 50% of the cells built show a separation of the low frequency semi-circle from the one located at the mid-frequency range. This can also be seen in Figure 93. This may be an issue with the electrode films not soaking in enough electrolyte during the filling process in order to function properly. Inserting the three electrode assembly into the core of the cell may not allow the films to expand as easily.

Efforts were made to determine whether there is a defect with the electrolyte. A cell which was received from the manufacturer sealed but not filled was drilled from the top cap. Then electrolyte from the same bottle was introduced using the same method as the three electrode cells. The cell was sealed with epoxy and charged to 50% SOC where a galvanostatic EIS was conducted using a 1.0 A sinusoidal amplitude. The spectrum, shown in Figure 94, appears to mimic the behavior seen in production cells indicating that it is not an issue with the electrolyte. It would be beneficial to insert a smaller diameter glass tube down the center of the cell in order to make room for the jelly roll to expand. This would also mean that less lithium metal can be used for the reference which may cause issues with the contact resistance between it and the copper wire connection.

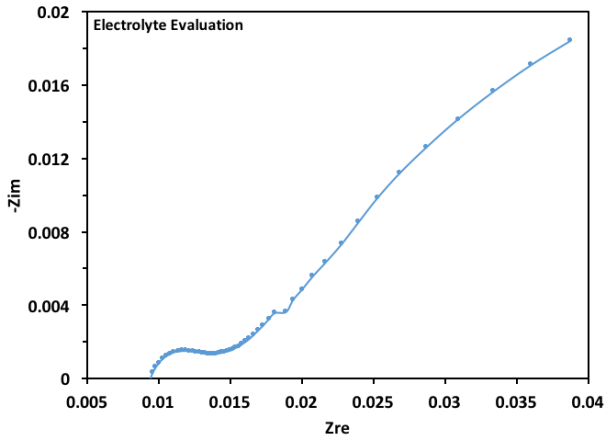

Figure 94: An EIS spectrum of a 26650 LFP cell which shows that the electrolyte used in the three electrode cells hasn't degraded.

Future efforts in this work should focus on in-situ methods such as this which can withstand the pulsed discharging conditions which the Navy wishes to test. The issues with the design pointed out above indicate that small design changes need to be

implemented in order for the three electrode cells to be properly compared to the LFP 26650 production cells.

Appendix A

Procedures for cell assembly/disassembly for custom cells and electrode extraction

Disassembly procedure for 26650 cell electrode extraction

1. Discharge the cell to 0% state of charge to prevent any accidental shorting and damage to the cell.
2. Begin by cutting slits in the top cap seal as pictured in Figure 95. Keep them as equally spaced as possible. DO NOT cut past the rubber seal as you will short the cell.

Figure 95: Picture of slits cut into the top cap

3. Peel back the slits that were cut by using a pair of needle nose pliers. Again, be careful not to touch the top cap to the case. Use the crimped lip as leverage and peal back.
4. When the slits are peeled back the top cap should come off like in Figure 96. Sever the tab welded to the top cap and carefully fold the tabs back down toward the jelly roll to keep them out of the way.

Figure 96: Picture of the top cap removed from the base

5. Now cut perforations into the side casing at equal intervals as shown in Figure 97. Use the lines cut in the top cap as guidelines and cut straight to the base. Be very careful to only make perforations and DO NOT cut through the casing.

Figure 97: Picture of the perforations cut into the side casing

6. Using the needle nose pliers, peel back the casing on all sides using the perforations (Figure 98). Once all sides have been peeled back, the jelly roll should be easy to remove. Sever the connection to the case at the bottom.

Figure 98: Picture of the side casing peeled back and the jelly roll exposed

7. Taking a sharp blade (utility knife) carefully cut the tape holding the jelly roll together. Afterwards you should be able to unravel the jelly roll for electrode extraction (Figure 99).

Figure 99: Picture of the jelly roll after the tape is cut and the roll unravels

Assembly procedure for the novel, in-situ three electrode cell

1. Taking a non-filled, un-crimped cell, drill a 7/32” hole from the bottom side of the top cap through the pressure cap. Be careful not to sever the connection to the top cap. It is best to drill the hole off center in order to avoid this. Do not drill through the top nip (Figure 100).

Figure 100: Picture of the hole drilled in the bottom side of the top cap

2. Transfer the cell into a glove box along with marine epoxy and tools to handle the reference electrode assembly.
3. Take a 2.0 mm metal rod and slowly place it down the center of the cell to make room for the reference electrode (Figure 101). It is ok to move the rod around to open up the core of the jelly roll but be careful not to damage the electrode films. Leave the rod in until it is time to insert the reference electrode.

Figure 101: Metal rod inserted down the center of the cell

4. To build the reference assembly, take a 2.0 mm ID, borosilicate glass capillary tube and place a thin piece of lithium metal inside making sure its compressed. Afterwards, feed a 22 AWG copper wire through one side of the tube and carefully slide it against the lithium metal. Make sure the wire and lithium are fitted tightly together with good contact. It should look like Figure 102 when it is done. This is a model for reference purposes and the white substitute in the picture should be replaced with lithium metal in the real device

Figure 102: Representation of the reference electrode assembly.

5. Fill the other side of the tube with electrolyte. Use a syringe to make sure there are no air bubbles between the lithium metal and the end of the tube.
6. Remove the metal rod from the core of the cell and place the reference assembly, glass tube first, into the core of the cell. Subsequently, feed the wire through the hole in the top cap and out top using the small holes which are between the top nip and the base of the cap (Figure 103).

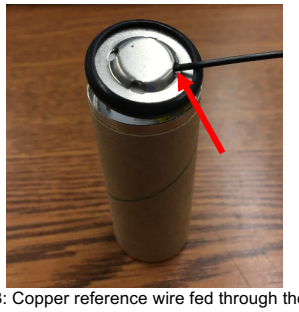

Figure 103: Copper reference wire fed through the top cap

7. Using the marine epoxy, seal the hole in the top cap around the wire and allow it to set before continuing. It is best to mount the cell upside down while waiting for the epoxy to dry so that the epoxy will not drip into the jelly roll.
8. After the epoxy has settled, use the syringe to drip 10 mL of electrolyte into the cell. It will be necessary at times to stop and wait for the electrolyte to be absorbed by the electrode material as not all of the 10 mL will be able to be accepted immediately. It is best to fill the cell as much as possible, wait 15 minutes, and then return to continue filling. Repeat this process until the 10 mL is achieved.
9. Press the top cap down ensuring the tabs welded to the top cap do no touch the edges of the case. Press down firmly on the top cap and hold to ensure the tab folds correctly.
10. Place the cell inside the metal brace that fits around the pinched edges of the cell as shown in Figure 104. Use a small vice grip to hold it in place. Place the battery inside the press via the hole cut in the base. Insert the crimping die on top of the cell by feeding the reference wire through the hole in the center.

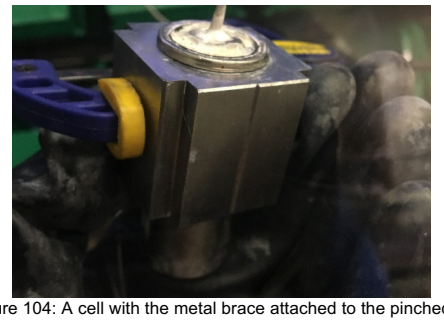

Figure 104: A cell with the metal brace attached to the pinched lip

11. Place the hydraulic cylinder over the top of the die and under the top steep plate. Make sure afterwards that there is minimal space between the hydraulic cylinder and the top plate of the press. Use the hydraulic cylinder to press the die onto the cell. DO NOT over press the dye. You need only press until the die is fully pressed on. Then remove the hydraulic cylinder and the die from the top of the cell.
12. Repeat steps 10 and 11 for the next two stages of dies. Afterwards, let the cell sit in the glovebox for at least 24 hours before using the startup procedure provided by the manufacturer to charge the cell for the first time.

References

[1] B. Lendon, "Navy's future: Electric gun, lasers, water as fuel," CNN, 10 April 2014. [Online]. [Accessed 20 August 2016].

[2] D. Stoudt, "Naval Directed-Energy Weapons-No Longer a Future Weapon Concept," *Leading Edge,* vol. 7, no. 4, pp. 6-11, 2012.

[3] H. Fair, "Progress in Electromagnetic Science and Technology," *IEEE Tranactions on Magnetics,* vol. 43, no. 1, pp. 93-98, 2007.

[4] H. Fair, "Advances in Elelctromagnetic Launch Science and Technology," *IEEE Transactions on Magnetics,* vol. 45, no. 1, pp. 225-230, 2009.

[5] S. Littlefield, "Roadmap for the all-electric warship," Electric Power, 15 February 2005. [Online]. Available: http://www.powermag.com/roadmap-for-the-all-electric-warship/?printmode=1. [Accessed 23 August 2016].

[6] I. J. Cohen, J. P. Kelley, D. A. Wetz and J. Heinzel, "Evaluation of a Hybrid Energy Storage Module for Pulsed Power Applications," *Plasma Science, IEEE Transactions on,* vol. 42, no. 10, pp. 2948-2955, 2014.

[7] I. Cohen, C. Westenhover and D. Wetz, "Evaluation of an actively contolled battery-capacitor hybrid energy storage module (HESM) for use in driving pulsed power applications," in *Pulsed Power Conference*, Austin, TX, 2015.

[8] G. Majeau-Bettez, "Life Cycle Environmental Assessment of Lithium-Ion and Nickel Metal Hrdide Batteries for Plug-In Hybrid and Battery Electric Vehicles," *Environmental Science and Technology,* vol. 45, no. 10, pp. 4548-4554, 2011.

[9] P. Gifford, "Development of advanced nickel/metal hydride batteries for electric and hybrid vehicles," *Journal of Power Sources,* vol. 80, no. 1-2, pp. 157-163, 1999.

[10] N. Sato, "Thermal behavior analysis of nickel metal hydride battereis for electric vehicles," *JSAE Review,* vol. 21, no. 2, pp. 205-211, 2000.

[11] G.-A. Nazri, Lithium Batteries Science and Technology, New York: Springer, 2009.

[12] Q. Wang, "Thermal runaway caused fire and explosion of lithium ion battery," *Journal of Power Sources,* vol. 208, no. 1, pp. 210-224, 2012.

[13] G.-H. Kim, "A three dimensional thermal abuse model for lithium-ion cells," *Journal of Powers Sources,* vol. 170, no. 2, pp. 476-489, 2007.

[14] Battery University, "Types of Lithium-Ion," Battery University, 2003. [Online]. Available: http://batteryuniversity.com/learn/article/types_of_lithium_ion. [Accessed 19 August 2016].

[15] K. Fehrenbacher, "Why Tesla's grid batteries will use two different chemistries," Fortune, 18 May 2015. [Online]. [Accessed 12 August 2016].

[16] C. Chen, "Aluminum-doped lithium nickel cobalt oxide electrodes for high-power lithium-ion batteries," *Journal of Power Sources,* vol. 128, no. 2, pp. 278-285, 2004.

[17] N. Omar, "Assessment of performance of lithium iron phosphate oxide, nickel manganese cobalt oxide and nickel cobalt aluminum oxide based cells for using in plug-in battery electric vehicle applications," in *2011 IEEE Vehicle Power and Propulsion Conference*, Chicago, 2011.

[18] M. Wohlfahrt-Mehrens, "Aging mechanisms of lithium cathode materials," *Journal of Power Sources,* vol. 127, no. 1-2, pp. 58-64, 2004.

[19] S. Franger, "Optimized Lithium Iron Phosphate for High-Rate Electrochemical Applications," *Journal of the Electrochemical Society,* vol. 151, no. 7, pp. A1024-A1027, 2004.

[20] V. Srinivasan, "Discharge Model for the Lithium Iron-Phosphate Electrode," *Journal of the Electrochemical Society,* vol. 151, no. 10, pp. A1517-A1529, 2004.

[21] G. Liang, "Lithium iron phosphate with high-rate capability synthesized through hydrothermal reaction in glucose solution," *Journal of Power Sources,* vol. 184, no. 2, pp. 538-542, 2008.

[22] N. Omar, "Lithium iron phosphate based battery-Assessment of the aging parameters and development of cycle life model," *Applied Energy,* vol. 112, no. 1, pp. 1575-1585, 2014.

[23] J. Molenda and M. Molenda, Metal, Ceramic, and Polymeric Composites for Various Uses, Intech, 2011.

[24] A. Kuwahara, "High-rate properties of LiFePO4/carbon composites as cathode materials for lithium-ion batteries," *Ceramics International,* vol. 34, no. 4, pp. 863-866, 2008.

[25] Y. Zhang, C.-Y. Wang and X. Tang, "Cycling Degradation of an automotive LiFePO4 lithium-ion battery," *Journal of Power Sources,* vol. 196, no. 1, pp. 1513-1520, 2010.

[26] M. A. Monem, "Lithium-ion batteries: Evaluation study of different charging methodologies based on aging process," *Applied Energy,* vol. 152, no. 1, pp. 143-155, 2015.

[27] K. Edstrom, M. Herstedt and D. P. Abraham, "A new look at the solid electrolyte interphase on graphite anodes in Li-ion batteries," *Journal of Power Sources,* vol. 153, no. 1, pp. 380-384, 2006.

[28] J. Vetter, P. Novak and M. Wagner, "Aging mechanisms in lithium-ion batteries," *Journal of Power Sources,* vol. 147, no. 1-2, pp. 269-281, 2005.

[29] L. Bodenes, "Lithium secondary battereis working at very high temperature: Capacity fade and understanding of aging mechanisms," *Journal of Power Sources,* vol. 236, no. 1, pp. 265-275, 2013.

[30] Y. Li, "Understanding Long-Term Cycling Performance of Li1.2Ni0.15Mn0.55Co0.1O2-Graphite Lithium-Ion Cells," *Journal of the Electrochemical Society,* vol. 160, no. 5, pp. A3006-A3019, 2013.

[31] P. Verma, P. Maire and P. Novak, "A review of the features and analyses of the solid electrolyte interphase in Li-ion batteries," *Electrochimica Acta,* vol. 55, no. 1, pp. 6332-6341, 2010.

[32] H. Bryngelsson, M. Sterndahl, T. Gustafsson and K. Edstrom, "How dynamic is the SEI," *Journal of Power Sources,* vol. 174, pp. 970-975, 2007.

[33] M. Ouyang, "Low temperature aging mechanism identification and lithium deposition in a large format lithium iron phosphate battery for different charge profiles," *Journal of Power Sources,* vol. 286, no. 1, pp. 309-320, 2015.

[34] E. Peled, "The electrochemical Behavior of Alkali and Alkaline Earth Metals in Nonaquesous Battery Systems-The Solid Electrolyte Interphase Model," *Journal of the Electrochemical Society,* vol. 126, no. 12, pp. 2047-2051, 1979.

[35] A. Andersson, "Chemical Composition and Morphology of the Elevated Temperature SEI on Graphite," *Journal of the Electrochemical Society,* vol. 148, no. 10, pp. A1100-A1109, 2001.

[36] P. Arora, "Capacity Fade Mechanisms and Side Reaction on Lithium-Ion Batteries," *Journal of the Electrochemical Society,* vol. 145, no. 10, pp. 3647-3667, 1998.

[37] N. P. Pieczonka, "Understanding Transition-Metal Dissolution Behavior in LiN0.5Mn1.5O4 High-Voltage Spinel for Lithium Ion Batteries," *Journal of Physical Chemistry C,* vol. 117, no. 31, pp. 15947-15957, 2013.

[38] J. Zheng, "The effects of TiO2 coating on the electrochemical performance of Li[Li0.2Mn0.54Ni0.13Co0.13]O2 cathode material for lithium-ion battery," *Solid State Ionics,* vol. 179, no. 27-32, pp. 1794-1799, 2008.

[39] R. Miao, "PVDF-HFP-based porous polymer electrolyte membranes for lithium-ion batteries," *Journal of Power Sources,* vol. 184, no. 2, pp. 420-426, 2008.

[40] J. R. Kim, "Electrospun PVdF-based fibrous polymer electrolytes for lithium ion polymer batteries," *Electrochemical Acta,* vol. 50, no. 1, pp. 69-75, 2004.

[41] J. W. Braithwaite, "Corrosion of Lithium-Ion Battery Current Collectors," *Journal of the Electrochemical Society,* vol. 146, no. 2, pp. 448-456, 1999.

[42] S. Zhang, "Aluminum corrosion in electrolyte of Li-ion battery," *Journal of Power Sources,* vol. 109, no. 2, pp. 458-464, 2002.

[43] L. J. Krause, "Corrosion of aluminum at high voltages in non-aqueous electrolytes containing perfluoroalkylsulfonyl imides; new lithium salts for lithium-ion cells," *Journal of Power Sources,* vol. 68, no. 2, pp. 320-325, 1997.

[44] B. Shrestha and D. A. Wetz, "Pulsed Elevated Rate Discharge of Electrochemical Energy Storage Devices," *IEEE Transactions on Plasma Science,* vol. 40, no. 10, pp. 2462 - 2469, 2012.

[45] D. A. Wetz and B. Shrestha, "Elevated Rate Cycling of High-Power Electrochemical Energy Storage Devices for Use as the Prime Power Source of an EM Launcher," *IEEE Transactions on Plasma Science,* vol. 41, no. 5, pp. 1319 - 1325, 2013.

[46] G. Rodriguez, "A utility of the role of energy storage in the smart grid," in *IEEE Power and Nergy Society General Meeting*, 2010.

[47] H. Qian, "A high-efficiency grid-tie battery energy storage system," *IEEE Transactions on Power Electronics,* vol. 26, no. 3, pp. 886-896, 2010.

[48] W. Li, "Real-Time Simulation of a Wind Turbine Generator Coupled With a Battery Supercapacitor Energy Storage System," *IEEE Transactions on Industrial Electronics,* vol. 57, no. 4, pp. 1137-1145, 2009.

[49] Y. Yao, "Interconnected Silicon Hollow Nanospheres for Lithium-Ion Battery Anodes with Long Cycle Life," *Nano Letters,* vol. 11, no. 7, pp. 2949-2954, 2011.

[50] M. Ge, "Porous Doped Silicon Nanowires for Lithium Ion Battery Anode with Long Cycle Life," *Nano Letters,* vol. 12, no. 5, pp. 2318-2323, 2012.

[51] B. Shrestha, "Development of a test stand for recharging electrochemical energy storage devices at pulsed elevated rates," *IEEE Transactions on Plasma Science,* vol. 40, no. 1, pp. 2462-2469, 2012.

[52] D. N. Wong, B. Shrestha, D. A. Wetz and J. M. Heinzel, "Impact of high rate discharge on the aging of lithium nickel colbalt aluminum oxide batteries," *Journal of Power Sources,* vol. 280, no. 1, pp. 363-372, 2015.

[53] B. Shrestha, D. A. Wetz and P. Novak, "Development of a test stand for recharging electrochemical energy storage devices at pulsed elevated rates," *IEEE Transactions on Plasma Science,* vol. 40, pp. 2462-2469, 2012.

[54] G. Ning, B. Haran and B. Popov, "Capacity fade of lithium-ion batteries cycled at high discharge rates," *Journal of Powers Sources,* vol. 117, no. 2003, pp. 160-169, 2003.

[55] P. Agarwal, "Measurement Models for Electrochemical Impedance Spectroscopy," *Journal of the Electrochemical Society,* vol. 139, no. 7, pp. 1917-1927, 1992.

[56] J. Wang, Y.-c. K. Chen-Wiegart and J. Wang, "In operando tracking phase transformation evolution of lithium iron phosphate with hard X-ray microscopy," *Nature Communications,* vol. 55, no. 70, pp. 1-10, 2014.

[57] H. Dahn, A. Smith, J. Burns and J. Dahn, "User-Friendly Differential Voltage Analysis Freeware for the analysis of degrdation mechanisms in Li-ion batteries," *Journal of the Electrochemical Society,* vol. 159, no. 9, pp. A1405-A1409, 14 August 2012.

[58] D. Andre, M. Meiler, K. Steiner and C. Wimmer, "Characterization of high-power lithium-ion batteries by electrochemical impedance spectroscopy. I. Experimental

Investigation," *Journal of Power Sources,* vol. 196, no. 12, pp. 5334-5341, 15 June 2011.

[59] E. Peled, "An Advanced Tool for the Selection of Electrolyte Components for Rechargeable Lithium Batteries," *Journal of the Electrochemical Society,* vol. 145, no. 10, pp. 3482-3486, 1998.

[60] Y.-S. Hong, K. S. Ryu, Y. J. Park and M. G. Kim, "Amorphous FePO4 as 3V cathode material for lithium secondary batteries," *Journal of Materials Chemistry,* vol. 12, no. 2002, pp. 1870-1874, 2002.

[61] M. Morcrette, Y. Chabre and G. Vaughan, "In-situ X-ray diffraction techniques as a powerful tool to study battery electrode materials," *Electrochimica Acta,* vol. 47, no. 1, pp. 3137-3149, 2002.

[62] S. Yang, Y. Song and P. Y. Zavalij, "Reactivity, stability and electrochemical behavior of lithium iron phosphates," *Electrochemistry Communications,* vol. 4, no. 3, pp. 239-244, 2002.

[63] T. Ohzuku, "Formation of Lithium-Graphite Intercalation Compounds in Nonaqueous Electrolytes and Their Application as a Negative Electrode for a Lithium Ion (Shuttlecock) Cell," *Journal of the Electrochemical Society,* vol. 140, no. 9, pp. 2490-2498, 1993.

[64] M. Newville, "IFEFFIT: Interactive EXAFS analysis and FEFF fitting," *Journal of Synchrotron Radiation,* vol. 8, no. 1, pp. 322-324, 2001.

[65] B. Ravel and M. Newville, "Athena, Artemis, Hapheastus: data analysis for x-ray absorption spectroscopy using IFEFFIT," *Journal of Synchrotron Radiation,* vol. 12, no. 1, pp. 537-541, 2005.

[66] D. Abraham, "Diagnosis of power fade mechanisms in high-power lithium-ion cells," *Journal of Power Sources,* Vols. 119-121, no. 1, pp. 511-516, 2003.

[67] S. S. Zhang, "A review on electrolyte additives for lithium-ion batteries," *Journal of Power Sources,* vol. 162, no. 1, pp. 1379-1394, 2006.

[68] J. H. Horton, "Researhc Projects," 2009. [Online]. Available: http://faculty.chem.queensu.ca/people/faculty/horton/research.html. [Accessed 20 August 2016].

[69] C. K. Chan, "Surface chemistry and morphology of the solid electrolyte interphase on silicon nanowire lithium-ion battery anodes," *Journal of Power Sources,* vol. 189, no. 1, pp. 1132-1140, 2009.

[70] D. Aurbach, B. Markovsky, A. Shecter and Y. Ein-Eli, "A comparitive study of synthetic graphite and Li electrodes in electrolyte solutions based on ethylene cabonate-dimethyl carbonate mixtures," *Journal of the Electrchemical Society,* vol. 143, no. 12, pp. 3809-3821, 1996.

[71] E. Peled, "Composition, depth profiles and lateral distribution of materials in the SEI built on HOPG-TOF SIMS and XPS studies," *Journal of Power Sources,* Vols. 97-98, no. 1, pp. 52-57, 2001.

[72] Thermo Scientific, "XPS Reference," Thermo Scientific, 2013. [Online]. Available: http://xpssimplified.com/periodictable.php. [Accessed 22 August 16].

[73] K2 Energy, "High Capacity LFP26650P Power Cell Data," [Online]. Available: http://liionbms.com/pdf/k2/LFP26650P.pdf. [Accessed 22 September 2015].

[74] D. A. Wetz, B. Shrestha, S. T. Donahue, D. N. Wong, M. J. Martin and J. M. Heinzel, "Capacity Fade of 26650 Lithium-Ion Phosphate Batteries Considered for Use Within a Pulsed-Power System's Prime Power Supply," *Plasma Science, IEEE Transactions on,* vol. 43, pp. 1448-1455, 2015.

[75] I. J. Cohen, D. A. Wetz, C. Storm and J. Heinzel, "Impact of a Hybrid Energy Storage Module on Power Quality of a Fossil Fuel Generator," in *Proceedings of the 2014 American Society of Naval Engineers Electric Machines Technology Symposium (EMTS)*, Philadelphia, 2014.

[76] P. Novak, D. Wetz and B. Shrestha, "Cycling Fatigue induced on Electrochemical Energy Storage Cells as a result of High C Pulsed Charging," *Electrochemical Society Transactions,* vol. 50, no. 26, pp. 175-186, 2013.

[77] D. Wetz, B. Shrestha and P. Novak, "Pulsed Evaluation of High Power Electrochemical Energy Storage Devices," *IEEE Transactions on Dielectrics and Electrical Insulation,* vol. 20, no. 4, pp. 1040-1048, 2013.

[78] Saft America, Inc., "Rechargeable lithium-ion battery VL 5U - Ultra high power cell; Doc. No. 54073-2-1009," 2009.

[79] B. Shrestha, D. Wetz and P. Novak, "The Impact of High Pulsed Loading on the Fatigue of Electrochemical Energy Storage Devices," *Electrochemical Society Transactions,* vol. 50, no. 26, pp. 187-196, 2013.

[80] *MIL-STD-1399,* Department of Defense, 2008.

[81] I. Cohen, D. Wetz and J. Kelley, "Evaluation of a Hybrid Energy Storage Module for Pulsed Power Applications," *IEEE Transactions on Plasma Science,* vol. 42, no. 10, pp. 2948-2955, 2014.

Biographical Information

Derek Wong was born in Pasadena, California and received his Bachelors of Science degree in Mechanical Engineering from the University of Texas at Austin. Afterwards, he moved on to earn his PhD in Materials Science and Engineering at the University of Texas at Arlington. He has interned at both the Naval Surface Warfare Center-Carderock Division in Bethesda, Maryland and Halliburton Drill Bits and Services in Conroe, TX. During his time as a student, Derek has been involved in many aspects of his department including representing UT Arlington's student chapter of ASM International as their vice-president. In the summer of 2014, he led this organization's efforts to organize a highly successful, regional summer camp for neighboring K-12 students to learn more about the world of engineering and materials science. Later on, Derek was recognized by being awarded for his research in lithium-ion battery degradation at the 2014 ASM International North Texas Research Symposium.